# Physik-Department

Measurement of light emission

in organic liquid scintillators

and studies towards the search for proton decay

in the future large-scale detector LENA

Dissertation

von

Teresa Marrodán Undagoitia

Technische Universität München

Measurement of light emission in organic liquid scintillators and studies towards the search for proton decay in the future large-scale detector LENA

Teresa Marrodán Undagoitia

Abstract

The LENA (**L**ow **E**nergy **N**eutrino **A**stronomy) detector is a proposed large liquid-scintillator neutrino observatory. Its main physics goals are the detection of low-energy neutrinos from the Sun, from Supernovae of type II, and from the Earth, and the search for proton decay. For this thesis, technical feasibility studies concerning the optical properties of the liquid-scintillator medium have been performed. The fluorescence decay-time constants and the light-emission spectra of different scintillator mixtures have been investigated. For this purpose, new experimental setups have been designed and constructed. The variation of the decay constants with the solute type and with the concentration has been analyzed for scintillator mixtures of the solvents PXE, LAB, and dodecan with the wavelength-shifters PPO, pTP, PMP, and bisMSB. In addition, the scintillation spectra have been recorded after excitation of the scintillator by UV radiation as well as by $10 \, \mathrm{keV}$ electrons. All results are interpreted in terms of a microscopic model of the scintillation mechanism. Regarding the results of the measurements performed in this thesis, for a large detector like LENA a mixture of PXE, $2 \, \mathrm{g}/\ell$ PPO and $20 \, \mathrm{mg}/\ell$ bisMSB shows the best performance because the main time constant is short. The potential of LENA to search for several proton-decay reactions has been evaluated. Using the Geant4 toolkit, a simulation has been performed for the SUSY-favored decay channel $p \rightarrow K^+\overline{\nu}$. Its atmospheric neutrino background has been explored in detail. For the proton lifetime τ_p a sensitivity of $\tau_p = 4 \cdot 10^{34} \, \mathrm{y}$ can be achieved via $p \rightarrow K^+\overline{\nu}$ within $10 \, \mathrm{y}$ of measuring time. The impact of the optical properties of the scintillator on the proton-decay detection efficiency has also been studied. Variations in the fluorescence decay constants or in the scattering lengths of the scintillator can lead to an increase or decrease of about 10% in the detection efficiency.

III

Kurzfassung

LENA (aus dem englischen **L**ow **E**nergy **N**eutrino **A**stronomy) ist
ein neu geplantes, auf der Technik eines Flüssigszintillators basiertes
Großprojekt für die Neutrinophysik und die Suche nach Proton-
zerfällen. In dieser Doktorarbeit werden dazu Machbarkeitsstudien
vorgestellt, die sowohl experimentelle Aspekte als auch Monte-Carlo
Simulationen beinhalten. Fluoreszenzzeiten und Emissionsspektren
von verschiedenen Szintillatormischungen werden präsentiert und im
Rahmen eines mikroskopischen Modells interpretiert. Simulationen
des LENA Experimentes zeigen, daß nach 10 Jahren Laufzeit eine
Sensitivität von $4 \cdot 10^{34}$ Jahren für die Lebensdauer des Protons im
Kanal $p \rightarrow K^+ \overline{\nu}$ erreicht werden kann. Der Einfluß der gemessenen
optischen Eigenschaften der Szintillatormischung auf die Sensitivität
von LENA zur Suche nach dem Protonzerfall wird aufgezeigt.

Contents

Contents

VII

Contents

VIII

Chapter 1

Introduction

During the last years, astroparticle physics has made a lot of progress leading to very important results. On the one hand, neutrinos provide a new method to study astrophysical processes like the energy production in our Sun or the mechanism of a core-collapse supernova explosion. On the other hand, the discovery of neutrino oscillations and, connected to that, neutrino masses give a strong motivation to extend the standard model of particle physics and to search for new physics beyond it.

One of the pioneering projects in the field was the Homestake experiment [1], performed in the early 1970s by R. Davis, which measured neutrinos from the Sun. It used the capture of neutrinos on ^{37}Cl which produces an electron and ^{37}Ar. The experiment was first tried out without success with $\overline{\nu}_e$ from a closeby power reactor proving that ν_e and $\overline{\nu}_e$ have different interactions with matter due to their helicity [2]. In addition, this experiment opened a new window for astronomy by looking at the center of the Sun for the first time. After 25 years of data taking, the measured neutrino rate was roughly one third of the predicted rate [1]. This discrepancy was the source of the *solar neutrino problem* and motivated the proposal of further so-called radio-chemical experiments. New detectors based on neutrino capture by Gallium (GALLEX [3]/GNO [4] and SAGE [5]) continued to measure neutrinos from the Sun to learn more about its energy production mechanism. In this case, the capture of ν_e on ^{71}Ga producing ^{71}Ge and an electron was used as detection reaction, with an energy threshold of 233 keV. The results showed again a deficit in the solar neutrino flux compared to the expectations of theoretical solar models.

In 1983, the Kamiokande detector [6] was built in Japan. It used the Cherenkov light emission in water and was originally planned to search for proton decay. Although no proton decay candidates were found, the detector made important astrophysical contributions, e.g., the measurement of the high-energy part of the solar neutrino spectrum [7] and the detection of neutrinos from the supernova explosion SN1987a [8]. Its successor Super-Kamiokande [9] started in 1995 and is still running. The detector consists of a

50 kt water detector and also searches for proton decay. Super-Kamiokande discovered the atmospheric neutrino oscillations [10] in 1998 and is still producing a variety of interesting physics results. Both Kamiokande and Super-Kamiokande measured about half of the predicted neutrino rate. At that time, several theoretical approaches tried to solve the solar neutrino problem relying on either a change of the solar model or a particle-physics effect. In 2001, the solar neutrino mystery was resolved by the results of the SNO experiment [11], a heavy-water detector especially designed to investigate solar neutrinos. By comparing the charged current interaction rates of ν_e with the neutral current ones, where all neutrino flavors ν_x contribute, the SNO experiment could clearly show that ν_e's produced in the Sun oscillate to other flavors. The conclusion was that neutrinos themselves are responsible for the solar neutrino problem. Already at this point, the history of astrophysics showed its potential to discover physics beyond the standard model by looking at astrophysical objects.

Neutrino oscillations imply a mixing of weak eigenstates and mass eigenstates. The weak neutrino eigenstates, which are produced with a definite lepton flavor in weak transitions, are mixtures of states of definite masses. Similar to the Cabibbo-Kobayaski-Maskawa [12] mixing in the quark sector, this mixing can be represented by a matrix [2], which can be parametrized in the form:

$$
\begin{pmatrix} \nu_e \\ \nu_\mu \\ \nu_\tau \end{pmatrix} = \begin{pmatrix} 1 & 0 & 0 \\ 0 & c_{23} & s_{23} \\ 0 & -s_{23} & c_{23} \end{pmatrix} \begin{pmatrix} c_{13} & 0 & s_{13}e^{-i\delta} \\ 0 & 1 & 0 \\ -s_{13}e^{i\delta} & 0 & c_{13} \end{pmatrix} \begin{pmatrix} c_{12} & s_{12} & 0 \\ -s_{12} & c_{12} & 0 \\ 0 & 0 & 1 \end{pmatrix} \begin{pmatrix} \nu_1 \\ \nu_2 \\ \nu_3 \end{pmatrix},
$$

(1.1)

where $s_{ij} = \sin\theta_{ij}$ and $c_{ij} = \cos\theta_{ij}$ with the rotation mixing angles θ_{ij}. The phase δ can describe a possible CP-violation and is usually written together with the θ_{13} terms as both are still unknown values. The most general form of this mixing matrix has a further multiplicative matrix including two additional phases (Majorana phases) which is not shown here.

During its propagation, the neutrino weak states oscillate due to the mass difference between mass eigenstates. If the oscillation problem is simplified to a two-neutrino system, the oscillation probability of a neutrino ν_α of energy E after a propagation distance L can be written as:

$$
P(\nu_\alpha \rightarrow \nu_\beta) \propto \sin^2 2\theta_{ij} \cdot \sin^2\left(1.27\frac{\Delta m_{ij}^2(\text{eV}^2)L(\text{m})}{E(\text{MeV})}\right)
$$

(1.2)

with ν_α and ν_β being the flavor states of the neutrino and $\Delta m_{ij}^2 = m_j^2 - m_i^2$ the mass difference between the mass states ν_i and ν_j[1]. With the measurement of solar neutrino oscillations, the value of θ_{12} and Δm_{12}^2 can be determined while θ_{23} and Δm_{23}^2 arises from atmospheric neutrino oscillations. The combined (global analysis) best values for

---

[1]The derivation of this formula can be found, for example, in [2].

these parameters[2] are:

$$\sin^2 2\theta_{12} = 0.87^{+0.04}_{-0.04} \qquad \Delta m^2_{12} = (7.59 \pm 0.21) \cdot 10^{-5} \, \text{eV}^2 \, [13] \tag{1.3}$$

$$\sin^2 2\theta_{23} > 0.90 \quad \text{at 90\% C.L. } [14] \qquad |\Delta m^2_{23}| = (2.8^{+0.7}_{-0.9}) \cdot 10^{-3} \, \text{eV}^2 \, [15]. \tag{1.4}$$

From the beginning, liquid scintillator experiments have played a major role in the neutrino detection. Reines and Cowan used this technology already in 1956 to prove the existence of neutrinos produced by a power reactor [16]. Concerning oscillations, the best limit for the third mixing angle θ_{13} arises from the CHOOZ experiment [17], located in a reactor complex in the northern part of France:

$$\sin^2 2\theta_{13} < 0.1 \quad \text{for large } |\Delta m^2_{13}| \quad \text{with} \quad |\Delta m^2_{13}| < 7 \cdot 10^{-4} \, \text{eV}^2 \quad \text{at 90\% C.L. } [17]. \tag{1.5}$$

The detector was based on a liquid-scintillator loaded with Gadolinium and investigated the disappearance of $\overline{\nu}_e$. Further reactor-neutrino experiments of this type are planned or already in construction aiming to gain about a factor of 10 in sensitivity compared to CHOOZ and maybe finally measure the value of θ_{13}. Examples of them are Double-CHOOZ [18] and Daya Bay [19].

Currently, two large liquid-scintillator devices are in operation, KamLAND [13] a 1 kt detector placed in the Kamioka mine in Japan and Borexino [20] with 300 t placed at the Gran Sasso underground laboratory in Italy. The KamLAND experiment has precisely measured the mass difference Δm^2_{12} of equation 1.3 by detecting $\overline{\nu}_e$ from power reactors. The detector is placed at a mean distance of about 180 km from the surrounding reactors which allows to measure clearly oscillations due to the relatively large value of θ_{12}. As the oscillations due to θ_{13} are very fast for this reactor-detector distance its contribution averages to 1/2. An important "background" in the low-energy part of the reactor spectrum is the contribution of the neutrinos produced inside the Earth. In the radioactive decay chains of ^{238}U and ^{232}Th, several neutrinos are produced with energies up to 3.3 MeV. Recently, the contribution of these so-called geoneutrinos to the spectrum has been extracted from the data being the first detection of geoneutrinos [21]. The main goal of Borexino [20] is the real-time measurement of the neutrinos produced in different reactions in the Sun, in particular of the monoenergetic ^{7}Be neutrinos. The used detection channel is the elastic scattering of ν_e on electrons where a Compton-like spectrum of the scattered electrons can be measured. As no further signature exists, signals from all present radioactive isotopes decaying in the energy region of solar neutrinos contribute to the background in the experiment. For this reason, low radio-purity levels were one of the main concerns in the detector design. Recently, the first results of real-time measurements of the ^{7}Be neutrinos have been published by the collaboration [22][23]. The precise measurement of ^{7}Be neutrinos is in good agreement with the

---

[2]The value for $\sin^2 2\theta_{12}$ has been calculated from the literature value: $\tan^2 \theta_{12} = 0.47^{+0.06}_{-0.05}$ [13].

neutrino oscillation models and allows to gain valuable information on fusion processes inside the Sun.

By now, although some parameters remain still unknown, the neutrino oscillation picture is quite well established and implies physics beyond the standard model. A large number of *Grand Unified Theories* (GUTs) are being developed to explain open problems in the current standard model. The original unification group $SU(5)$ [24] has been extended, for example, to the larger group $SO(10)$ [25] or to Supersymmetry [26] and include neutrino masses. However, the most dramatic prediction of GUTs, the proton decay [27], still remains undetected. The Super-Kamiokande experiment [28][29] has been searching for such processes via several decay channels but no evidence for proton decay has been found, the current best limits for the proton lifetime being around $10^{32} - 10^{33}$ years. In the recent years, several models pointed out than the proton lifetime could be $\sim 10^{34}$ years [30] and this has therefore motivated the design of new large detectors.

Motivated by the search for proton decay and by the success of the neutrino astronomy field, several large detectors have been proposed in recent years [31][32][33][34][35]. In Europe, three detector concepts have been suggested: MEMPHYS[3], GLACIER[4] and LENA[5]. MEMPHYS [33] is a 500 kt water-Cherenkov detector which is planned to be built in $3-5$ shafts similar to the Superkamiokande detector concept. The main advantage of the detection principle is the direction sensitivity as Cherenkov light is produced within a cone around the particle propagation-axis. This direction can be reconstructed using the distribution and arrival time of the photons in the photomultipliers (PMTs) placed on the walls. GLACIER [34] is foreseen as a 100 kt liquid-Argon time projection chamber (TPC) which has to be built in a cryostat. Two types of signals are recorded for every event: the light emission is detected by PMTs and the ionization signal is extracted by an electric field, amplified and read out. The TPC performance allows for particle tracking and offers a powerful background discrimination. LENA [35][36] is designed as a cylindrical volume of 50 kt liquid scintillator. Its main advantages are a very good energy resolution (expecting ~ 180 photoelectrons per MeV deposited energy) and a low energy threshold. These three proposals have been joint in the LAGUNA[6] [37] group to study the technical feasibility to build a large device underground and to investigate the physics potential with common tools like simulations and background estimations.

The LENA detector has been proposed by the group E15 at the Technische Universität München and has the potential to measure proton decay via $p \rightarrow K^+ \overline{\nu}$ at the level of 10^{34} years lifetime and, in addition, could confirm Super-Kamiokande limits with a different technology. Besides the search for proton decay, several physics goals are aimed

---

[3]MEMPHYS stands for MEgaton Mass PHYSics.

[4]GLACIER stands for Giant Liquid Argon Charge Imaging ExpeRiment.

[5]LENA stands for Low Energy Neutrino Astronomy.

[6]LAGUNA stands for Large Apparatus for Grand Unification and Neutrino Astrophysics.

at, examples are the measurement of the diffuse background of supernova neutrinos, solar neutrinos, and geoneutrinos. The physics potential of the detector strongly depends upon the optical properties of the liquid-scintillator detection-medium. The energy resolution and threshold are directly related to the light yield of the detector. Moreover, for example the position reconstruction or the separation of timely close signals depend on the lifetime of the excited states of the scintillator molecules. Therefore, a good knowledge of the light emission processes and its propagation properties is required.

This thesis focuses on both technical feasibility studies and Monte Carlo calculations, to investigate the physics potential of the LENA detector to search for proton decay. Concerning the technical studies, liquid scintillator measurements have been performed to understand the impact of the detector performance on the physics results. The outline of the work is as follows: chapters 2 and 3 describe the physics goals and the current LENA detector design, respectively. In chapter 4, the basic concepts of the scintillation mechanism in organic liquids are presented while in chapter 5 the detailed description of the studied organic compounds and their handling procedures can be found. Chapters 6 and 7 present the experiments which have been performed to investigate the scintillation-light emission properties. In chapter 8, the discussion of the experimental results can be found. Chapter 9 describes the studies and Monte Carlo simulations performed to evaluate the potential of LENA to detect proton decay. In chapter 9, also the impact of the optical scintillator properties on the physics results is discussed. Chapter 10 gives a short summary of the results of further simulations which focus on the beta-beam detection in LENA. Finally, chapter 11 contains a summary of the thesis and an outlook.

Chapter 2

Physics goals of the LENA experiment

LENA (**L**ow **E**nergy **N**eutrino **A**stronomy) is a proposed large-volume liquid-scintillator multipurpose observatory. Its main aims are the detection of low-energy neutrinos from several astrophysical sources and the search for proton decay. This chapter is a compilation of the physics cases which may be studied with this future detector. While in the first part research fields related to neutrino astronomy are described, in the second part goals related to particle physics are addressed. In chapter 3, the description of the current detector design can be found[1].

2.1   Neutrinos as probes

Neutrinos are weakly interacting neutral particles and can therefore be nicely used in astrophysics as information messengers. While astrophysical charged particles can be bent by magnetic fields and photons can be absorbed in the interstellar medium, neutrinos reach the Earth bringing the whole information (direction and energy) on their production source. By now, neutrinos have been used to investigate the energy production in the Sun, to learn about core-collapse supernova or more recently to gain information on the interior of our Earth. In the following, the potential of the LENA detector to investigate astrophysical objects is summarized. Predictions of neutrino fluxes and rates in the detector are given for the different physics cases.

---

[1]Figure 3.1 shows an artistic representation of the current LENA detector design.

2.1.1 Solar neutrinos

The Sun loses energy by radiation, but remains stable due to the production of energy via hydrogen burning. The main burning cycle in the Sun is called *pp-cycle* where hydrogen is fused to helium. The net reaction can be written as:

$$4\text{H} + 2e^- \rightarrow {}^4\text{He} + 2\nu_e + 26.73\,\text{MeV}. \tag{2.1}$$
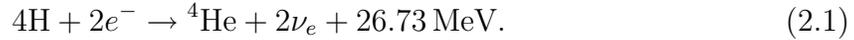
Within this cycle, neutrinos from several reactions are produced. Figure 2.1 shows the theoretical neutrino spectra calculated by [38]. Contributions from the already men-
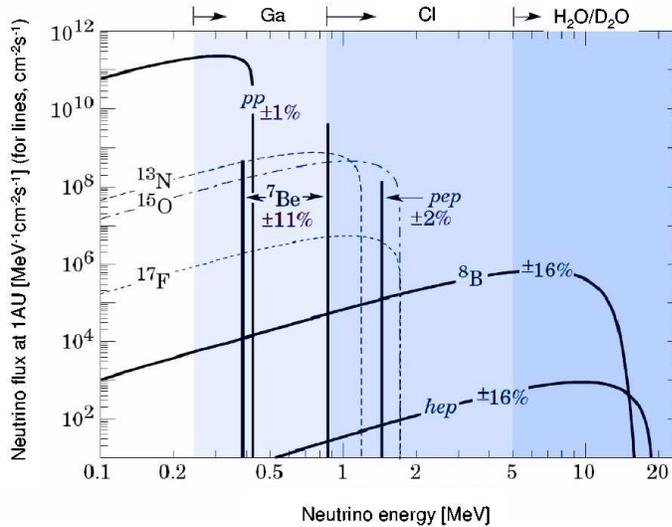
Figure 2.1: The solar neutrino energy spectrum on the Earth as predicted by the current solar standard model [38]. Contributions from the pp-chain branches are plotted as solid lines, the CNO contributions as dotted lines. The top part of the diagram illustrates from left to right the energy threshold for the gallium (GALLEX [3], GNO [4], SAGE [5]), chlorine (Homestake [39]), as well as water (Superkamiokande [9]) and heavy water (SNO [11]) experiments.

tioned pp-chain are plotted as solid lines. The names of the different contributions (pp, ^{7}Be, pep, ^{8}B, hep) arise from the corresponding production reaction. Furthermore, the Sun can burn hydrogen also through the *CNO-cycle*. The spectra of the thereby produced neutrinos are represented with dotted lines. However, the CNO-cycle provides only a small contribution to the total energy production in the Sun (about 2%). On the top of the diagram the energy thresholds for the gallium (GALLEX [3], GNO [4], SAGE [5]), chlorine (Homestake [39]), as well as water (Superkamiokande [9]) and heavy water (SNO [11]) experiments are illustrated. The radio-chemical experiments using Ga and Cl have a low-energy threshold but measure the integrated neutrino flux. In

contrast, the experiments using Cherenkov light in water or heavy water measure spectroscopically, however only above $\sim 5\,\mathrm{MeV}$.

Recently, the Borexino liquid-scintillator experiment has made the first real-time measurement of the low-energy part of the solar neutrino-spectrum [22][23]. Borexino has a fiducial volume of $100\,\mathrm{t}$ and it is built with high radio-purity to allow for low-energy neutrino detection. Already after 2 months of measuring time, a clear signal of ^{7}Be neutrinos could be extracted from the data. A rate of $47\pm3\pm4$ counts/$(\mathrm{d}\cdot100\,\mathrm{t})$ has been observed [23]. From this precise measurement, information on the fusion processes inside the Sun can be gained. In addition, the neutrino oscillations can be tested. The measured ^{7}Be neutrino rate is in agreement with the predictions from [40][41]. Solar neutrino oscillations occur inside the Sun. When a neutrino leaves the Sun's surface, the mass eigenstates do not overlap anymore. However, the oscillations on the way out of the Sun are affected by the high solar matter densities as ν_e in contrast to ν_μ and ν_τ can interact with e^- via $\nu_e + e^- \rightarrow \nu_e + e^-$ by charged current interaction. This effect is energy dependent and was first described by Mikheyev, Smirnov, and Wolfenstein being usually called MSW effect [40][41]. It strongly influences ν_e oscillations above $\sim 1\,\mathrm{MeV}$ and for this reason, the mono-energetic ^{7}Be line at $862\,\mathrm{keV}$ is of great interest as it is located in the transition region between matter-dominated and vacuum-dominated oscillations. The LENA detector would be able to detect these solar ^{7}Be neutrinos via neutrino electron scattering with a rate of ~ 5400 events/day in a fiducial volume of $18\,000\,\mathrm{m}^3$. In this energy region, the main background sources are decays from naturally contained isotopes as ^{210}Po, ^{210}Bi and ^{85}Kr. Depending on the signal-to-background ratio, the ^{7}Be measurement would provide a sensitivity for time variations in the ^{7}Be neutrino flux of $\sim 0.5\%$ during one month of measuring time. Such a sensitivity may give information on helioseismology at a unique level, being able to resolve pressure or temperature fluctuations in the center of the Sun which would cause time-fluctuations of the ν flux.

In addition, the detection of pep-neutrinos (see figure 2.1) with a calculated rate of about 210 events/day could provide further information on neutrino oscillations. This mono-energetic contribution appears in an energy region where the transition from matter-induced oscillation to vacuum oscillation is expected due to the above mentioned MSW effect [40][41], i.e. between $1-2\,\mathrm{MeV}$. The ratio of the neutrino fluxes from the reactions of pep fusion and pp fusion is theoretically determined with an accuracy $\leq 1\%$. Thus, the measurement of the pep neutrinos could also deliver information on the solar pp-neutrino flux. The neutrino flux from the CNO-cycle is theoretically predicted with the lowest accuracy (30%) of all solar neutrino fluxes. The detection of CNO-neutrinos would help to better understand this energy-production cycle. In principle, there is an energy window above $700\,\mathrm{keV}$ for the detection of pep and CNO neutrinos where there is only a small background contribution due to intrinsic ^{40}K and ^{210}Bi. However in this region, the muon-induced cosmogenic backgrounds of ^{11}C and

[10]C are expected. For the location in Pyhäsalmi, a signal-to-background ratio of about 1/3 is expected. To calculate this ratio, the muon flux [42] and the calculated muon mean energy [43] have been taken and compared with the feasibility measurements for the Borexino experiment [44]. In addition, the three-fold coincidence method developed by the Borexino Collaboration [45] could be used to further reduce the background. In this method, coincidences between crossing muons and spallated neutrons are used to reject ^{11}C candidates.

Furthermore, a liquid scintillator contains ^{13}C atoms at a natural abundance of 1% which can be used as target for [8]B neutrinos [46] as the energy threshold is 2.2 MeV. Around 360 events per year of this type are estimated for LENA. A deformation due to the MSW-effect [40][41] should be observable in the low-energy regime of the [8]B neutrino spectrum after a couple of months of measurements.

2.1.2   Supernova neutrinos

In 1987, neutrinos from a core-collapse supernova explosion were detected for the first time. The supernova SN1987A was located in the Large Magellanic Cloud and the neutrinos produced were detected by the Kamiokande II [8] and the IMB (Irvine-Michigan-Brookhaven) [47] experiments. With a total of 19 events, these detectors could give a first hint to the role of neutrinos in such a supernova explosion. A high statistics measurement of neutrinos produced by a core-collapse supernova could deliver information on the details of the supernova explosion-mechanism. Current supernova explosion models [48][49][50] differ significantly in the prediction of neutrino mean energies of different neutrino flavors (ν_e, ν_μ and ν_τ) and types (ν and $\overline{\nu}$). For example, the predicted mean energies for $\overline{\nu}_e$ varies between 11.4 [49] and 15.4 MeV [50]. Spectroscopy measurements of the neutrinos arriving from a supernova explosion could test these calculated mean energies.

For a 8 $M_\odot$ star in the center of our galaxy ($\sim$ 10 kpc distance), about 10 000 to 15 000 neutrinos are expected in the LENA detector [51] depending on the model used for the calculations. In a liquid-scintillator detector, several detection reactions allow separate measurements of ν_e, $\overline{\nu}_e$ and the sum of the remaining flavors. Table 2.1 summarizes the main reaction channels with the expected rates for a 8 $M_\odot$ star in the center of the galaxy. The given ranges account for predictions of different supernova explosion models and neutrino oscillation scenarios (resonances inside the supernova depending on θ_{13} and the neutrino mass hierarchy [51]). The neutrinos denoted by ν represent the sum of all neutrino types: $\overline{\nu}_e$, ν_e, $\overline{\nu}_\mu$, ν_μ, $\overline{\nu}_\tau$, ν_τ. A measurement of the fluxes for $\overline{\nu}_e$, ν_e and ν is possible with the LENA detector. Unfortunately, the determination of the ν_e flux is affected by a large error. The reason is the similar signature of reactions (2) and (3) in table 2.1, as in both cases a delayed coincidence is recorded with a time delay of 20.2 and 11.0 ms, respectively,[52]. Moreover, the threshold for both reactions is also

Detection reaction	Expected rate
(1) $\overline{\nu}_e + p \rightarrow n + e^+$	7 500 - 13 800
(2) $\overline{\nu}_e + ^{12}\text{C} \rightarrow ^{12}\text{B} + e^+$	150 - 610
(3) $\nu_e + ^{12}\text{C} \rightarrow ^{12}\text{N} + e^-$	200 - 690
(4) $\nu_e + ^{13}\text{C} \rightarrow ^{13}\text{N} + e^-$	$\mathscr{O}(10)$
(5) $\nu + ^{12}\text{C} \rightarrow \nu + ^{12}\text{C}^*$	680 - 2 070
(6) $\nu + e^- \rightarrow \nu + e^-$	680
(7) $\nu + p \rightarrow \nu + p$	1 500 - 5 700
(8) $\nu + ^{13}\text{C} \rightarrow \nu + ^{13}\text{C}^*$	$\mathscr{O}(10)$

Table 2.1: Typical event rates in LENA for a supernova explosion of $8\,\text{M}_\odot$ in the center of our galaxy [51]. The given ranges account for predictions of different supernova explosion models and neutrino oscillation scenarios. ν represents the sum of all neutrino types: $\overline{\nu}_e$, ν_e, $\overline{\nu}_\mu$, ν_μ, $\overline{\nu}_\tau$, ν_τ.

similar: 14.4 and 17.3 MeV, respectively. To disentangle these fluxes, information about the $\overline{\nu}_e$ flux can be taken from reaction (1). However, to calculate the expected rate of reaction (3), a good knowledge on the reaction cross sections is required. Currently, the neutrino cross-section measurements [52] give a combined accuracy of only 6.7%. The uncertainty on the determination of the ν_e flux with this method is between 8 and 11% depending on the measured rates. Future measurements of neutrino cross-sections [53] could reduce this uncertainty.

In a recent work [51], the expected neutrino rates from a supernova have been evaluated taking into account several oscillation scenarios. The value of θ_{13} has been varied and normal and inverted hierarchy have been considered in the rate predictions. The neutral current reactions (5), (6), (7) and (8) are insensitive to flavor and therefore to oscillations. Their fluxes offer the possibility to discriminate different supernova explosion models (more information about these models is given in section 2.1.3). Besides the flux measurements, as the time resolution of a liquid scintillator detector is quite precise ($\sim$ few ns), the evolution of the arrival times of the neutrinos can be studied. This evolution could be compared with that of supernova simulations [54] in order to learn details of the core-collapse process.

For a supernova explosion where the neutrinos cross the Earth before being registered in the detector, neutrino oscillations in the Earth matter can be studied [55]. Due to these oscillations, modulations in the detected energy spectra are expected. Their detection would enable to put a limit on the neutrino mixing angle θ_{13} and to identify whether the neutrino mass hierarchy is normal or inverted [55]. A large scintillator detector like LENA offers the required energy resolution to identify the mentioned oscillations in the spectrum.

2.1.3   Diffuse supernova neutrino background

During the history of the Universe, core-collapse supernova explosions have produced neutrinos and anti-neutrinos in all types and flavors: the *diffuse supernova neutrino background* (DSN). By now, no positive signal of such neutrinos has been obtained [56]. A measurement of DSN neutrinos would represent an exciting discovery. Moreover, it will provide information on the supernova explosion mechanism, i.e. on the mean energy of the produced neutrinos, even in the absence of a current explosion.

A large-volume detector is an ideal device to search for the DSN. Currently, the best upper limit on the measurement of the DSN flux comes from the Super-Kamiokande water-Cherenkov experiment [56] being $1.2\,\overline{\nu}_e\,\mathrm{cm}^{-2}\,\mathrm{s}^{-1}$ for energies above $19.3\,\mathrm{MeV}$. This lower energy limit is due to the background of spallation products induced by cosmic muons [57]. In a liquid scintillator detector [58], the capture of $\overline{\nu}_e$ by a free proton can be used to tag such events as it has the largest cross section in this energy region:

$$\overline{\nu}_e + p \to n + e^+, \quad n + p \to d + \gamma(2.2\,\mathrm{MeV}). \tag{2.2}$$
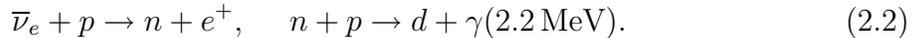
The positron provides a prompt signal of at least $1\,\mathrm{MeV}$ due to the e^+e^- annihilation. The neutron is later (after $\sim 180\,\mu\mathrm{s}$) captured on a free proton producing a $2.2\,\mathrm{MeV}$ gamma. This delayed coincidence provides a clear signature to separate such events from background interactions. The almost background-free energy window from ~ 10 to $25\,\mathrm{MeV}$ for the DSN detection is determined by the background contribution from reactor and atmospheric $\overline{\nu}_e$ in that region.

In figure 2.2, a spectrum of the expected neutrino rate is given for the Pyhäsalmi location in Finland[2]. The blue band represents the theoretically favored region for the DSN flux together with the upper limit from Superkamiokande [56]. The black lines show the background from reactor and atmospheric neutrinos. The lines denoted by LL, KRJ and TBP correspond to different supernova explosion models, i.e. Lawrence Livermore [48], Keil, Raffelt, Janka [49] and Thompson, Burrows, Pinto [50]. The resulting DSN flux was calculated in [57]. For the location in Pyhäsalmi, the expected number of $\overline{\nu}_e$ events after $10\,\mathrm{years}$ measuring time is $60-130$ for different supernova explosion models, considering the most probable value for the star formation rate [58]. The expected background rate for this period is 13 events which arise not only from reactor and atmospheric neutrinos but also from muon-induced fast neutrons which can mimic the signature. If no signal is detected, a new limit of $0.13\,\mathrm{cm}^{-2}\,\mathrm{s}^{-1}$ for the flux above $19.3\,\mathrm{MeV}$ could be achieved. Between 10.5 and $19.3\,\mathrm{MeV}$, the limit would be set to $0.3\,\mathrm{cm}^{-2}\,\mathrm{s}^{-1}$. Neutrino scattering on carbon ($^{12}\mathrm{C} + \nu_e \to\,^{12}\mathrm{N} + e^-$) has also been considered in the literature [59] as a way to measure DSN. In this paper [59], the authors have calculated a rate of $2-3$ events for $10\,\mathrm{years}$ in the fiducial volume of LENA, again considering the most probable value of the star formation rate.

---

[2]More information on detector locations can be found in chapter 3.
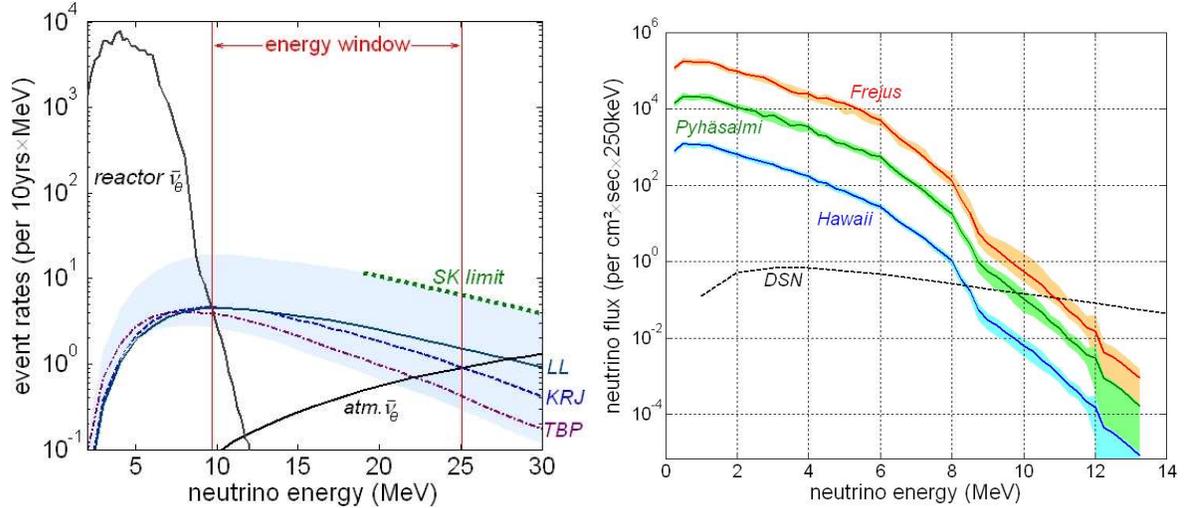
Figure 2.2: Left: $\overline{\nu}_e$ of the diffuse supernova neutrino background spectrum for three different supernova explosion models: LL [48], KRJ [49] and TBP [50]. The background from reactor and atmospheric $\overline{\nu}_e$ is also included. Right: shape of the reactor anti-neutrino spectrum at various detector locations. Figures from [58].

Making no further assumptions on the future knowledge on the supernova rate, for 50 measured events, the mean energy of the $\overline{\nu}_e$ spectrum could be determined at a level of $+50\% -30\%$ [60]. However, the progress in optical observations of the star formation for the visible [61], ultraviolet [62] and infrared [63] regions may provide an improved prediction for the star formation rate which is closely linked to the supernova rate. As a result, more stringent constraints on the supernova explosion models can be derived. In addition, assuming the total binding energy of a supernova to be equally distributed between the 6 neutrino types and flavors [64], the supernova explosion rate could be tested with the $\overline{\nu}_e$ signal. This measurement will provide complementary information to the direct observational methods.

2.1.4 Geoneutrinos

Radioactive decays from the uranium and thorium chains are responsible for part of the heat production inside the Earth due to the energy deposition of several α- and β-particles (with few-MeV energy) within the decay chains. The measured heat flow emitted by the Earth's surface is around 40 TW, but it is still unknown what part of this heat arises from radioactivity. However, in several stages of the decay chains anti-neutrinos are produced (in β-decays), offering a new way to investigate our Earth.

In summer 2005, the first measurement of the so-called geoneutrinos was performed

by the KamLAND experiment [21]. KamLAND is a 1 kt liquid-scintillator detector in Japan which main aim is to measure oscillations of reactor anti-neutrinos. At an early stage, geoneutrinos were a background in the low-energy region of the reactor-neutrino spectrum. At present, the signal of the geoneutrinos and reactor $\overline{\nu}_e$ can be separated allowing first estimates of the Earth's U/Th content. Figure 2.3 shows on the left the theoretical spectra of the anti-neutrinos produced by radioactive decays of uranium, thorium and potassium inside the Earth [21]. The black line at 1.8 MeV depicts the
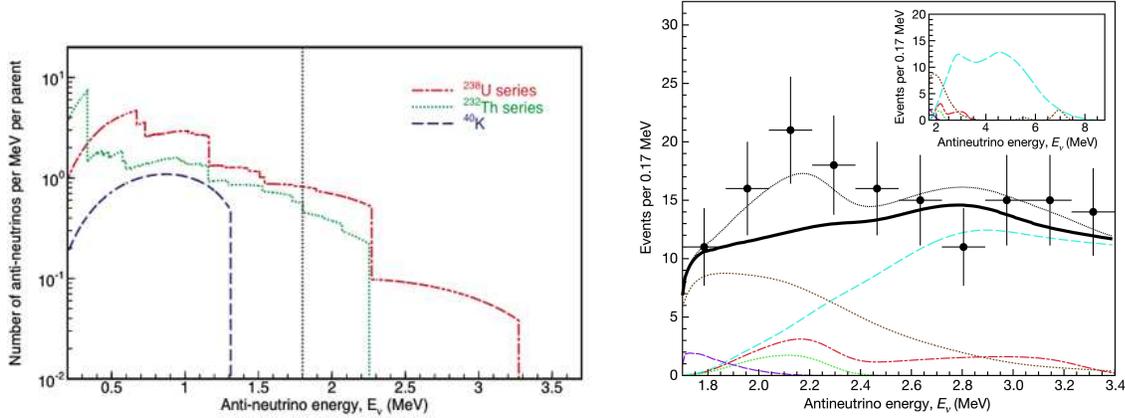
Figure 2.3: Left: theoretical spectra of the anti-neutrinos produced by radioactive decays inside the Earth. Right: anti-neutrino spectrum at low energies measured by KamLAND. The expected signals from geoneutrinos are the red dot-dashed line for ^{238}U and the dotted green line for ^{232}Th. For further description see text. (Pictures from [21]).

threshold of the detection reaction, the inverse beta decay (see equation 2.2). On the right, the measured $\bar{\nu}_e$ energy spectrum in KamLAND [21] is shown for low energies. In the main panel, experimental points are displayed along with the expectation considering all signal and background contributions (black dotted line). Also shown are the total expected spectrum excluding the geoneutrino signal (black thick solid line), the expected signals from ^{238}U (red dot-dashed line) and ^{232}Th (dotted green line) geoneutrinos. The background contributions due to reactor $\bar{\nu}_e$ (blue dashed light line), ^{13}C $(\alpha, n)\,^{16}$O reactions (brown dotted line), and random coincidences (purple dashed line) are plotted as well. In the inset, the expected spectra extended to higher energies are shown. The geoneutrino spectra are calculated [21] from the so-called reference model for geoneutrinos which assumes 16 TW of radiogenic power from ^{238}U and ^{232}Th.

LENA could make the next step in the investigation of geoneutrinos, as around 1 000 events per year are expected [65] for a detector located in Finland. The event rate depends on the detector site as the amount of radioactive elements in oceanic and

continental crust differs. For a location on the oceanic crust, for example in Hawaii, the event rate drops to about 300 events per year [65]. The detection reaction is the capture of $\overline{\nu}_e$ on free protons present in the liquid scintillator (see equation 2.2). Currently, the Borexino detector is taking data and results of geoneutrino measurements are expected to be published in the close future. In its fiducial volume of 100 tons, about 10 geoneutrinos per year are expected. Once LENA is taking data, the results of these three experiments could be combined to determine the distribution of the radioactive isotopes in both the oceanic and the continental crust. Thereby, knowledge on the contribution to the $\overline{\nu}_e$ flux in the mantle and the core of the Earth could be obtained. Besides the determination of the event rate, spectroscopy of the emitted positron can be performed. While the neutrino spectrum of the uranium chain extends to about 3.3 MeV, the spectrum of thorium ends at about 2.3 MeV (see left panel in figure 2.3). Due to the good energy resolution of the liquid scintillator, both contributions could be disentangled and information on the relative abundances of uranium and thorium isotopes could be gained.

2.2 Particle physics

A large-scale detector like LENA can also be used to explore physics phenomena beyond the standard model of particle physics. The search for proton decay will either result in the discovery of the proton lifetime or will at least more strongly constrain current theoretical predictions. Furthermore, the neutrino oscillations parameters can be studied by the measurement of neutrinos from several sources: accelerator neutrino-beams, reactor $\overline{\nu}_e$ or neutrinos produced in the atmosphere. An overview of the potential of LENA concerning the search for physics beyond the standard model is given in this section.

2.2.1 Proton decay

Proton decay is a baryon number violating process which is predicted by all Grand Unified Theories beyond the standard model [27]. As mentioned above, an observation of the proton decay would deliver valuable information on particle physics models. For LENA, the proton decay reaction $p \rightarrow K^+\overline{\nu}$ has been examined in detail [66]. A sensitivity of $4 \cdot 10^{34}$ y for the lifetime of the proton has been calculated. This value is already in the order of magnitude of several theoretical predictions. In addition, other proton and baryon number violating neutron decay channels could be tested with LENA. The analysis of the nucleon decay sensitivity in LENA is a main objective of this thesis. A theoretical introduction, a summary of the current experimental situation, and an analysis of the signals of several nucleon decay processes in a large liquid-scintillator detector are presented in chapter 9.

2.2.2 Neutrino oscillations with beta beams

One of the missing parameters in the neutrino mixing matrix (see chapter 1) is the angle θ_{13}. In addition to the planned reactor-neutrino experiments [18][19], accelerator-based ideas have been discussed [67][68][69] to determine θ_{13}. *Beta beams* [70] are a possibility which uses accelerated radioactive ions as source of neutrinos (β^+ decay for the production of ν_e and β^- decay for $\overline{\nu}_e$). A first brief study about the capabilities of the LENA detector to detect neutrino oscillations by using beta beams has been performed within this thesis. Chapter 10 describes the beta-beam concept, its possible realization, the simulation work carried out here and the first conclusions.

2.2.3 Reactor neutrinos

The determination of the solar oscillation parameters Δm^2_{12} and Θ_{12} has been investigated [71][72] by using $\overline{\nu}_e$ from power reactors.

In [71], the authors consider neutrino oscillations for a large liquid-scintillator detector like LENA located in the French Fréjus underground laboratory [73]. The effective reactor power of 56 reactors has been calculated at the Fréjus site. The $\overline{\nu}_e$ flux is $W = 3.4\,\mathrm{MW\,km^{-2}}/(4\pi)$ taking an average traveled-distance of 299 km. However, the closest four reactors contribute with around 70 % of the total flux. In this setup, about 17 000 events per year are expected in the fiducial volume (44 kt) of LENA. In addition to the high statistics, the liquid scintillator technology profits from a very good energy resolution of $10\,\%/\sqrt{E_p[\mathrm{MeV}]}$. After one year of measuring time, a $3\,\sigma$ uncertainty below $3\,\%$ on Δm^2_{12} and $20\,\%$ on θ_{12} results [71]. If several years are considered (about 7 years), the uncertainties decrease to $1\,\%$ and $10\,\%$ respectively. The present 3σ uncertainties for these parameters are $\sim 11\%$ and 25%, respectively.

The authors of [72] have also studied the precision which can be achieved for the solar parameters by using either a mobile reactor or a conventional power station. In addition, new ideas concerning reactor neutrino oscillations due to θ_{13} to be measured with a large liquid scintillation detector (45 kt) and a mobile $\overline{\nu}_e$ source are discussed. For a nuclear powered ship as a source for $\overline{\nu}_e$, a sensitivity of $\sin^2 2\theta_{13} < 0.004$ can be achieved at 90% confidence level [72].

2.2.4 Atmospheric neutrinos

In LENA, about 10 fully contained (FC) events per day are expected for a neutrino energy range from 100 MeV to 25 GeV [74]. Although no simulations have been carried out so far, LENA may be able to investigate neutrino oscillations. Similar to the case of the beta beam detection (see section 10.1), future feasibility studies have to show the tracking capabilities of the detector to determine a directional resolution and energy-

reconstruction potential of the LENA detector. Nuclear physics effects as the Fermi motion and hadron production have to be evaluated as well.

2.2.5 Indirect detection of dark matter

The existence of dark matter in the Universe is strongly motivated by cosmological [75] and astrophysical measurements [76]. Although several heavy particles have been proposed, also light particles are under discussion [77]. In [78], the authors have studied the signature and the sensitivity of LENA to search for MeV dark matter particles. To this end, the signal of neutrinos resulting from dark matter annihilation, $\chi\chi \rightarrow \nu\nu$, in the Milky Way is investigated. Due to the good energy resolution and the clear signature of $\overline{\nu}_e$ in LENA, the detector would have the capability to find a positive signal in a large part of the mass region of interest $(10 - 100\,\mathrm{MeV})$.

Chapter 3

The LENA detector design

The proposed LENA observatory is a large-volume organic liquid-scintillator device which has to be placed in an underground location. A cylindrical shape with a mass of 50 kt has been proposed [79] as this is the minimum required to achieve the desired physics goals. The physics program of LENA (see chapter 2) comprises mainly neutrino astronomy and the search for proton decay. In the first part of this chapter, the capabilities of the detector demanded by the physics are outlined. In a second part, the current technical design is presented which is different from the one described in previous works [36][58] as a recent underground construction study [80] has constraint the old design.

3.1   Requirements

This section summarizes the main pre-requisites which have to be fulfilled in the detector design. First, the shielding against cosmic muons is considered making constraints on the detector location i.e. underground depth. Later, conditions for the radio-purity of the detector materials and optical properties of the liquid scintillator are introduced.

3.1.1   Cosmic muon shielding

In order to have a good shielding against cosmic muons, an underground (or under-water) location is necessary. The physics potential of the LENA detector explained in chapter 2 has been evaluated assuming 4 000 meters water equivalent (m.w.e.) shielding corresponding to about 1.5 km depth of rock. At this depth, for standard rock a muon flux of $\sim 10\,\mathrm{m}^{-2}\,\mathrm{d}^{-1}$ is expected. To tag these remaining muons, an active outer veto is desired which can be made either of water or liquid scintillator.

Muon-induced neutrons constitute the most delicate background for all measure-

ments where electron anti-neutrinos, $\overline{\nu}_e$, are involved. This is the case for the diffuse background of supernova neutrinos, geoneutrinos, and reactor neutrinos. Muons crossing the surrounding rock can produce spallation processes leading to high-energy neutrons (up to $1\,\text{GeV}$). These neutrons can enter the detector without leaving a signal in the outer veto. Their elastic scattering on protons can produce a signal in the scintillator which corresponds to the sum of all recoiling protons. After thermalization, the neutrons are captured on protons producing a $2.2\,\text{MeV}$ γ-ray. The signal from the recoil protons accompanied by the delayed neutron-capture mimic exactly the $\overline{\nu}_e$ signature:

$$\overline{\nu}_e + p \rightarrow e^+ + n, \qquad n + p \rightarrow d + \gamma \ (2.2\,\text{MeV}). \tag{3.1}$$

The $\overline{\nu}_e$ signature consists of a delayed coincidence: the prompt signal of the e^+ is followed by a gamma of $2.2\,\text{MeV}$ after $\sim 180\,\mu\text{s}$.

In addition, muons can produce long-lived radioactive isotopes in the detector volume due to reactions on ^{12}C. The decay of such isotopes produces a low-energy electron signal in the energy window where the search for solar neutrinos takes place. The Borexino Collaboration has studied these isotopes in detail[44]. Most important are ^{11}C and ^{10}C as they have a relatively long lifetime ($20.4\,\text{min}$ and $19.3\,\text{s}$, respectively). The energy of the emitted positron is 0.96 and $1.9\,\text{MeV}$, respectively. These energies correspond to the energy region in which pep- and CNO-neutrinos can be measured (see section 2).

3.1.2 The detection of $\overline{\nu}_e$

The measurement of $\overline{\nu}_e$ both from the diffuse background of supernova neutrinos in the Universe and from natural radioactivity inside the Earth are important goals of the LENA project. However, in the energy region between $\sim 2-10\,\text{MeV}$, anti-neutrinos from power reactors dominate the spectrum. As the flux of reactor neutrinos is dependent on the location (see figure 2.2) places close to reactors are disfavored.

On the other hand, reactor neutrinos could be used to measure neutrino oscillation parameters (Δm_{12}^2 and θ_{12}) precisely [71][72] (see section 2.2.3). In that case, a location close to power reactors might be preferred.

3.1.3 Low radioactivity environment

As reported in chapter 2, the high statistics measurement of solar neutrinos is a desired aim of the LENA project. Neutrinos from the Sun interact via elastic scattering with the e^- in the detector liquid producing a Compton-like spectrum. Unfortunately, the liquid-scintillator detector technology does not provide directional information. Therefore, the natural radioactive background producing electrons, positrons, and α-particles contributes to the background of this measurement.

Radioactive background can be classified into metal and gaseous isotopes. The metal impurities are mainly found in the detector equipment, e.g., the steel tank or the photo-multiplier tubes. The most dangerous impurities are ^{40}K, ^{238}U and ^{232}Th as their decay (or the decay of daugther particles) produce a signal below 1.5 MeV which corresponds to the solar neutrino detection window. Within the Borexino experiment [22], several measurements were performed during the design phase in order to determine the amount of radioactive impurities of all materials used [81]. Special attention has to be paid to the detection medium itself. In Borexino, the scintillator purity-requirements were set to $7.8 \cdot 10^{-15}$ for ^{40}K, $2.3 \cdot 10^{-17}$ for ^{238}U and $5.8 \cdot 10^{-16}$ g/g for ^{232}Th. Similar purity levels should be achieved in LENA to meet the desired physics goals.

The most dangerous gaseous impurity is radon (^{222}Rn) which is a noble gas that belongs to the uranium chain. Underground sites are rich in radon as the isotope is produced in the surrounding rock and diffuses very easily. For this reason, the tightness of the scintillator container or the detector itself is a critical issue. The radon decay chain consists of several fast decays until the ^{210}Po isotope is produced which has a lifetime of 22 years. Within this decay chain, the isotopes ^{210}Po and ^{210}Pb lead to signals in the neutrino detection region: α-decay of 5.4 MeV (0.4 MeV visible energy due to alpha quenching[1]) and β-decay with 1.16 MeV endpoint energy, respectively. Both contributions appear in the ^{7}Be-neutrino energy window. In addition to radon, the gaseous impurities ^{85}Kr and ^{39}Ar can diffuse to the detection volume and produce again a signal in the region of interest. However, both isotopes can be removed efficiently by bubbling nitrogen through the liquid.

3.1.4 Optical properties of the detection liquid

The optical properties of the detector liquid determine the energy threshold of the detector as well as the energy and time resolutions and the position reconstruction potential. The most important parameter of a scintillation material is the light yield, i.e. the number of photons produced by the energy deposition of a given charged particle. The light yield is usually given as the number of photo-electrons produced in the cathode of the PMTs (photo-electrons per MeV, pe/MeV) having therefore included the efficiency of the PMTs. To achieve a good energy resolution and low threshold, a high light yield is necessary. To this end, the efficiency of the conversion from deposited energy to scintillation light should be high. Additionally, the energy transfer processes and the light propagation (absorption length) have to be optimized to avoid photon losses.

As mentioned in chapter 2, position reconstruction of the events is necessary to separate simultaneous signals and to define the sensitive volume. The position reconstruction relies on the distribution of the detected photons and on having prompt ($\sim$ ns) scintilla-

---

[1] Alpha quenching is referred to as the loss of visible light. The explanation of this effect can be found in chapter 4.

tion signals [51]. Scattering processes smear out the information on the emission position and result in broader pulses. Long scattering lengths (at least 20 m) are therefore essential. The search for proton decay via $p \rightarrow K^+\overline{\nu}$ (chapter 9) demands a good time resolution as well, i.e. of a few ns, in order to separate the Kaon signal from its decay products. For this reason, the main fluorescence decay time of the scintillator should be short (see chapter 4). Furthermore, the energy transfer processes and the light propagation should be optimized to have a fast detector response. This timing requirement has been studied experimentally within this thesis. The description of the experiments performed and the results can be found in chapters 6, 7 and 8.

A liquid scintillator for a detector application consists of a liquid solvent and one or more organic powder solutes (see chapter 5). The concentration of the solute should be uniform throughout the whole detector as the light yield depends on its concentration (see chapter 6). To guarantee this homogeneous concentration, the temperature gradient along the whole detector should be smaller than 1°C. Moreover, as such a large neutrino observatory is planned to run about 30 years, the quality of the detection medium should not decrease with time. That means, long-term stability has to be taken into account in the choice of the liquid scintillator. In addition, all materials which are in contact with the liquid should be tested to be compatible with it and not to cause any degradation of the liquid on a long time-scale.

3.1.5 Photo-sensors performance

The scintillation light emitted by the target liquid is, so far, planned to be detected by photomultiplier tubes (PMTs). To obtain a significant coverage (typically 30%) at reasonable costs, large-area PMTs would be the most reasonable solution. Two approaches can be considered: 12' diameter PMT-cathode used in combination with light concentrators [82] or PMTs of 20' diameter cathode. Currently, the efficiency of PMTs for light detection is limited by the cathode conversion efficiency and by the proper focusing of the photo-electrons into the first dynode. However, new developments in this field have been achieved in 10' diameter PMTs and efficiencies of 35 to 45% have been obtained [83].

A further constraint to avoid large random coincidence rates is an, as low as possible, dark current of the PMTs. Temperatures of less than 20°C would favor a low dark-current rate. Finally, the time resolution of the PMTs (time jitter) should not be much larger than 1 ns in order to avoid the smearing out of the photon arrival times.

3.2 Current design

The possible detector locations under discussion are described in this section. The current technical design of LENA is presented as well.

3.2.1 Detector location

Several locations have been discussed for the future LENA observatory. The main constraints arise from the depth, $\overline{\nu}_e$-background from nearby reactors and the accessibility. Within the LAGUNA [37] European design-study (see chapter 1), six locations in Europe have been discussed (Canfránc [84] (Spain), Boulby [85] (England), Fréjus [73] (France), Polkowice-Sieroszowize [37] (Poland), Slanic [37] (Romania) and Pyhäsalmi [86] (Finland)). While Canfránc and Fréjus are placed under a mountain and can be reached by a road tunnel, the rest are underground mines. Due to the depth of the locations considered in this study, actually only the locations in France and Finland should be considered for LENA.

The *Laboratoire Souterrain de Modane*: Fréjus is located in a highway tunnel below the Alps between France and Italy. It has an overburden of $1\,700\,\text{m}$ of rock what corresponds to $4\,800\,\text{m.w.e.}$ The corresponding muon flux is $4\,\text{m}^{-2}\,\text{d}^{-1}$ and the reactor $\overline{\nu}_e$-flux is $1.6 \cdot 10^6\,\text{cm}^{-2}\,\text{s}^{-1}$. Currently, several experiments are running in the existing experimental hall and an expansion of the lab is planned. The *Center for Underground Physics in Pyhäsalmi mine* (CUPP) is placed in the middle of Finland close to the Pyhäjärvi lake. CUPP's lowest-level is at $1\,440\,\text{m}$ depth ($4\,000\,\text{m.w.e.}$) and there the muon flux is $8.6\,\text{m}^{-2}\,\text{d}^{-1}$. The reactor $\overline{\nu}_e$-flux at this location is $1.9 \cdot 10^5\,\text{cm}^{-2}\,\text{s}^{-1}$ and the access is both by road tunnel and by lift. From December 2007 to May 2008, a pre-feasibility study for the LENA detector at the Pyhäsalmi site has been carried out by the Rockplan engineering company [80].

In addition to the locations of this design study, other locations are also considered. A possibility would be an under-water location (at least $4\,000\,\text{m}$ depth) in the Mediterranean Sea close to the Nestor base [87] in Pylos (Greece). A similar initiative (liquid scintillator detector of $10\,\text{kt}$) is carried out by the Hano-Hano [88] detector proposal for a location close to the coast of Hawaii.

3.2.2 Technical design

At present, only a pre-design study for the Pyhäsalmi location exists [80] and for this reason, the design is based on conditions from this site. For the locations at Fréjus or underwater close to the Nestor base, similar studies should be performed in order to define the final detector design.

The current detector design [80] is based on a vertical cylinder with a diameter of 30 m and a height of approximately 100 m. This orientation is favorable for the construction of the underground cavity and the stainless steel tank where the sensitive liquid is contained. The underground cavern is designed with an egg-like shape of a maximum diameter of about 45 m and a height of $\sim$ 105 m. This is the most stable cavern-configuration to hold the rock pressure at approximately 1450 m depth. To design the exact shape, the rock in the surroundings of the Pyhäsalmi mine has been considered.

The inner volume is filled with about 50 kt of liquid scintillator, the exact composition being still under discussion (see chapter 8). In figure 3.1, an artistic representation of the LENA detector is given. The inner volume is filled with organic liquid-scintillator which
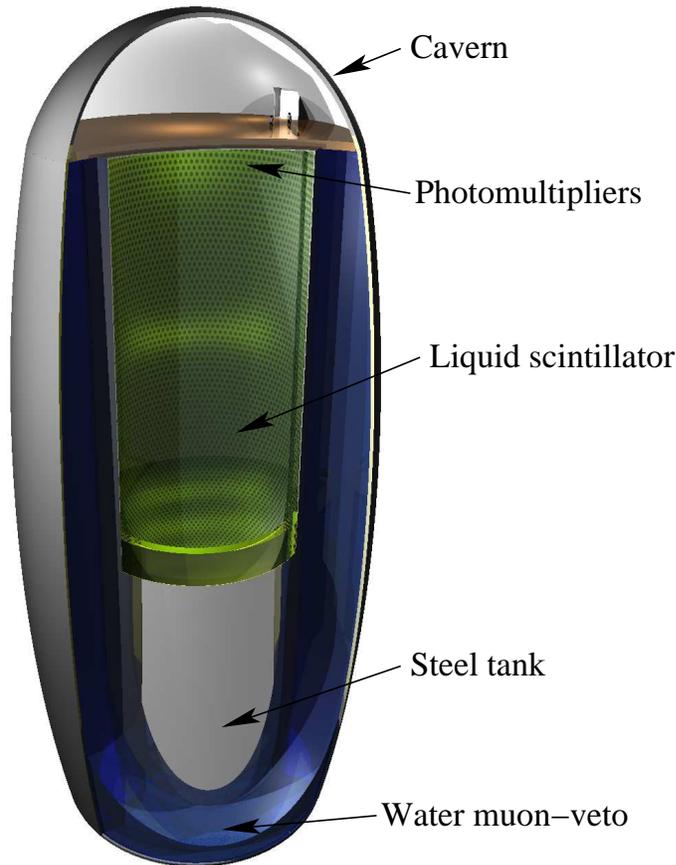
Figure 3.1: Artistic representation of the current LENA detector design. The cavern has an egg-like shape for stability of the surrounding rock. Inside, the detector is divided into an outer water muon-veto (in blue) and an inner volume contained in a steel tank which is filled with liquid scintillator (in green/yellow).

composition is still under discussion. The solvents PXE, LAB and dodecan, and the solutes PPO, pTP, bisMSB, and PMP[2] are under investigation. Experiments concerning optical properties of this detection medium have been performed within this thesis and therefore, more information on the liquid scintillator design for LENA can be found in chapter 8. To detect the scintillation light, the steel tank has to be instrumented with photo-sensors. At this stage $\sim$13 000 photomultiplier tubes (PMTs) are necessary providing a surface coverage of about 30%. However, further photo-sensor developments may offer an alternative. As mentioned in 3.1.3, radioactive impurities could be on the PMTs surfaces. To avoid continuous signals in the PMTs due to intrinsic radioactivity, the volume inside the tank is divided into two parts by a thin Nylon vessel. A similar approach has successfully been carried out in the Borexino experiment [89]. While the inner volume of with a radius of 12 m would contain the liquid-scintillator mixture, the outer volume could be filled with a non-scintillating oil with the same density and refractive index as the inner liquid.

Between the excavation hall and the steel tank, at least 2 m of water is foreseen. This water volume can act as Cherenkov detector to tag through-going cosmic muons: the muon veto. It could be instrumented with photo-sensors as well. However, the necessary coverage for this volume is much lower.

---

[2]The description of the scintillator components can be found in chapter 5

Chapter 4

Theoretical model of organic liquid scintillators

Scintillation materials or compounds are those which show the property of *luminescence*. When a luminescent material is excited (for example, by particle radiation, light, heat, chemical reactions), its deexcitation produces ultraviolet (UV) or visible light. Depending on the time scale τ of the light emission after excitation, the process is called *fluorescence* (typically, $\tau \sim 10^{-9} - 10^{-8}$ s) or *phosphorescence* ($\tau \sim 10^{-6}$ s or more).

In particle physics, these materials are widely used as they allow the detection of charged particles. When a charged particle crosses a medium, it loses its energy mainly by electromagnetic interactions. Electrons of the medium instantaneously feel an intense electric field and molecules are either ionized or excited. In case of scintillating materials, part of the energy released in the deexcitation of such electrons is emitted in form of photons. The advantages of such materials as detectors are: the linear relation between light output and energy deposition, the fast response time, and the possibility to use pulse-shape discrimination to distinguish different types of particles.

This chapter is a brief summary of the properties of organic liquid scintillators and the underlying theory [90]. The aim is to describe the microscopic behavior of these materials in order to achieve a better understanding of the measurements which are presented in the next chapters.

4.1 Electronic structure of organic molecules

Organic scintillators consist of hydrocarbon molecules which contain benzene-ring structures. To form an organic molecule, the four available valence electrons of the carbon atom ($1s^2 2s^1 2p^3$) can form saturated hydrocarbon (CH_4), doubly- (C_2H_4) or triply-bonded (C_2H_2) molecules.

There are three important electronic configurations. In the first configuration, the four valence orbitals combine to produce four equivalent bonds orientated in space as a regular tetrahedron (called sp^3 *hybridization*). These so-called σ-bonds are quite strong and do not produce scintillation.

In the second configuration, one s- and two p-orbitals combine (sp^2 *hybridization*) to form three equivalent orbitals. This configuration is required for the formation of the hexagonal structure of the benzene (as shown in the left part of figure 4.1) and other aromatic hydrocarbons. The three hybrid orbitals are coplanar and are inclined
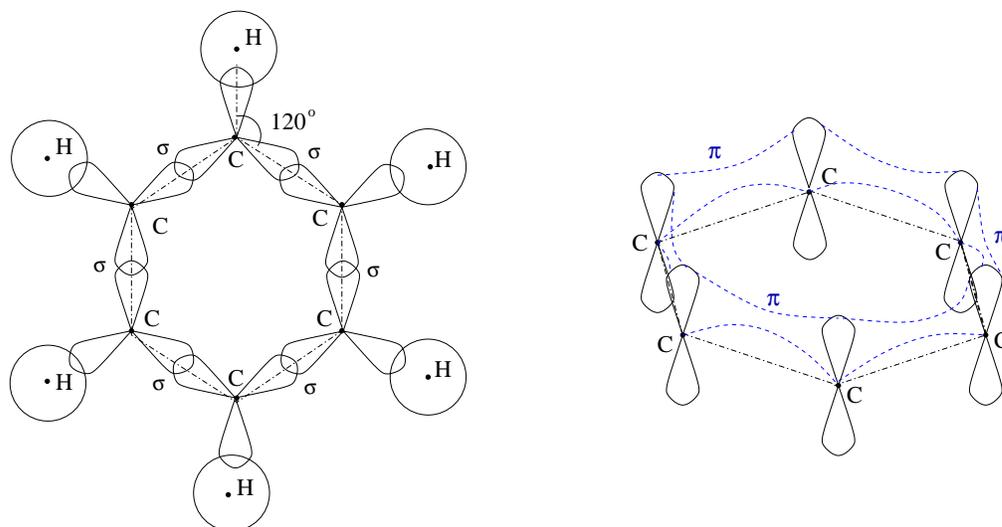
Figure 4.1: Orbital structure of the benzene rings. On the left, the three orbitals which produce σ-bonds are shown. On the right, the dotted lines illustrate the upper part of the symmetrical π-orbitals. The original p-orbitals from which the delocalized orbital derives are also represented.

at equal angles of 120° to each other. They produce σ-bonds which are strong bonds responsible for the rigidity of the molecular skeleton. These orbitals do not produce luminescence. The third p-orbital is symmetric with respect to the molecular plane and the associated electron is called π-electron. The π-electrons at each carbon atom interact among themselves to form symmetric orbitals with respect to a nodal plane in the plane of the σ-bonds. They are called π-bonds and are weaker than σ-bonds. In benzene, the six π-electrons form three double-bonds and combine to a single delocalized orbital (right part of figure 4.1). In organic molecules containing benzene, luminescence is caused by transitions from the excited states of these π-orbitals to the ground state.

In the third configuration, two of the p-orbitals combine to form π-orbitals. The triply bonded molecules result from the *sp hybridization* and are also luminescent.

4.2 Excited states of π-electron systems

A typical energy diagram for π-molecular orbitals, also called *Jabloski diagram* [91], is shown in figure 4.2. Depending on the relative spin orientation of the excited electron compared to the spin orientation of the unpaired electron in the ground state, parallel or anti-parallel relative spin orientations can be defined. As both configurations produce
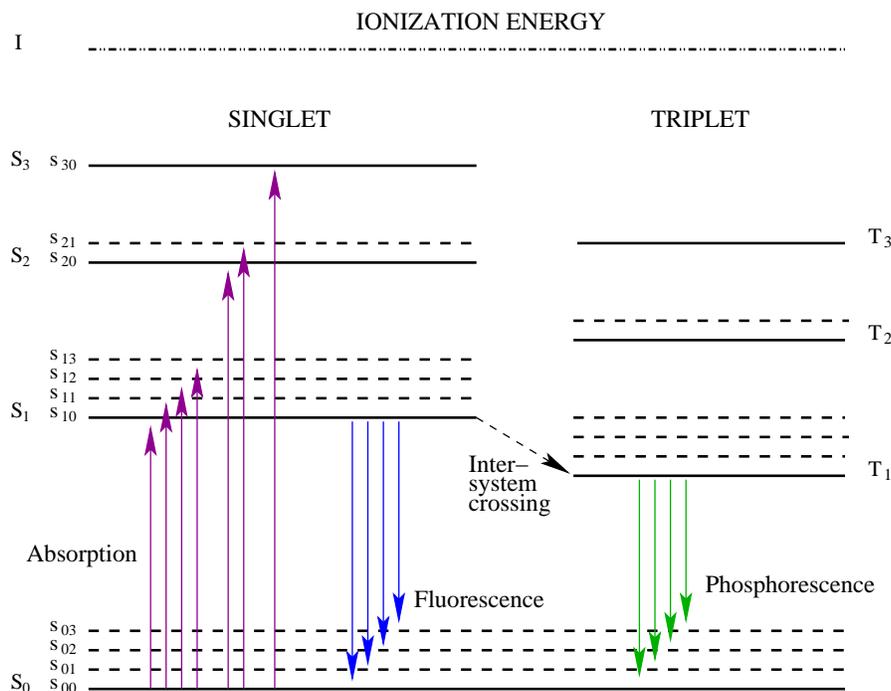
Figure 4.2: Energy levels of the π-electrons in an organic scintillator molecule. S_0 is the ground state; S_1, S_2 and S_3 excited singlet spin-states; T_1, T_2 and T_3 excited triplet spin-states; S_{00}, S_{01} ... vibrational sub-levels and I the ionization energy of the π-orbital.

different energy levels, the singlet and triplet spin states are shown separately in the diagram. The energy spacings between electronic levels (S_0, S_1 ...) are $2 - 4.5$ eV while between the vibrational levels of the molecule (S_{00}, S_{01}, S_{02} ...) it is about 0.1 eV.

When some excitation energy brings the molecule from the ground state, S_0, to some excited state S_i ($i \geq 1$), it rapidly (10^{-12} s) dissipates its energy through collisions with neighboring molecules until it reaches the S_1 level. Also excited vibrational states, S_{11}, S_{12} ... lose the energy quite fast (10^{-12} s) in the form of heat. This process is called *vibrational relaxation*. The relative intensities of the transitions from S_1 to different vibrational states of the ground state are given by the Franck-Condon factors [92][93]. These factors take into account the overlap of the vibrational wave functions. As shown in figure 4.2, in a fluorescence process the light is emitted through the transitions from

S_1 to S_0. Radiationless processes can occur between states of the same multiplicity, $S_1 \rightarrow S_0$, $S_2 \rightarrow S_1$ or $T_2 \rightarrow T_1$. Those processes are called *internal conversion* or *electronic relaxation* and cause losses concerning the conversion of excitation energy to fluorescence light.

Triplet states are usually populated indirectly as the absorption $S_0 \rightarrow T_1$ would mean an electronic transition with spin flip which is highly forbidden by selection rules. Ionized molecules recombine with electrons mainly into excited states, 75% of them triplet states [90]. A further possibility is the *inter-system crossing* process, that means the transition $S_1 \rightarrow T_1$ where the spin of an electron flips to the parallel configuration. When such triplet states are excited, there are several ways of emitting the energy in form of light. One possibility is to make the transition process T_1 to S_0 (phosphorescence), which is highly forbidden and therefore has a time scale of microseconds or longer. Usually the T_1 state produces indirect delayed-luminescence via $S_1 \rightarrow S_0$ as intermolecular interaction of T_1 can lead to excited singlet states. For example, during its lifetime T_1 can acquire per collision sufficient thermal energy to return to S_1. Furthermore, two interacting molecules in the T_1 state can deexcite by the reaction:

$$T_1 + T_1 \rightarrow S^* + S_0 \rightarrow S_0 + S_0 + photons, \tag{4.1}$$
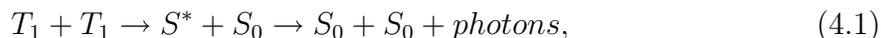
where two triplet states combine producing S_0 and one excited singlet state S^*. In both cases, fluorescence due to the S_1 to S_0 transition occurs but with a time delay compared to the direct emission. The delay accounts for the time which takes T_1 to acquire enough energy to go to S_1 or two T_1-excited molecules to meet and react.

4.3 Multi-component scintillators

The emission spectrum of a single-component scintillator has a significant overlap with its own absorption spectra. This results in multiple absorption and reemission processes where an important part of the information about the primary process is lost. To prevent additional losses in the energy conversion efficiency due to solvent self-absorption, a second (or even third) organic component is usually added. The aim of the second component, also called *wavelength-shifter* or *fluor*, is to efficiently absorb the light produced by the primary component, the solvent, and reemit it again in a longer wavelength region where the solvent is transparent. In this section, the main microscopic processes which take place in multi-component scintillation mechanisms are described. Detailed information can be found in [90][94]. The understanding of the scintillation process is important to make a proper interpretation of the results of the experiments in chapters 6 and 7 as well as to extrapolate these results to large liquid-scintillator detectors.

To discuss the two-component system, the solvent will be referred to as X and the solute as Y. In case of liquid scintillators, the concentration of Y is typically in the order

of a few grams per liter (g/ℓ) of X. In figure 4.3, the secondary processes which follow the excitation of the solvent are presented. Only singlet-spin states are displayed. Two of the solvent molecules are shown to explain interactions between them. The excitation of solvent and solute to one of their excited states is represented with a purple line. Red lines represent radiationless transitions and therefore energy losses. Blue lines are radiative transitions and black dashed lines represent energy transfer. The upper dashed lines show transfer by collision or by dipole-dipole interaction and the lower dashed lines represent radiative energy transfer. Finally, the dashed blue lines represent the photons which escape from the system and can be detected by photo-sensors. The probability of the different processes is shown as a rate (represented by k) in s^{-1} units. The direct excitation of the solute can be neglected as the concentration is usually very small.
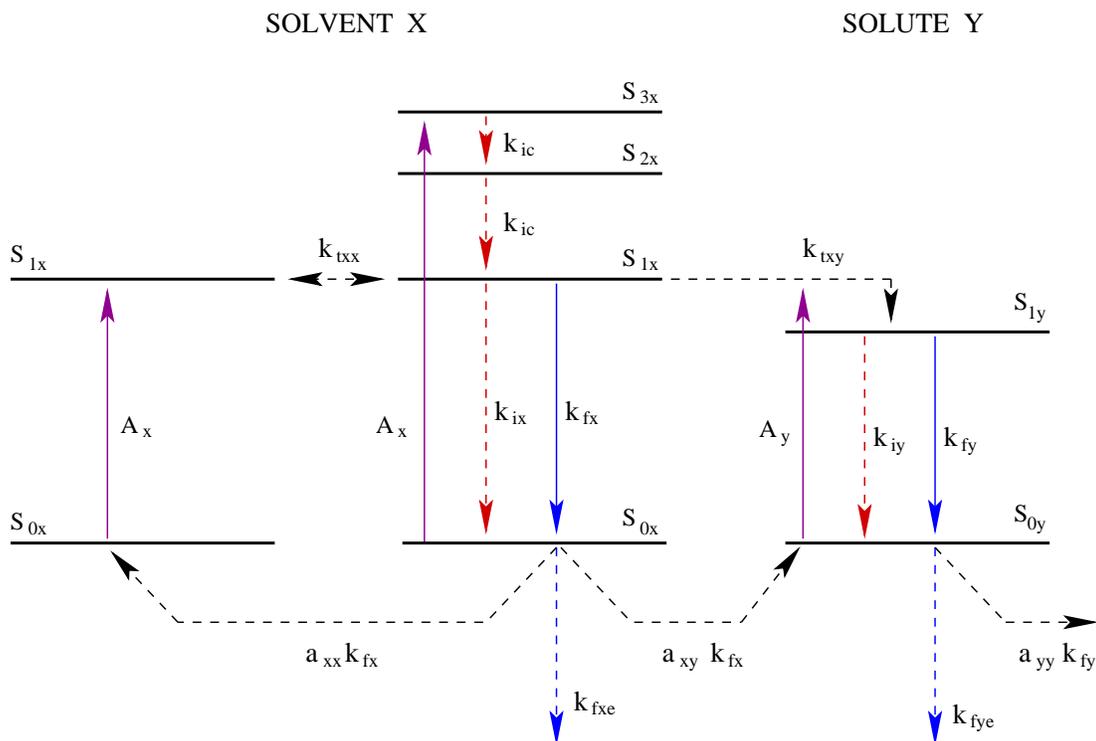
Figure 4.3: The scintillation process in a two-component system [90]. The solvent is denoted by X and the solute by Y. In this diagram, only singlet-spin states are shown. Purple lines represent the excitation of solvent and solute. Red lines represent radiationless transitions and therefore energy losses, blue lines are transitions with photon emission and black dashed lines represent energy transfer: the upper lines denote transfer by collision or dipole-dipole interactions and the lower ones by radiation transfer. The dashed blue lines represent the photons which escape from the system and can be detected by photo-sensors.

Charged particles which cross a scintillation medium ionize and excite molecules on their track. Although σ-bonds are quite strong, ionizing radiation can excite or ionize bonding electrons too. Ionization of these σ-electrons may result into a destroyed benzene molecule. Here, only excited π-electrons will be considered as they are mainly responsible for the scintillation. Except for the fraction of molecules which recombines, ionization leads to a loss of fluorescence efficiency. In general, energy-loss processes are commonly known as *quenching*.

When the solvent material is excited via A_x (see middle part of figure 4.3), the molecule rapidly decays nonradiatively to the state S_{1x} which causes internal quenching (k_{ic}). In the state S_{1x} four different processes compete: decay to S_{0x} without radiation (k_{ix}), decay to S_{0x} with fluorescence emission (k_{fx}), energy transfer per collisions to another solvent molecule (k_{txx}, also known as *energy hopping* [95]) or energy transfer to a solute molecule (k_{txy}). Since usually the lifetime of the solvent excited state (τ_{1x}: lifetime of the S_{1x} level) is chosen to be quite large (10-30 ns), energy transfer processes dominate [90][96]. The energy transfer from the solvent to solute molecules happens mainly nonradiative by dipole-dipole interaction [90]. The dipole-dipole transfer rate k for two molecules X and Y, located at a distance R apart from each other is given by [97]:

$$k = \frac{1}{\tau_{1x}} \left(\frac{R_0}{R}\right)^6 \tag{4.2}$$

where R_0 is the critical distance below which the probability for excitation transfer rapidly increases. R_0 is proportional to a term which takes into account the overlap between the solvent emission and the solute absorption. If fluorescence light is produced, there is a probability for this light to escape from the system ($k_{fxe} = (1 - a_{xx} - a_{xy})k_{fx}$) and to be detected. The photons also have a certain probability of being absorbed either by the solvent (a_{xx}) or by the solute (a_{xy}) molecules.

Once the state S_{1y} has been populated, the energy can propagate via radiative (k_{fy}) or radiationless (k_{iy}) processes from S_{1y} to S_{0y}. Most of the photons escape and are detected ($k_{fye} = (1 - a_{yy})k_{fy}$) but if the volume of the system or the concentration of the solute are large, there is still some probability that the light is reabsorbed by solute molecules Y ($a_{yy}k_{fy}$). The excitation of solute molecules may eventually lead to further losses of light due to other solute molecules. Reabsorption of a solute photon by another solute molecule may have a further radiationless transition k_{iy}. This is called *concentration quenching* and denoted by k_{cy} [90].

If a third component is added to the mixture, the wavelength can be shifted further to longer values and a similar scheme of energy transfer and absorption-reemission processes is obtained.

4.4 The light output

The light output parameter refers to the efficiency of converting deposited energy into emitted photons. This parameter is crucial as it determines the energy resolution and the threshold of the scintillator detector. The first part of this section describes the light emission in a phenomenological way. In the second part, the microscopic processes are taken into account.

The amount of light emitted by a scintillating material is not strictly proportional to the energy deposited by the ionizing particle. In reality, it is a complex function of the energy (not necessarily linear), the type of particle and the specific ionization [98]. In the previous section, quenching has been defined as the effect responsible for radiationless decay processes which imply light losses in the emission. In addition, excitation energy of several molecules can combine leading to additional ionized molecules. For example:

$$S^* + S^* \rightarrow S^+ + S_0 + e^- \tag{4.3}$$

where S^* stands for an excited molecule and S^+ for an ionized molecule. Ionization and excitation densities are high for large energy deposition per unit length $\frac{dE}{dx}$. This is the case for slow electrons or in general for heavier particles, as protons or α's. When the excitation density is high, the probability of the reaction 4.3 increases leading to a lower light yield.

For a phenomenological parametrization of the described energy deposition per unit length $\frac{dE}{dx}$ as a function of the ionization density, the semi-empirical Birk's formula [90] can be applied:

$$\frac{dL}{dx} = \frac{A\frac{dE}{dx}}{1 + kB\frac{dE}{dx}}, \tag{4.4}$$

where $\frac{dL}{dx}$ is the number of photons emitted per unit length. The parameters of this formula are: the absolute scintillation efficiency A (number of photons per energy unit) and kB, the parameters relating the density of ionization centers to $\frac{dE}{dx}$ [98]. These values are specific for every scintillator and have to be obtained from experimental data. In this formula, the ionization density is taken into account by the use of the Bethe-Bloch formula [98] which is introduced via the particle's energy loss per unit length $\frac{dE}{dx}$. Birk's formula correctly describes the light emission of several organic media.

Returning to the microscopic model, a general study of the light output can be performed without taking ionization density considerations into account. The number of photons N_y produced by the solute in a two-component scintillator can be written as [90]:

$$N_y = \frac{PC}{E_{1x}} \; f_{xy} \; q_{0y} \times 10^6 \tag{4.5}$$

33

where P is the fraction of the incident energy which leads to the excitation of π-electronic singlets. $C = E_{1x}/E_{ex}$ is the part of the excitation energy (E_{ex}) which contributes to fluorescence transitions (E_{1x}) or is transferred to the solute. f_{xy} is the fraction of the energy E_{1x} which is transferred from the solvent to the solute and q_{0y} is the fluorescence *quantum efficiency* of the solute Y, i.e. the fraction of the energy in S_{1y} which is released in the form of photons. According to the nomenclature of figure 4.3, f_{xy} and q_{0y} can be written as [90]:

$$f_{xy} = \frac{a_{xy}(c) \cdot k_{fx} + k_{txy}(c)}{k_{fx} + k_{ix} + k_{txy}(c)} \tag{4.6}$$

$$q_{0y} = \frac{k_{fy}}{k_{fy} + k_{iy} + k_{tcy}(c)} \tag{4.7}$$

where the dependence on the solute concentration c is written explicitly. Dedicated experiments around 1960 showed that the dependence of the nonradiative energy transfer on the concentration is linear [99][100]:

$$k_{txy} = m_{txy} \cdot c \tag{4.8}$$

$$k_{tcy} = m_{tcy} \cdot c \tag{4.9}$$

where m_{txy} and m_{tcy} are constants. The resulting dependence of the number of emitted photons on the concentration is given by:

$$N_y \propto \frac{a_{xy}(c) \cdot k_{fx} + m_{txy} \cdot c}{k_{fx} + k_{ix} + m_{txy} \cdot c} \frac{k_{fy}}{k_{fy} + k_{iy} + m_{tcy} \cdot c} \tag{4.10}$$

As explained before, the energy transfer from the solvent to the solute molecules takes place mainly via dipole-dipole interaction. As the lifetime of the solvent S_1 level is rather large (about $20 - 30\,\text{ns}$), the probability to have radiative transfer is negligible. For this reason, the approximation $a_{xy}[c] \rightarrow 0$ can be applied. The formula 4.10 can be simplified and the constant parameters reordered to:

$$N_y \propto \left(\frac{\frac{m_{txy}}{k_{fx}+k_{ix}} \cdot c}{1 + \frac{m_{txy}}{k_{fx}+k_{ix}} \cdot c} \right) \cdot \left(\frac{\frac{k_{fy}}{k_{fy}+k_{iy}}}{1 + \frac{m_{tcy}}{k_{fy}+k_{iy}} \cdot c} \right) \tag{4.11}$$

If constants are combined as following:

$$\frac{m_{txy}}{k_{fx} + k_{ix}} = A \tag{4.12}$$

$$\frac{k_{fy}}{k_{fy} + k_{iy}} = B \tag{4.13}$$

34

$$\frac{\mathrm{m}_{tcy}}{\mathrm{k}_{fy} + \mathrm{k}_{iy}} = D \tag{4.14}$$

this formula can be used to obtain the microscopic parameters (e.g., energy transfer efficiencies) of a composite scintillator by a measurement of the light emission in dependence on the solute concentration:

$$N_y \; \propto \; \left(\frac{A \cdot c}{1 + A \cdot c}\right) \cdot \left(\frac{B}{1 + D \cdot c}\right) \tag{4.15}$$

By a fit to the light yield as function of the solute concentration, the values of A, B and D result. This technique is therefore a common standard for the characterization of scintillator mixtures (e.g. [99][96]).

4.5 Fluorescence decay time

Time evolution of the light emission

In first approximation, the probability density function (PDF) of the photon emission process can be described by an exponential decay function which originates from the transition of the singlet state S_1 to S_0 (see figure 4.2).

$$n(t) = n_0 \; \exp\left(\frac{-t}{\tau}\right) \tag{4.16}$$

where n is the number of excited states at the time t, n_0 is the number of excited states at the time $t = 0$ and τ is the decay constant.

Commonly, scintillating materials show more than one decay constant due to the existence of further excited states, additional processes, or even non-exponential contributions. For this reason, a better description can be obtained by using the sum of several exponential functions:

$$n(t) = \sum_i n_i \; \cdot e^{-\frac{t}{\tau_i}}. \tag{4.17}$$

In this case, τ_i are the decay constants and n_i represents the value of the corresponding exponential function at the time $t = 0$. These constants are typical for each scintillator material. The first component usually has a large amplitude and corresponds to the transition $S_1 \rightarrow S_0$. One of the additional components is related to the triplet spin states (see for example equation 4.1). The time constant is determined by the transition probability from T_1 to S_1 [90].

The origin of the additional components usually found in measured data is not well understood. There are several processes -not necessarily exponential- which can account

35

for these contributions. Information on these processes can be found in the literature [90] and some of them are summarized in the following. A possibility is fluorescence due to a so-called *dimeric* state in which an ionized molecule binds to a non-ionized one producing new states. These dimeric states, usually denoted by D^*, possess specific energy levels which can produce fluorescence. Radiative absorption and reemission of light by the solute can also lead to a longer time constant. As it depends on the probability for self-absorption, it does not follow a simple exponential law. This effect has been investigated in chapter 7 and a contribution to the time decay is expected. Finally, electron recombination happens to form excited molecules and this could also result in a further contribution to the decay times. However, recombination times are slow in organic liquids [90].

Particle identification

The amplitudes of the time components described previously depend on the energy deposition per unit length $\frac{\mathrm{d}E}{\mathrm{d}x}$. For scintillators which have a strong dependence on the energy deposition, the pulse shape can be used for particle discrimination. In neutrino physics, these materials are commonly used for discrimination of α-particles or neutron-induced proton recoils from electron signals. As α-particles are a common background caused by natural radioactivity and a common detection reaction is the scattering of neutrinos on electrons (β-particle), this so-called α/β-discrimination is a fundamental method for background rejection.

For heavier or slower particles than fast electrons, the density of ionized and excited molecules is high. Therefore intermolecular interactions increase. For example, the presence of several nearby molecules with T_1-state electrons enlarge the amplitude of the corresponding delay-fluorescence component (see section 4.2). Figure 4.4 qualitatively displays the behavior of the pulse shape for three different types of particles: alphas, protons and electrons. It can be observed that the amplitude ratio between fast and slow components depends on the particle type.

In addition to the change in the pulse shape, high ionization densities lead to light losses (quenching). This effect can be understood by looking at equation 4.3. There excited molecules combine to produce an ionized molecule and one in the ground state. An ionized molecule is an effective loss of energy as the recombination time is long compared to the event duration. The probability for this process increases with the ionization density.

Lifetime measurements

Traditionally, in order to measure the fast time component of fluorescence, i.e. of the $S_1 \to S_0$ transition, excitation by ultraviolet light has been used [94]. By choosing the
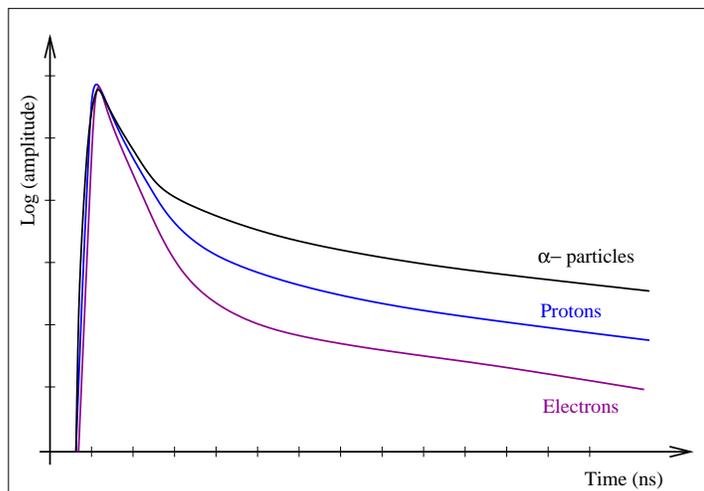
Figure 4.4: Comparison of the pulse shapes for alpha-particles, protons and electrons in a liquid scintillator. The amplitude of the pulses in logarithmic scale is plotted as a function of time.

energy of the excitation to fulfill the condition for resonance absorption $S_0 \rightarrow S_1$, the S_1 state can be overpopulated and the fast time constant can be measured separately, i.e. without being affected by other transitions. When the excitation of the medium is performed by particle radiation, all processes discussed in section 4.3 can contribute to the pulse shape. In chapter 6, measurements of the decay constants of several scintillator mixtures using radioactive sources will be introduced. The measured lifetimes correspond to the sum of the energy transfer times (processes k_{txx} and k_{txy}), the decay time (process k_{fy}) and additional contributions, for example from absorption-reemission processes ($a_{yy}k_{fy}$).

4.6   Light propagation

During the propagation of the produced photons through the medium, *absorption* and *scattering* processes can occur. These processes strongly depend on the emitted wavelength as in general the transparency of the medium increases with the wavelength.

Absorption describes processes in which photons interact with a component of the scintillator (an organic impurity for example) and their energy is released in heat. Such a process can in principle take place for both photons emitted by the solvent and photons emitted by the solute and implies always the loss of the photon. Scattering describes interactions in which a photon is produced in the final state and includes processes in which the direction of the photon and/or its wavelength is altered. There are two

37

main contributions to the scattering: Rayleigh processes involving the electrons of the different molecules present and Mie scattering by impurities. A description of these processes can be found in [101].

Moreover, the solute can absorb light produced by other solute molecules and reemit part of it again into a 4π solid angle. If the propagation of the light is considered for one direction, for example in the x direction, the intensity of the light can be written as:

$$I = I_0 \cdot e^{-\frac{x}{\lambda_a}} \cdot e^{-\frac{x}{\lambda_s}} \cdot e^{-\frac{x}{\lambda_{sa}}} \tag{4.18}$$

where I_0 is the initial intensity, λ_a is the absorption length, λ_s is the scattering length and λ_{sa} is the self-absorption length of the solute. For short wavelengths, the solute self-absorption dominates. For long wavelengths, absorption by organic impurities and scattering are the dominant processes. The total attenuation length λ for the propagation is given by:

$$\frac{1}{\lambda} = \frac{1}{\lambda_a} + \frac{1}{\lambda_s} + \frac{1}{\lambda_{sa}}. \tag{4.19}$$

For a large-volume particle detector, long absorption and scattering lengths are required. As absorption processes decrease the total number of photons which arrive at the photo-detectors, the effective light yield of the detector is reduced. As already mentioned, the light yield of a scintillator detector is a very important parameter as it accounts for the energy resolution and the energy threshold. Scattering and solute absorption-reemission processes lead to a loss of information on the position of the event in the detector. The photons have a different direction and this causes the arrival position (position in which the photomultiplier is hit) to be smeared out. In addition, it affects the timing structure of the events as scattered photons travel in general a longer distance leading to a longer propagation time. Measurements to the solute self-absorption have been performed within this thesis and are presented in chapter 7.

Chapter 5

Scintillator properties and sample preparation

To study some of the optical parameters of the scintillation process, laboratory experiments using several organic liquid samples have been performed (see chapters 6 and 7). These samples consist of a mixture of a liquid solvent and one or more solute powders, both scintillating organic compounds. In this chapter, the scintillating compounds used for the experiments and their properties are summarized. As the handling of organic liquid scintillators is not a trivial issue, the procedure to prepare a sample for a measurement is described in detail. Finally, some information on the materials used for the handling and for the scintillator container is outlined as material compatibility is required to avoid degradation of the liquid.

5.1   Properties of the scintillator components

This section is a compilation of properties of the organic substances used for the experimental investigations in the present work. In addition, information on the scintillator mixtures used in existing neutrino experiments is given.

Tables 5.1 to 5.4 summarize the main properties of the organic components of the scintillator: name, formula, absorption and emission wavelengths, CAS[1]-number and the name of the company which delivers them. The values given for the absorption and the emission wavelengths are peak values. The measured emission spectra for the different components are presented later in chapter 7 and the absorption spectra of several compounds can be found in [94]. First, table 5.1 compares two liquid solvents which have been investigated: *phenyl-o-xylylethan* (PXE from PXE Dixie [102]) and *linear-alkyl-benzene* (LAB from Petresa [103]). PXE has already been tested in the

---

[1]Chemical Abstracts Service: assignment of identifiers to every chemical.

Solvent	phenyl-o-xylylethan	linear-alkyl-benzene
Short name	PXE	LAB
Formula	$C_{16}H_{18}$	$C_9H_{12}+(CH_2)_m \quad m = 7-10$
Density	$0.986 \, kg/\ell$	$0.863 \, kg/\ell$
Absorption	$270 \, nm$	$260 \, nm$
Emission	$290 \, nm$	$283 \, nm$
CAS-number	6196-95-8	68890-99-3
Company	PXE Dixie [102]	Petresa [103]
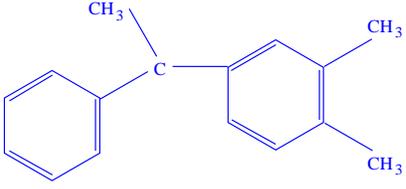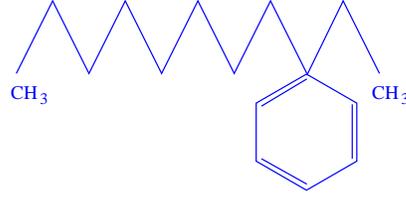
Table 5.1: Summary of the main properties of the solvents PXE and LAB.

counting test facility (CTF) [104] for Borexino and the results are very promising as it shows a high light yield, good transparency and it has a high flash point[2] [105]. LAB is a quite new scintillator solvent which, however, has been investigate by several groups [106][107][108] and is also very interesting due to its high transparency, high light yield, and low prize. The LAB type used for the measurements in this thesis is P550 Q. Both solvents, PXE and LAB, have the advantage of being a non-hazardous liquid with a flash point of 145° and 128°C, respectively.

Next in table 5.2, the properties of *dodecan* are presented. Dodecan is a mineral oil (carbon and hydrogen chain) which is added to the scintillating liquid first because of its high transparency and second because it increases the total number of free protons in the mixture which are the target of $\overline{\nu}_e$ (see chapter 2). The only disadvantage of using such an oil is that the light yield decreases as dodecan has no double or triple-bonds and therefore does not scintillate itself.

The emission and absorption spectra of the scintillating solvents have a significant overlap. To shift the wavelength to a region where the solvent is transparent, a further organic compound is commonly added. These additional solutes are called *wavelength-shifter* or *fluor*. In table 5.3, the properties of two so-called primary solutes are summarized: *2,5-diphenyl-oxazole* (PPO) and *para-terphenyl* (pTP). Both of these compounds absorb approximately where the solvents PXE and LAB emit and have a *Stokes shift*[3]

---

[2]The flash point is the lowest temperature at which a liquid generate sufficient vapor to form a flamable mixture with oxygen.

[3]Phenomenon which takes its name from Stokes who found in 1852 that emitted light in scintillators was composed of wavelengths longer than those of the absorbed light.
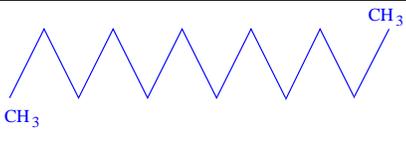
Solvent	dodecan
Formula	$C_{12}H_{26}$
Density	$0.749\,kg/\ell$
CAS-number	112-40-3
Company	Sigma-Aldrich [109]

Table 5.2: Properties of the non-scintillating solvent oil dodecan.

Solute	2,5-diphenyl-oxazole	para-terphenyl
Short name	PPO	pTP
Formula	$C_{15}H_{11}NO$	$C_{18}H_{14}$
Absorption	$303\,nm$	$275\,nm$
Emission	$365\,nm$	$339\,nm$
CAS-number	92-71-7	92-94-4
Company	Sigma-Aldrich [109]	Sigma-Aldrich [109]
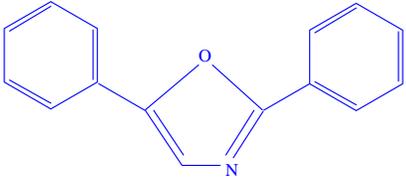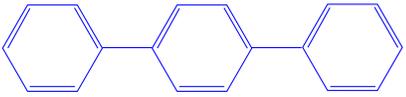
Table 5.3: Properties of the primary fluors PPO and pTP.

of $\sim$60 nm. PPO[4] has been widely used and its properties are well known [99]. In table 5.4, further solutes are described: *1,4-bis-(o-methyl-styryl)-benzene* (bis-MSB) and *1-phenyl-3-mesityl-2-pyrazoline* (PMP). BisMSB is a secondary wavelength-shifter as it is usually added in addition to a primary shifter. It absorbs where the primary fluor emits and produces a further shift of $\sim$ 60 nm. It is added in small quantities to avoid self-absorption at large wavelengths. PMP [110] is a primary solute with a large Stokes shift of about 120 nm. It has the advantage that absorption and emission spectra overlap only marginally and hence, its self-absorption is small.

All solutes used are in powder form and were dissolved in the liquid solvent. The goal is to find a scintillator mixture which shifts the wavelength to the range $\lambda > 400\,nm$

---

[4]This solute which is recognized today as an efficient solute in scintillator solutions, was first synthesized in 1896 by Emil Fisher [99].

Solute	1,4-bis-(o-methylstyryl) -benzene	1-phenyl-3-mesityl -2-pyrazoline
Short name	bisMSB	PMP
Formula	$C_{24}H_{22}$	$C_{18}H_{20}N_2$
Absorption	345 nm	294 nm
Emission	420 nm	415 nm
CAS-number	13280-61-0	60078-97-9
Company	Sigma Aldrich [109]	Merck [111]
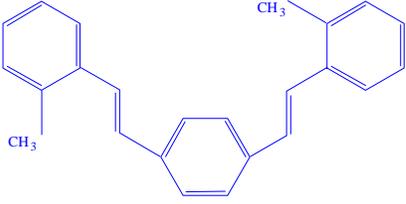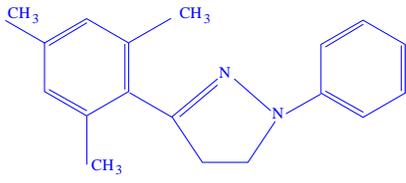
Table 5.4: Properties of the secondary fluor bisMSB and a fluor with large Stokes shift PMP.

to guarantee large absorption and scattering lengths (see chapter 4). In addition, this is the region where the photomultipliers are most sensitive. Therefore, by choosing a large emission wavelength, the total detection efficiency increases. This can be reached by combining two common wavelength-shifters (primary plus secondary) or by the use of a solute with a large Stokes shift.

As already mentioned in chapter 1, several organic liquid-scintillator experiments have delivered important physics results, especially in the neutrino astronomy field. KamLAND [112] uses a composition of 20% *pseudo-cumene* (PC), 80% dodecan and $1.5 \, \mathrm{g}/\ell$ PPO, CHOOZ [113] involved 50% paraffine and 50% hexanol loaded with 0.09% gadolinium, $1 \, \mathrm{g}/\ell$ pTP and bisMSB, KARMEN [114] used 25% PC, 75% paraffine and $2 \, \mathrm{g}/\ell$ PMP, and Borexino [89] has a PC solvent with $1.5 \, \mathrm{g}/\ell$ PPO.

5.2 Mixture-preparation procedure

Liquid-scintillator samples are prepared and stored in glass bottles as glass is compatible with liquid scintillator. Before closing the bottles tightly, the liquid is bubbled with nitrogen gas. All air in the bottle is replaced by nitrogen to avoid reactions of oxygen with the scintillator. Oxidation of the organic liquid may lead to a degradation and thus, the light emission might decrease. The liquid solvent and the solute powder are weighed in two different balances. The first is used for the solvent and permits a maximum weight of 1 200 g with a precision of 10 mg, while the second, for the small powder quantities,

has a maximum weight of 100 g with a precision of 0.1 mg. Afterwards, both components are mixed together. Usually, the solute can be dissolved easily by bubbling nitrogen gas through the liquid. In the case of pTP and for high concentrations of bisMSB ($c \sim 1\,g/\ell$), due to their low solubility, heating of the samples was required to achieve the dissolution (1-2 hours at $\sim 70°$C). This difficulty to dissolve pTP makes such a liquid scintillator less feasible for a large-volume detector.

Once the mixture is ready, the scintillator container for the experiment has to be filled carefully. A description of the container is given in section 5.3. First of all, the constituent pieces of the container have to be cleaned: first with water and soap and then carefully with propanol. Later, the pieces are assembled and the inside volume of the container is bubbled with nitrogen. The scintillator is handled with an injection needle made of glass. A first scintillator filling is always performed for cleaning. After a second filling with the desired mixture the container is bubbled again with nitrogen to avoid oxygen contamination in the liquid. Immediately thereafter, the container is filled completely and closed tightly. The whole procedure is carried out under a flow-box to avoid dust deposition.

5.3   Sample container and material compatibilities

Liquid scintillators can be quite aggressive versus plastic materials and for this reason all components of the scintillator container have to be known to be compatible, otherwise a test has to be performed. The container for the experiment was made out of black PTFE[5] material as PTFE is known to be compatible with the liquid scintillators used in this work.

The design of the container is shown schematically in figure 5.1. It has a cylindrical shape with an inner diameter of 2.5 cm. The length of the container is 2.0 cm for the fluorescence measurements (chapter 6) and 1.0 cm for the spectroscopic experiments (chapter 7). The container was chosen slightly smaller for the spectroscopic measurement to investigate the effect of light propagation with small distances. On both sides of the cylinder, 2 mm thick quartz windows are placed to allow light to escape and reach the photomultipliers. Quartz was chosen as it has a homogeneous transmission for wavelengths down to approximately 150 nm.

The container is held together by 8 screws. To keep the container tight O-rings are placed beside the quartz in a groove on the PTFE cylinder. Originally, the O-rings were made of Viton. After few days it was realized that the material reacts with the scintillator and changes its shape. The O-rings were replaced by Teflon-coated ones. For the filling, there is an opening on the top. After filling, it is closed with a screw. To close it tightly, a Teflon ring is placed between the screw and the container.

---

[5]Teflon-PTFE is a synthetic fluoropolymer.
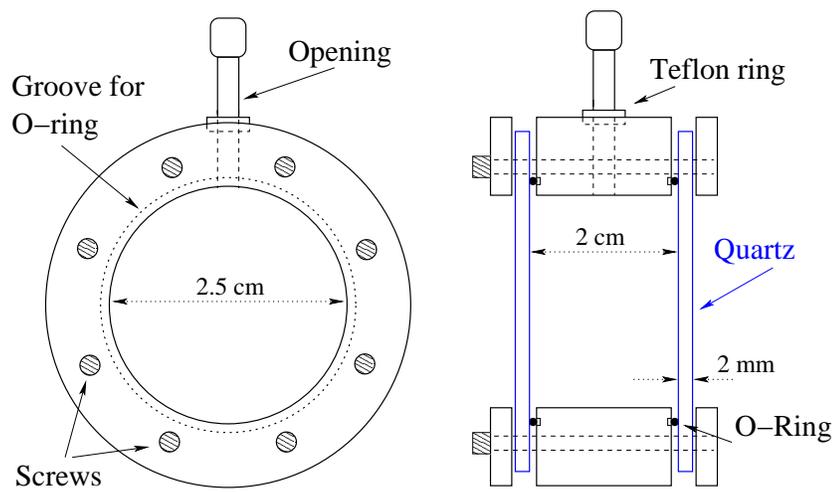
Figure 5.1: Schematic of the scintillator container geometry: top and side view.

Chapter 6

Fluorescence decay-time measurements of organic liquids

The lifetimes of the molecular excited states in a scintillator determine the pulse shape of the events in a detector application. For this reason, experiments relying on pulse shape analysis for background discrimination are always dependent on the fluorescence decay-time constants. This is the case for α/β-discrimination in the detection of solar neutrinos [22] or for the search for proton decay via $p \to K^+\overline{\nu}$ (see chapter 9). In the future LENA project [36], the search for proton decay is one of the main goals and thus the determination of the signal's pulse shape is of great interest. Therefore a dedicated experiment to determine fluorescence decay constants of several scintillator mixtures has been performed in the course of this thesis. After a description of the setup and the electronics, the offline analysis of the data and the results are presented. The measurements were performed at the TU-München (Garching) from December 2006 to April 2008.

6.1   Experimental method

The goal of the experiment is to determine the *probability density function* (PDF) which describes the time-dependence of the photon emission in the fluorescence processes of organic liquid scintillators. A sampling of the emission time of photons after excitation of the medium is therefore required. Details concerning organic scintillator PDF will be given in section 6.5.3. The experiment uses the *start-stop* method [115] which measures the arrival times of single photons. In this method, the start-signal accounts for the starting-point of the pulse: approximately the time of the energy deposition. If a light detector is able to measure a large number of photons of an event, the start time can be extracted from the first detected photon. A second detector provides the stop-

signal. Therefore, this detector should be designed in such a way that the probability of detecting a single photon of an event is in the few % regime. This guarantees that the probability to detect more than one photon in an event is almost zero. The PDF of a certain scintillator mixture results from the time difference between the start and the stop signals (see section 6.6).

6.2 Experimental setup

In this section, the experimental realization of the single-photon counting method is described. The main constituents of the setup, the electronic design and the data acquisition system are presented.

6.2.1 Setup and commissioning

The main setup consists of a liquid-scintillator sample and two photomultipliers (PMTs) which detect the emitted light. The sample is irradiated by a ^{54}Mn gamma-source (834 keV). The left part of figure 6.1 shows a scheme of the layout while a photograph of the setup can be seen on the right. The scintillator sample is filled into a cylindrical container made of black Teflon with quartz windows at both ends (see chapter 5). It contains only about 10 ml of liquid to guarantee a single Compton interaction of the ^{54}Mn gamma-rays. The maximum energy for the recoil electron for this source is 639 keV (back-scattering, i.e. Compton-edge energy). Compton electrons deposit their energy in the scintillator leading to light emission. One of the PMTs is directly coupled to the scintillator container (close PMT) by using silicone oil. It detects a large number of photons per event and thereby setting the starting-point for the event. The second PMT is placed ~ 30 cm away from the sample (far PMT). This distance was chosen to assure single-photon counting due to the small solid angle. The probability to detect a photon from a Compton event in the designed setup is at most 3%. This value has been calculated conservatively assuming 10 000 photons/MeV light emission and an energy deposition corresponding to the Compton edge of ^{54}Mn.

The PMTs used for the experiment are type 9111 from the company Electron Tubes [116]. The cathode is 25 mm ($1''$) in diameter with a plane-concave window. Table 6.1 summarizes the main technical specifications of these PMTs provided by the manufacturer. The PMTs marked with (1) were used during the time period December 2006 to April 2007, those marked with (2) during April 2007 to April 2008. The original PMTs (1) were replaced in April 2007 to have a UV-light transmitting window. Both types of PMT-windows have a maximum sensitivity of $\sim 30\%$ at 350 nm. While the borosilicate window used in (1) transmits less than 10% below 300 nm, the UV-window used in (2) transmits more than 10% already above 230 nm. In addition, the new PMTs
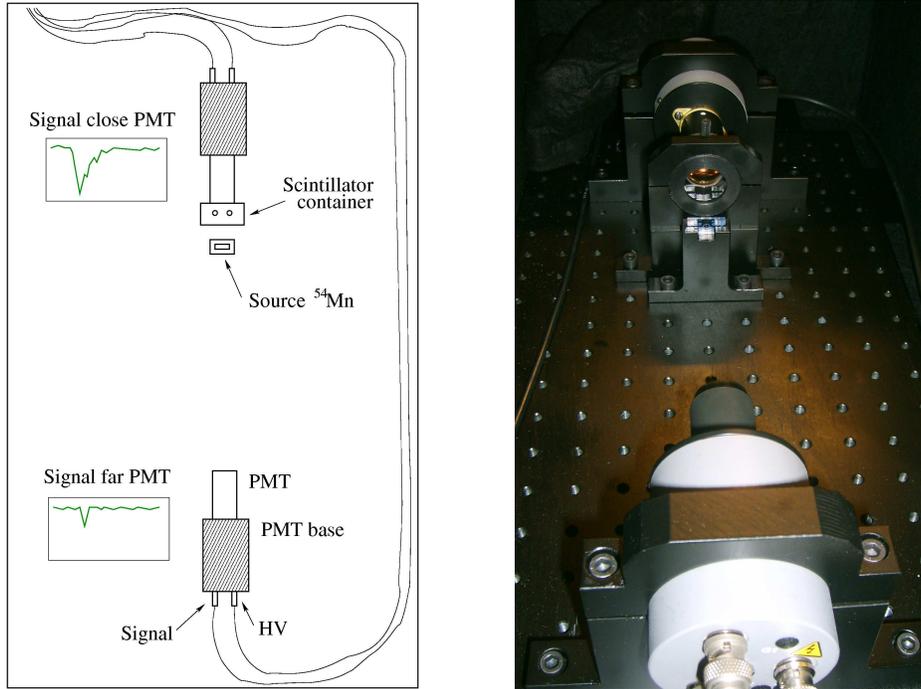
Figure 6.1: Left: Schematic diagram of the setup for the fluorescence-time measurement. Two photomultipliers collect the scintillation light emitted by a scintillator mixture, one is coupled to the container and the second is located at 30 cm distance. The scintillator is excited by a ^{54}Mn γ-source. Right: picture of the setup mounted on an optical bench.

were selected for low dark current. Both sets of PMTs performed properly. The working HV was chosen to allow for a high detection efficiency at low dark current. The photo-tubes were operated at 756 V, 750 V (1) and 768 V, 978 V (2) for the close and far PMTs, respectively. The single-photon response of both PMTs which were used as far-detector can be seen in figure 6.2. The plot shows a histogram of the pulse height. It is fitted with the sum of a Gaussian curve (for the single-photon peak) and an exponential function which describes thermal noise. The latter arises mainly from the noise of the dynode-chain used for signal amplification inside the PMT:

$$F(x) = a \cdot e^{-\frac{x}{\tau}} + h \cdot e^{-\frac{(x-r)^2}{2 \cdot \sigma^2}} \tag{6.1}$$

x is the pulse height, a and h are the amplitudes of the exponential and the Gaussian curves, respectively, τ is the time constant in the exponential, r and σ are the position of the center and the width of the Gaussian curve. The peak at the right end of each histogram corresponds to events with an overflow in pulse height as the maximum range of the data acquisition was set to 0.5 V.

47

	Close PMT (1)	Far PMT (1)
Type	Electron tubes 9111B	Electron tubes 9111B
Serial number	20 918	20 934
Time jitter σ	0.98 ns	0.98 ns
Window	borosilicate glass	borosilicate glass
	Close PMT (2)	Far PMT (2)
Type	Electron tubes 9111WA	Electron tubes 9111WA
Serial number	175	201
Time jitter σ	0.98 ns	0.98 ns
Dark current	$108\,\mathrm{s}^{-1}$	$70\,\mathrm{s}^{-1}$
Peak/valley ratio	1.54	1.80
Window	UV-glass	UV-glass

Table 6.1: Summary of the technical specifications (as given by the provider) of the photomultipliers used for the experiment. For the PMTs (1), the dark current and the peak-to-valley ratio were not specified.

The whole setup is located inside a black-box which has carefully been tested for light tightness. The holders for the different modules and the scintillator container were chosen in black color to avoid light reflections which may have an influence on the PDF. External electromagnetic fields were the main background noise for the measurements during the first months as it induced coincident signals in both PMTs. Several improvements were applied to solve the problem. The main improvement resulted from a protective μ-metal shielding around the PMT tubes. Moreover, lead sheets around the box shield the experimenter from the radioactive source and at the same time shield the experiment from electromagnetic noise. Additional aluminum panels have been placed on top and bottom of the black-box for the same reason. The remaining noise pulses were removed later by software analysis (see section 6.5).

6.2.2   Electronics and data acquisition

A NIM[1]-based electronic setup has been used for the signal processing. First, the signals of both photomultipliers are amplified by a factor of ~ 10. The amplifier module has a splitter which delivers two analog output signals. One is used directly to connect the output of each PMT to the data acquisition system. For the amplified close-PMT signal, the second output signal is connected to a discriminator and used as trigger for the data acquisition system. The trigger threshold is set to 70 mV by the discriminator.

---

[1]Nuclear Instrument Module, standard mechanical and electrical specifications.

9111B 20934	
Entries	150000
a	1597 ± 147.9
τ	0.03748 ± 0.00258
h	600.6 ± 4.5
σ	0.09573 ± 0.00070
r	0.1833 ± 0.0014

9111WA 201	
Entries	150000
a	2000 ± 0.7
τ	0.01843 ± 0.00041
h	506.3 ± 1.7
σ	0.1305 ± 0.0007
r	0.2003 ± 0.0008
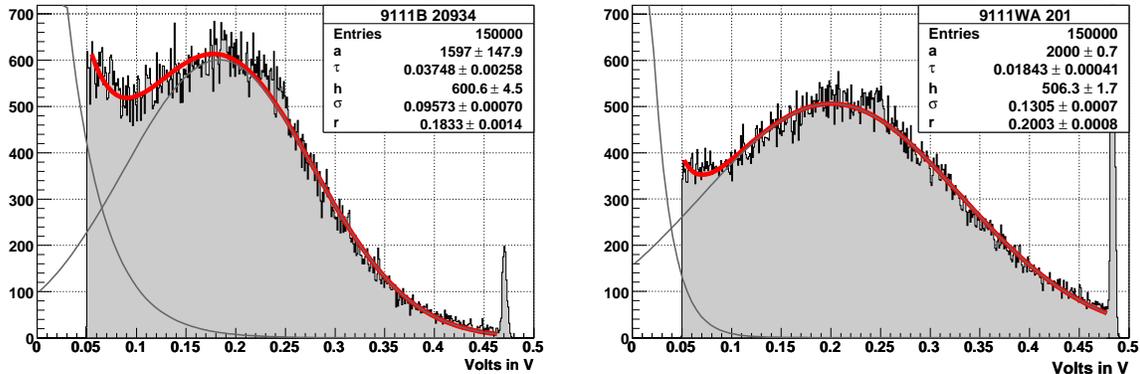
Figure 6.2: Single-photon pulse-height spectra for the far detectors: electron-tubes 9111B 20 934 (left) and electron-tubes 9111WA 201 (right). The data is fitted according to equation 6.1. For further details see text.

For data readout and recording, an Acqiris (Acqiris/Agilent Technologies [117]) data acquisition system is used. The device has four inputs for signal channels plus one input for an external trigger. In the setup, the acquisition system is operated at a sampling rate of 4 GS/s (giga-samples per second) which is the maximum possible together with a 10 bit dynamic range. The system is operated with this external trigger given by the close-PMT. A Labview (National Instruments [118])-based software is used as software trigger and to store the data. When a trigger signal from the close multiplier appears, a coincidence window of 500 ns is opened. If the software detects a signal above threshold (0.05 V) in the far-PMT, both photomultiplier data are stored in a separate text file. The signal is sampled every 0.25 ns. The resulting files have a size of ~ 1 GB each and contain 50 000 pulses covering a measuring time of ~ 8 h.

6.3   Background sources

Several sources of background have been identified in the experiment. The first has already been mentioned in 6.2.1: electromagnetic fields can produce coincident noise signals in both PMTs. However, with the implemented shielding, this background has been suppressed almost completely. Remaining noise pulses are later removed by the software analysis. In addition, the dark-current pulses of the PMTs as well as pre- and after-pulses can affect the measurement. In the following sections, these effects are described in detail and the solutions to remove such noise pulses are given specifically for each PMT.

49

6.3.1 Random coincidences due to dark current

The dark current of a photomultiplier refers to thermally produced electrons in the cathode or in the dynode-chain [98]. Electrons emitted by the cathode have a single-photon structure in the spectrum as they experience the complete amplification through the dynode-chain. The shape of the spectrum due to the electrons produced in the dynodes is an exponential function because it is a superposition of electron signals generated in the different amplification stages.

The dark current of the close PMT does not significantly contribute to the background of the measurement. This is because the threshold of this detector is set much higher than the single-photon peak as the close PMT is supposed to see a large amount of photons.

In the far PMT, however, such pulses can fake the signal of a fluorescence event. To reduce this background, PMTs selected for low dark current were chosen. The measured dark rates R_S of the far PMTs at the working voltage are (1) $R_S = 20.0\,\mathrm{s}^{-1}$ and (2) $R_S = 19.5\,\mathrm{s}^{-1}$. To calculate the random coincidence rate, the mentioned dark current values as well as the length of the coincidence time gate and the close PMT trigger rate are needed. The latter depends on the light yield of the specific sample. A typical value of the trigger rate is $R_T = 100\,\mathrm{s}^{-1}$. The random coincidence rate R_c can be written as:

$$R_c = R_T \cdot R_S \cdot t_w \tag{6.2}$$

where t_w is the coincidence time window of 500 ns. By multiplying the rate R_c with the typical measuring time of $t_m = 8\,\mathrm{hours}$ (for a measurement of 50 000 pulses), the number of random coincidences $N_c(8\,\mathrm{h}) \simeq 29$ results. This implies a relative number of background events of 0.06% which is a negligible contribution.

As the dark-current rate is temperature dependent, the laboratory was kept at an almost constant temperature which was measured before every measurement. A maximum oscillation $(19 - 23)°\mathrm{C}$ for the whole measuring period has been found. The dark-current rate R_S was however stable over the measuring time.

6.3.2 Pre- and after-pulses

Pre-pulses correspond to signals produced by photoelectrons which are not properly focus on the first dynode but arrive at a later one leading to a shorter transition time. These pulses have one or more multiplication stages less than electrons arriving at the first dynode and for this reason the pulse height is, in general, smaller. As the determination of the starting-point in the close PMT is performed by a constant-fraction method (see section 6.5.1), a small pre-pulse before the considered main pulse does not disturb as the trigger is always above single photons in the close PMT. In the far PMT,

pre-pulses which are above the threshold can not be distinguished from single-photon pulses.

After-pulses are produced when a photoelectron ionizes residual gas inside the tube and a positive ion accelerates back to the cathode or to a previous dynode. The impact of the ion can release further electrons which drift again to the dynode-chain producing a delayed pulse. The height of the after-pulse depends on the position of the ion production (it is smaller when it is produced at a dynode) and on the number of electrons that it releases when it collides with the cathode or a dynode.
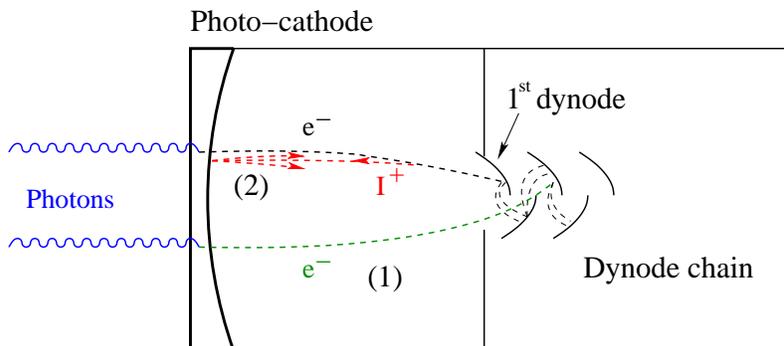
Figure 6.3: Diagram of a photomultiplier where pre- (1) and after-pulses (2) are shown.

In the close PMT, after-pulses have no relevance for the measurement as after-pulses are hidden inside the many-photons pulse. In the case of the far PMT which detects the single photons, after-pulses have to be removed from the data by software as they are indistinguishable from events where two single photons appear (see section 6.5.1). The after-pulse rate for the PMTs used for the experiment is specified by the provider at about 5% in $0.1\,\mu$s which means that 5% of all pulses have after-pulses within a time window of $0.1\,\mu$s after the main pulse. These after-pulses might be either smaller or larger than the single-photon pulse itself due to the different ways such pulses are produced.

6.3.3 Early and late-pulses

The cathode of a PMT is semi-transparent allowing only few photons to cross without producing a photoelectron. In this case, the photon can reach the first dynode and produce the photoelectron there. As a result, the propagation time of the photoelectron is shorter and early pulses appear. Moreover, sometimes the electron produced in the photo-cathode does not produce a cascade at the first dynode but scatters and goes back to the cathode. In this process, the electron loses its energy as it is moving in a trajectory

against the electric acceleration potential. After it has stopped, it is accelerated again towards the first dynode. The result of this effect is a late arrival time of the signal.
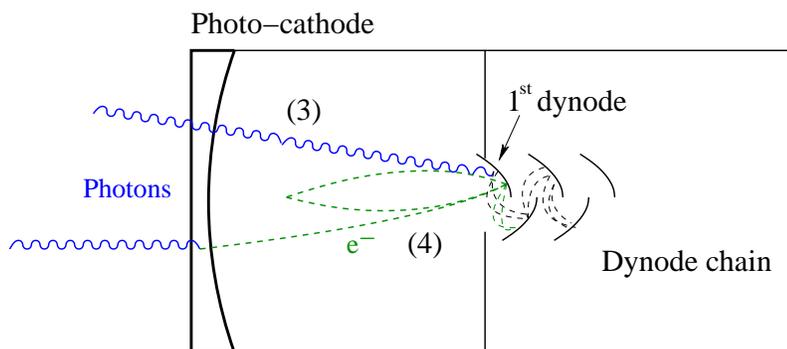
Figure 6.4: Diagram of a photomultiplier where early (3) and late pulses (4) are shown.

Both early and late-pulses affect the measurement of the single photon in the far-PMT. These effects have been observed within this work (see section 6.5.2) and their contribution accounts to a few %.

6.4   Measurement of the time resolution

The time-resolution function of the fluorescence-measurement system depends mostly upon the single-photoelectron transit *time jitter* of the PMT. Photoelectrons produced at different positions of the cathode have different propagation distances to the first dynode. This results in a smearing of the transit time through the tube. As shown in table 6.1, the time jitter of the PMTs used is $0.98\,\text{ns}^2$. An additional source of loss in time-resolution is the time jitter of the electronic readout chain, however being usually a smaller contribution.

6.4.1   Experimental setup

To measure the time resolution of the whole system, an additional experiment has been performed. The idea is to evaluate the resolution of the measuring system when the far PMT detects a signal which is simultaneous with a Compton event. This is carried out by the use of a Cherenkov radiator (Plexiglas) in front of the far PMT. The scintillator sample is coupled as usual to the close PMT while a Plexiglas (acrylic glass) disk of

---

[2]The specified value is the full width at half maximum (FWHM) of $1.2\,\text{ns}$ which corresponds to $\sigma = 0.98\,\text{ns}$.

2 cm thickness is mounted in front of the far PMT. The far PMT is optically decoupled from the sample by the use of a black plane that guarantees optical shielding. The ^{54}Mn source is replaced by a ^{22}Na source that emits two coincident gamma-rays of 511 keV energy in opposite directions (from $e^{+}e^{-}$ annihilation). Figure 6.5 shows the experimental arrangement for this measurement. As the source is placed between both
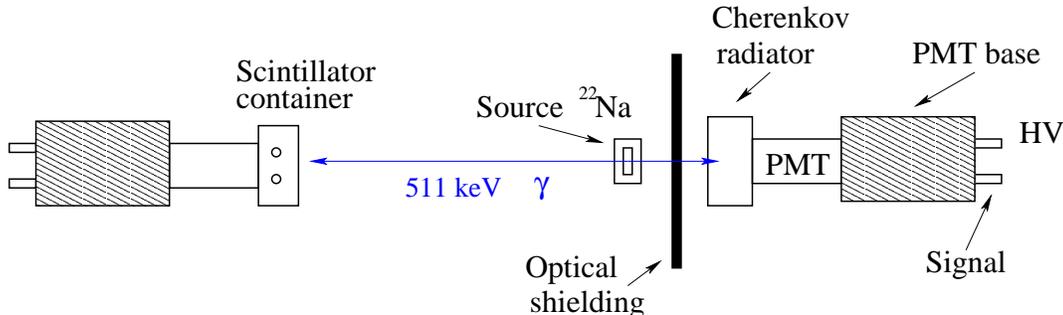
Figure 6.5: Arrangement to measure the system's time resolution.

PMTs, coincident 511 keV γ-ray Compton interactions in the scintillator and in the Plexiglas can occur. In the scintillator, the Compton electron is responsible for the scintillator signal. The Compton electron produced in the Plexiglas (with a refractive index of $n = 1.49$) has a maximum energy of 341 keV which is above the Cherenkov threshold for this medium. As the Cherenkov light-emission is a rapid process, the arrival of the photons is expected few picoseconds after the propagation of the Compton electron in the Plexiglas material. The amount of Cherenkov photons produced by a certain energy is much lower than the corresponding scintillation signal. In order to increase the rate of the detected Cherenkov pulses, the radioactive source was placed closer to the Cherenkov radiator than to the scintillator. The new position of the radioactive source produces a constant shift of the time differences. The source has been moved about 30 cm resulting in about 1 ns shift. However, this effect doesn't influence the measurement as the width and shape of the distribution are the interesting parameters and not the global position of the distribution. This method has already been used [119] to determine the time resolution for such experiments and provides the distribution of simultaneously produced events in the system.

The electronic configuration as well as the data acquisition settings remain the same as described in 6.2.1 except for the coincidence window which is reduced from 500 to 125 ns (see section 6.2.2). The analysis software used is the same as in the decay-times measurements except by the close-PMT threshold which was increased to 0.15 V. The reason is to increase the mean energy of the Compton-scattered photon in the scintillator as the 511 keV gamma from ^{22}Na is lower than ^{54}Mn energy (834 keV). By increasing the low-energy threshold in the software analysis, the spectra of both sources are more

similar and the time-resolution determination is more realistic.

6.4.2   Results

Figure 6.6 shows the distribution of the time differences between the starting-point given by the scintillation signal and the arrival of the Cherenkov photons. The number of
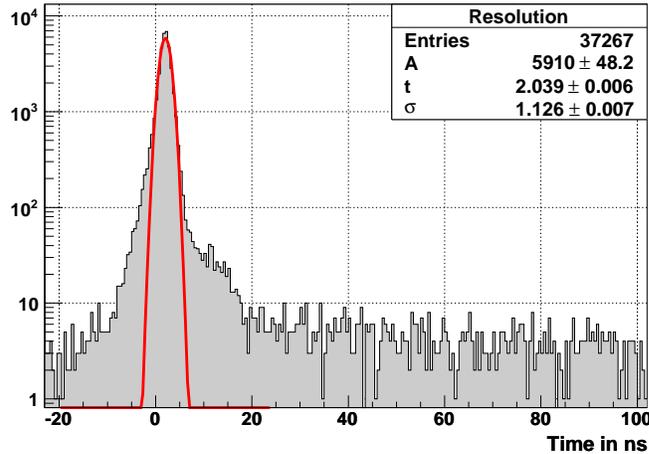
Figure 6.6: Distribution of the time differences between the starting-point signal in the scintillator and the arrival of Cherenkov photons. A Gaussian curve nicely describes the time resolution of the system (the events are plotted in logarithmic scale).

events (y-axis) is represented in a logarithmic scale to better exhibit the surrounding events of the main peak. The main part of the pulses can be described by a narrow Gaussian curve, with a $\sigma = 1.13 \pm 0.07$ ns. As mentioned before, the time-jitter of the PMTs is 0.98 ns. This measurement shows that the rest of the electronics worsens the resolution only slightly. The start-stop method relies on the assumption that the start-time is given by a pulse with a large number of photons (see section 6.1). Consequently, the resolution of the measuring system gets better for large pulse height in the close PMT. In section 6.6, the resolution of the system for different scintillator samples is presented.

Although the main peak is well described by a Gaussian function, there are small contributions at the left and at the right sides of the main peak. The shoulder on the left side is due to pre-pulses of the single-photon tube. Further away on the left, there is a contribution which can be explained as photons which cross the cathode and produce a photoelectron directly in the dynode-chain, the early pulses. The contribution of the whole left part of the Gaussian peak is about 5%. The description of these effects can be found in section 6.3.

The pulses on the right ($t < 20$ ns, which is of the order of the PMT transit time of 15 ns) can be explained as reflexion of photoelectrons on the first dynode to the cathode i.e. scattering processes where the electron goes back towards the cathode. This effect makes about 2% of the pulses and has also been reported in [115]. The rest of the pulses at later times ($t > 20$ ns) contributes about 2% of the total number of pulses. Its origin is unknown but it could be explained by a small fluorescence of the photomultiplier housing and window as the source was placed very close to the tube. The quartz fluorescence has been reported in [90]. It has to be pointed out that this fluorescence effect is smaller for the measurement of the time constants because the radioactive source was further away from the single-photon detector and because the coincidence rate was much higher. Altogether, about 91% of the pulses are beneath the Gaussian curve.

6.4.3   Background sources and discussion

This time-resolution measurement is affected by additional background events. The production of two back-to-back gammas lead to coincidence events where one of the gammas hits the PMT directly (for example the cathode, the PMT housing or the dynode chain) and not the Plexiglas.

To investigate this effect, an additional test has been performed. Using exactly the same setup, the Plexiglas (Cherenkov radiator) has been removed. The results show the same shape as in the original measurement, however the relative number (fraction) of late ($t = 6 - 20$ ns) and "fluorescence" ($t > 20$ ns) pulses increases in both cases by a factor of about 4. The main peak in this measurement arises from direct hits of the gamma-ray in the PMT cathode where also Cherenkov light can be emitted. The increase of the events outside the Gaussian curve points to an additional background related to the new setup, possibly gamma-ray hits in the some of the PMT materials. This proves that actually more than 91% of the pulses are under the Gaussian curve. A possibility to improve the measurement is to increase the size of the Plexiglas material.

To sum up, the experiment has shown that the measuring system has a very good time resolution. However, the exact value of σ cannot be taken directly from this experiment as it is affected of an additional background compared to the decay-time measurements.

6.5   Offline analysis

The analysis of the measured data, i.e. the determination of the decay-time constants, is performed in three stages. All employed software consists of custom-made programs using the ROOT [120] analysis toolkit. In the first step, the start time of the pulses in both PMTs is determined and the difference is calculated. Second, the time resolution

of the system is estimated for each measurement. The last step is to fit the data of each measurement with a convolution of the fluorescence decay-time constants and the time resolution of the system, which is well described by a Gaussian function.

6.5.1 Determination of the photon arrival time

The aim of the first step of the analysis is to determine the time difference between the start time given by the trigger pulse and the arrival time of a single photon in the far PMT. For every measurement, two text data files are produced, in which the close PMT pulses and the single-photon pulses are stored. Examples of a close PMT pulse and a single-photon pulse are shown in figure 6.7. Each pulse consists of 2 000 sample
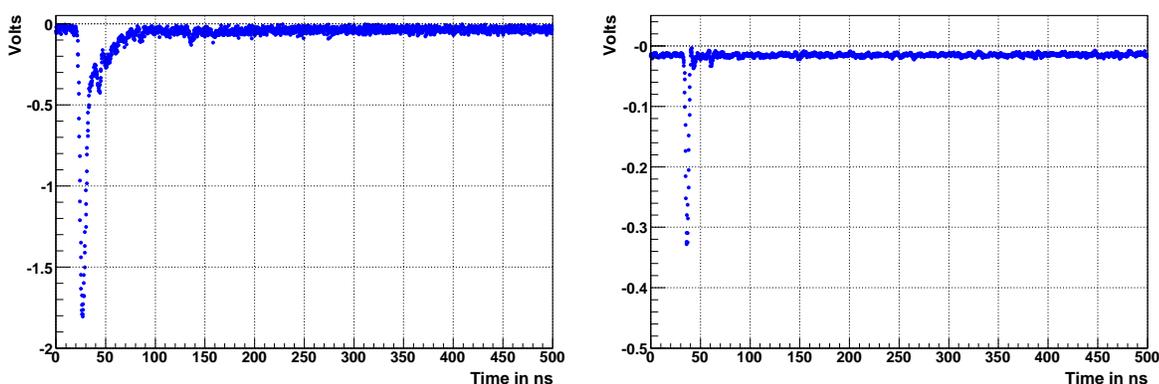
Figure 6.7: Examples of a close-PMT pulse (left) and a single-photon pulse (right).

points corresponding to 500 ns. For each recorded pulse, the first 50 points (12.5 ns) are used to determine the baseline. Next, the maximum pulse height is calculated. For this, the baseline height has to be subtracted from the pulse maximum. To determine the start-time of every pulse, a constant-fraction method has been used. The aim is to avoid triggering in the noise or in pre-pulses. The start-point of the pulse is set at 40% of the the pulse height for both PMT signals. The difference between the pulse start-times in the close PMT and in the far PMT gives the distribution of the single-photon arrival-times. An example of the distribution (logarithmic scale) is shown in the left part of figure 6.9. The distribution consists mainly of a multi-exponential decay function.

As mentioned in section 6.3, electromagnetic fields can induce noise leading to coincidence signals in both PMTs simultaneously. To reject these pulses, a soft-ware filter has been included in the analysis. An example of such a noise pulse is shown in the left part of figure 6.8.

In addition, pulses with two peaks have to be identified and cut from the data. Such
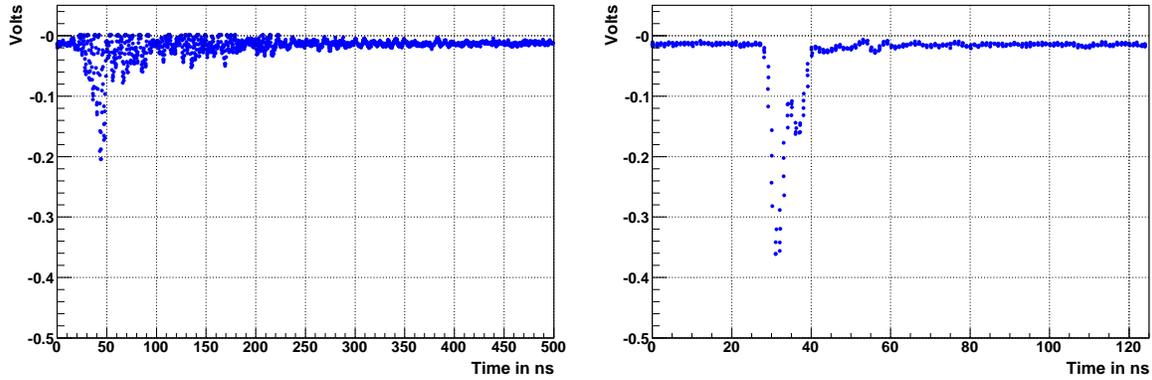
Figure 6.8: On the left: example of a noise pulse produced by electromagnetic fields in the laboratory. On the right, a zoom into an event with two peaks.

pulses appear either from after-pulses or from events in which two photons produced a photoelectron signal. In principle, it has been estimated that only 3% of the pulses produce a single photoelectron. The probability to have a two-photon signal is calculated to be 0.04% using the Poisson statistic. In these cases, the analysis program takes the arrival time of the first photon leading to a systematic error in the arrival time for shorter times. To avoid this systematic error, the pulses are removed. An example of a double pulse is shown in the right part of figure 6.8. The number of identified double pulses oscillates between 4 and 7% of the total number of pulses. This number is in the order of magnitude of the after-pulse rate specified by the provider (about 5% in $0.1\,\mu s$).

Several cuts are applied to the data at this stage. In both close and far PMTs a pulse height cut is performed. For the close PMT, a wide range of 0.1 to 1.95 V has been selected to accept as much Compton events as possible. In case of the single-photon counter, the acceptance window is the region $(0.06 - 0.47)\,V$ (1) and $(0.1 - 0.47)\,V$ (2). Thus, dark-current pulses on the low part and overflow pulses in the high part of the spectrum (see figure 6.2) are eliminated.

6.5.2 Software determination of the time resolution

In section 6.4, as an example the resolution of the system has been measured for a single sample (LAB with $10\,g/\ell$ PPO). However, as the time-resolution of the measurement also depends on the pulse height (explained in section 6.4), the resolution has to be measured for every sample. Fortunately, the resolution is monitored in each measurement. Figure 6.9 shows the distribution of the arrival times of the scintillation photons. After the maximum of the data-histogram, a multi-exponential decay can be observed. For a perfect time resolution, the distribution would be a pure multi-exponential function
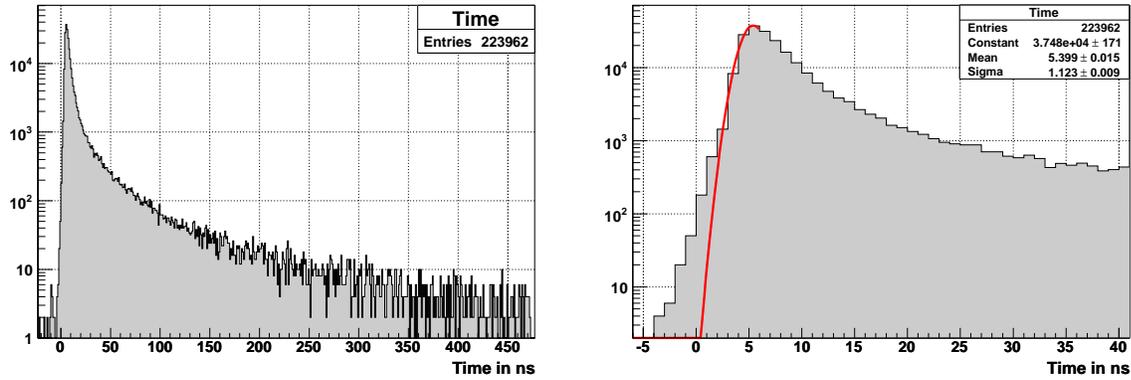
Figure 6.9: Distribution of the arrival times of single photons. On the right a zoom into the first 50 ns of the distribution of the arrival times of single photons is displayed. A Gaussian curve is fitted to the left side of the distribution.

with a sharp edge at zero time difference. As we have at least the time-jitter of the PMTs, the left-side of the distribution shows the experimental time resolution. In this plot the contribution of pre-pulses can be found as well. Similar to the measurement described in section 6.4, the main part can be described by a Gaussian function. By fitting this left-side of the arrival-time distribution (see right plot), the time resolution of the system for every measurement is obtained.

To verify this method the resolution calculated is compared with the one measured in section 6.4. The result of the experiment, $\sigma = 1.126 \pm 0.007$, is compatible within the error with the one obtained by fitting the left side as shown in figure 6.9, $\sigma = 1.123 \pm 0.009$. Hence, the fitting method explained here is reliable and can be used to estimate the resolution for every measurement.

6.5.3 Fit to the fluorescence decay times

The probability density function (PDF) $F(t)$ of the scintillation emission can be described by a convolution of a multi-exponential function with the time resolution of the measuring system:

$$F(t) = \left(\sum_i \frac{N_i}{\tau_i} \cdot e^{-\frac{(t-t_0)}{\tau_i}} \right) \otimes R(t) \tag{6.3}$$

where τ_i is the decay-time constant of the exponential function i and N_i is the area under this function such that $\sum_i N_i = 1$. t_0 is the time at which the exponential decay starts and $R(t)$ is the time-resolution function. In good approximation, the time resolution

58

can be represented by a Gaussian curve:

$$R(t) = e^{-\frac{t^2}{2\sigma^2}} \tag{6.4}$$

where σ is a known parameter. The resolution of the system for each sample is determined by fitting with ROOT a Gaussian curve to the left part of the distribution as explained in section 6.5.2.

The main fit to the data consists of a convolution of a Gaussian with the sum of three or four exponential functions. To perform the fit to the measured data, the toolkit Roofit [121] is used. This is a ROOT-based software developed by the Babar collaboration [122] where the most common convolutions for fits to physical data are already implemented. In its default configuration, Roofit performs a maximum likelihood fit and minimizes $-\log(L)$. This is a relevant feature as a maximum likelihood fit performs better when there are bins with zero content which is the case for some of the measured distributions. The minimization is performed by calling the minimization package Minuit [123] from CERN libraries. Minuit is a tool to find the minimum value of a multi-parameter function and to analyze the shape of the function around the minimum. The main advantage is that is uses several methods to make a realistic estimation of the uncertainties, including correlations between the parameters. First, MIGRAD (MInimum GRADient method) is used but if the routine takes too long automatically the SIMPLEX routine is called which gives a robust minimum but with less precision. The values obtained are given then again as starting parameters to MIGRAD which performs a more precise determination of the minimum. Next, the method HESSE determines the matrix errors by calculating the full second-derivative matrix by finite differences and inverts it. Finally, if the correlations between the different fit parameters are large, the routine MINOS follows the function from the minimum to several standard deviations away from it, instead of using the curvature at the minimum and assuming a parabolic shape. In general, this method yields different positive and negative errors (asymmetric error interval δ_{stat}).

The fit program normalizes the provided data histogram and fits the function given in equation 6.3 to it. The fit is performed by using at least three decay-time constants as two components are clearly insufficient to describe the data. The last component N_l (third or fourth depending on the sample) is defined as $N_l = 1 - \sum_{i-1} N_{i-1}$. Thus, the number of amplitudes fitted is the number of decay constants minus one. Depending on the scintillator mixture and the solute concentration, while in some cases three components are enough, in several cases four decay constants performed a better fit. To evaluate the goodness of a certain fit, the convergence of the fit has been considered but also the value of the likelihood function ($-\log(L)$). As explained in section 4.5, there are several processes which can account for the different decay-time components. However, it is unknown which processes have a significant contribution to the measurement. While the value of σ is set as fixed parameter, the amplitudes N_i, decay constants τ_i

and the start point of the exponential t_0 result from the fit. By changing σ by one sigma standard deviation, a systematic error δ_{sys} for the fitted parameters is obtained.

6.6 Results of the measurements

In this section, the results of the PDFs for several scintillator mixtures and the description of their main features are presented. In addition, the amount of light emitted by different samples is quantitatively compared. A discussion and interpretation of these studies is given in chapter 8.

6.6.1 Measurements of the probability density function

This section compiles all measured PDFs. The data of each measured sample is presented in a histogram with a bin size of 1 ns including the statistical errors. A fit with the convolution of the sum of several exponential functions with a Gaussian curve (see equation 6.3) is also depicted by a red curve. Next, for each sample three tables summarize the parameters of the fit: first the time resolution σ, next the decay constants τ_i and in the third table the amplitude of each exponential function N_i and the time, t_0 where the decay function starts. The amplitude of the last component has been calculated ($N_{l,cal}$) from the fit values and it is included in the table. Its error is difficult to calculate as it depends on the other amplitudes. However, to set a maximum error (δ_{max}) for this parameter quadratic error propagation has been used. The errors on the fitted parameters (δ_{stat} and δ_{sys}) are calculated as explained in section 6.5.3. Both systematic and statistic errors are always asymmetric. However, due to rounding some of them become symmetric.

PXE + 20 mg/ℓ bisMSB with 2 g/ℓ of pTP and PPO

Figure 6.10 shows the PDF results for three-component scintillator mixtures. While the solvent (PXE) and the secondary wavelength-shifter (20 mg/ℓ bisMSB) were the same for both cases, the primary wavelength-shifter (at 2 g/ℓ) was varied, first pTP was used and then PPO[3]. The fit to both data sets is performed with four exponential decay functions.

The distributions have a short decay constant τ_1 which accounts for the main part of the produced photons. For the mixture with PPO, the amplitude of this time constant is higher (85%) than for pTP (62%). However, the values for the decay-time constants are lower for the mixture with pTP. Although the decay times are shorter for pTP,

---

[3]For a detailed description of the scintillator components, see chapter 5.
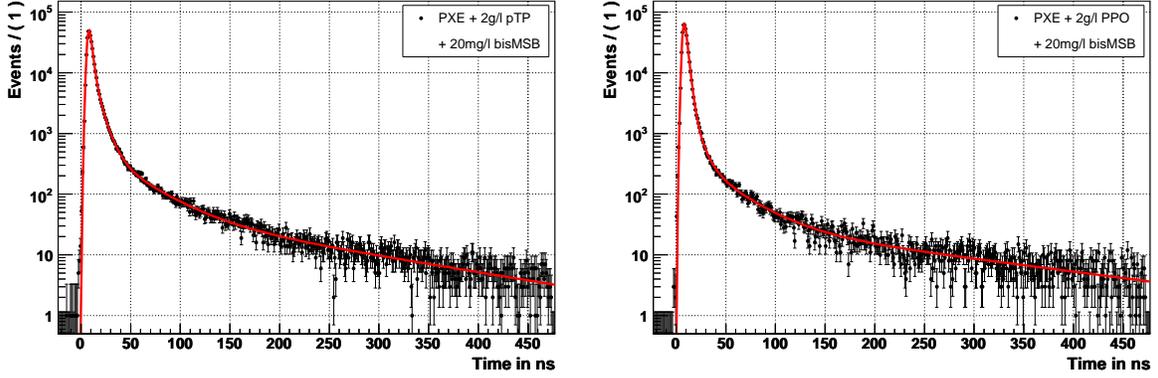
Primary solute (s)	pTP	PPO
σ (ns)	1.61 ± 0.01	1.50 ± 0.01

s	$\tau_1 \pm \delta_{stat} \pm \delta_{sys}$	$\tau_2 \pm \delta_{stat} \pm \delta_{sys}$	$\tau_3 \pm \delta_{stat} \pm \delta_{sys}$	$\tau_4 \pm \delta_{stat} \pm \delta_{sys}$	$t_0 \pm \delta_{stat} \pm \delta_{sys}$
pTP	$2.38 \pm 0.04^{+0.05}_{-0.04}$	$7.3 \pm 0.2 \pm 0.1$	$35 \pm 2^{+1}_{-0}$	$162^{+10+1}_{-9\ -2}$	$6.664^{+0.008+0.02}_{-0.008-0.02}$
PPO	$2.61 \pm 0.02^{+0.02}_{-0.03}$	$7.7 \pm 0.4^{+0.2}_{-0.3}$	$34 \pm 2^{+0}_{-1}$	205^{+13+1}_{-11-0}	$6.753^{+0.006+0.01}_{-0.006-0.01}$

s	$N_1 \pm \delta_{stat} \pm \delta_{sys}$	$N_2 \pm \delta_{stat} \pm \delta_{sys}$	$N_3 \pm \delta_{stat} \pm \delta_{sys}$	$N_{4,cal} \pm \delta_{max}$
pTP	$0.62 \pm 0.01^{+0.03}_{-0.01}$	$0.30 \pm 0.01^{+0}_{-0.01}$	$0.057 \pm 0.002^{+0.003}_{-0}$	0.023 ± 0.014
PPO	$0.853^{+0.007+0.005}_{-0.008-0.006}$	$0.097^{+0.007}_{-0.006} \pm 0.005$	$0.034 \pm 0.002^{+0.001}_{-0}$	0.016 ± 0.010

Figure 6.10: Probability density function for PXE with $2\,\mathrm{g}/\ell\,\mathrm{pTP}$ + $20\,\mathrm{mg}/\ell\,\mathrm{bisMSB}$ (left) and for PXE with $2\,\mathrm{g}/\ell\,\mathrm{PPO}$ + $20\,\mathrm{mg}/\ell\,\mathrm{bisMSB}$ (right). The plots show the time dependence of the light emission fitted according to equation 6.3 and the tables show the numerical results of the fit. All decay times τ_i, the time t_0, as well as the time resolution σ are given in ns. The amplitudes N_i are given in % having $N_{l,cal}$ been calculated from $\sum_i N_i = 1$. Its maximal error δ_{max} has been calculated as a quadratic addition.

for a detector application the mixture with PPO would be favored because of its large N_1. To have a good position reconstruction, it is important to have a high number of photons in the first nanoseconds being a large amplitude of the first decay constant N_1 an important parameter as well. The second decay constant τ_2 has a value in the same order of magnitude as τ_1. The origin of τ_2 could be connected to the solute self-absorption and reemission however, as said before, probably there is not always a single process related to the constants τ_2, τ_3 and τ_4.

The mixture with $2\,\mathrm{g}/\ell\,\mathrm{pTP}$ belong to a sample of scintillator from CTF measurements [105]. PDF measurements of this mixture have already been performed [124], however, the results are not compatible with the values reported here. Especially the two shortest components have measured values (3.78 and 15.4 ns [124] when a four-component fit is performed) which are clearly above the ones showed in figure 6.10. The difference could be related to the size of the measured sample. As will be shown in chapter 7, the effect of propagation, i.e. absorption and re-emission by the solute, result in a longer time constant. However, no information on the container size is given in [124] rendering the answer to the discrepancy to remain speculative.

PXE with 1, 2, 6 and $10\,\mathrm{g}/\ell\,\mathrm{PPO}$

Figure 6.11 shows the PDF results for mixtures of PXE solvent with 1, 2, 6 and $10\,\mathrm{g}/\ell$ PPO. This series of measurements have been performed to study the variation of the decay constants (especially the shortest one, τ_1, and its amplitude) with the solute concentration. The variation of the system's resolution (σ) with the concentration can be also appreciated. Actually, the resolution is directly related to the light output, the higher the light output the better the resolution. This effect is related to the measuring principle as the method relies on a trigger with a high number of photons to estimate the start time. In section 6.6.3, the relative light output of the presented scintillator mixtures will be presented.

The fit to the data has been performed with four exponential components. Similar to the three component mixtures, a first short time ($\tau_1 \sim 2.5\,\mathrm{ns}$) component appears accounting in this case for $\sim 82\%$ of the photons in the pulse. While the amplitude of the first component decreases with increasing concentration, the second component remains constant within the error bars and the third and fourth increase. At the same time, the shortest decay constant τ_1 decreases to $2.04\,\mathrm{ns}$ pointing to a faster energy transfer with increasing concentration. An interpretation of this behavior will be given in chapter 8.

The shortest decay constant τ_1 becomes the smallest value for high PPO concentrations. However, this is a feature of the measured sample geometry where the maximum propagation of the light is $2\,\mathrm{cm}$. As it will be shown in chapter 7, with increasing concentration the probability for solute self-absorption and reemission increases leading again to a longer time constant.
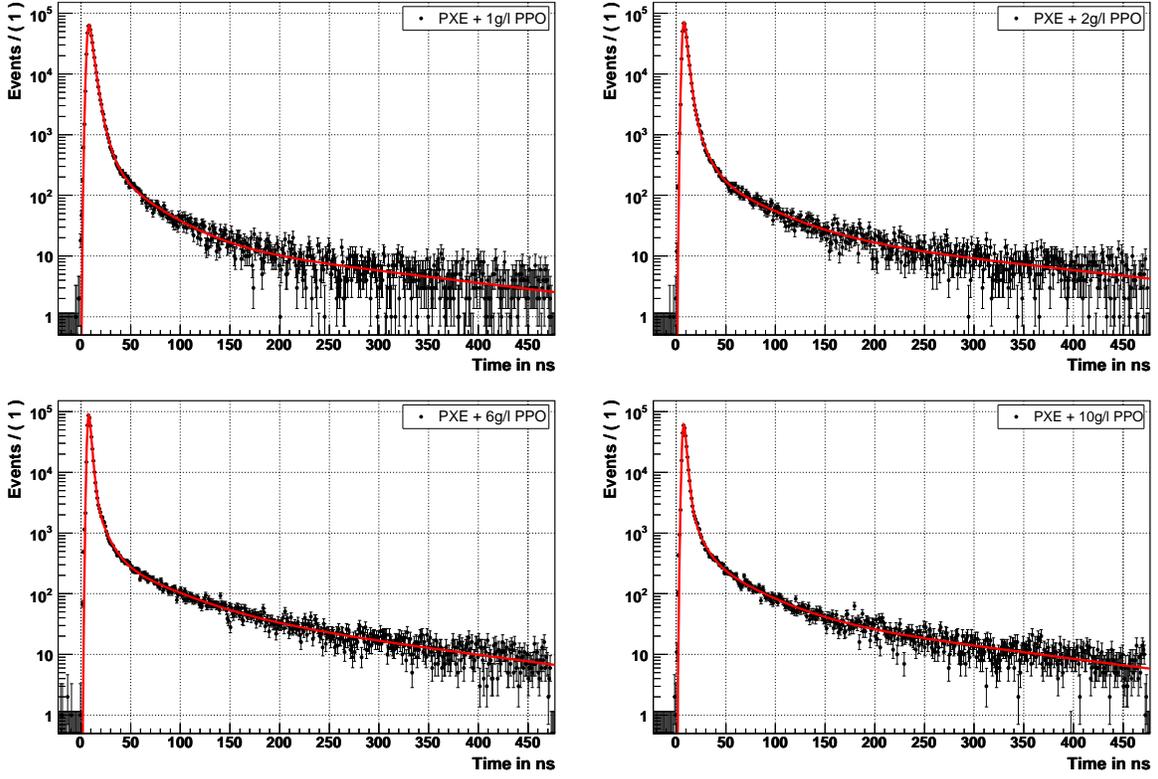
[c]	1 g/ℓ	2 g/ℓ	6 g/ℓ	10 g/ℓ
σ (ns)	1.45 ± 0.01	1.229 ± 0.007	1.066 ± 0.006	1.171 ± 0.007

[c]	$\tau_1 \pm \delta_{stat} \pm \delta_{sys}$	$\tau_2 \pm \delta_{stat} \pm \delta_{sys}$	$\tau_3 \pm \delta_{stat} \pm \delta_{sys}$	$\tau_4 \pm \delta_{stat} \pm \delta_{sys}$	$t_0 \pm \delta_{stat} \pm \delta_{sys}$
1 g/ℓ	$3.16^{+0.04}_{-0.05} \pm 0.06$	$7.7 \pm 0.7^{+0.9}_{-0.5}$	$34 \pm 3 \pm 2$	218^{+25+12}_{-19-6}	$6.631^{+0.006+0.01}_{-0.006-0.01}$
2 g/ℓ	$2.63 \pm 0.02^{+0.01}_{-0.02}$	$8.8 \pm 0.3^{+0.1}_{-0.2}$	$43 \pm 3 \pm 0$	242^{+27+2}_{-21-1}	$6.661^{+0.005+0.007}_{-0.005-0.008}$
6 g/ℓ	$2.03 \pm 0.01^{+0.01}_{-0.01}$	$9.0 \pm 0.3^{+0.1}_{-0.1}$	$47 \pm 3^{+0}_{-1}$	203^{+16+1}_{-13-0}	$6.733^{+0.004+0.006}_{-0.004-0.007}$
10 g/ℓ	$2.04 \pm 0.01^{+0.02}_{-0.01}$	$8.6 \pm 0.4^{+0.2}_{-0.1}$	40.0 ± 2.3	$207 \pm 14^{+1}_{-0}$	$6.627^{+0.005+0.008}_{-0.005-0.008}$

[c]	$N_1 \pm \delta_{stat} \pm \delta_{sys}$	$N_2 \pm \delta_{stat} \pm \delta_{sys}$	$N_3 \pm \delta_{stat} \pm \delta_{sys}$	$N_{4,cal} \pm \delta_{max}$
1 g/ℓ	$0.84 \pm 0.02^{+0.03}_{-0.02}$	$0.12^{+0.02}_{-0.01} \pm 0.02$	$0.029^{+0.003+0.001}_{-0.002-0.002}$	0.011 ± 0.028
2 g/ℓ	$0.852 \pm 0.005^{+0.002}_{-0.003}$	$0.103^{+0.005+0.002}_{-0.004-0.003}$	$0.031 \pm 0.001^{+0}_{-0}$	0.014 ± 0.007
6 g/ℓ	$0.822 \pm 0.003^{+0.001}_{-0.002}$	$0.105 \pm 0.002^{+0.001}_{-0.001}$	$0.046 \pm 0.002^{+0}_{-0}$	0.027 ± 0.004
10 g/ℓ	$0.802 \pm 0.004^{+0.002}_{-0.002}$	$0.105 \pm 0.003^{+0.001}_{-0.002}$	$0.061 \pm 0.002^{+0}_{-0.001}$	0.032 ± 0.005

Figure 6.11: PDFs for different concentrations of PPO in PXE and the time resolution σ of the system (all in ns). Further details as in figure 6.10.

63

LAB with 1, 2, 6 and $10\,\mathrm{g}/\ell$ PPO

Figure 6.12 show the results for different PPO concentrations in the solvent LAB (type P550 Q). In this case, the fit for the two lowest concentrations is performed with three exponential decay components and with four for the two higher concentrations. The histogram for the low-concentration mixtures could also be fitted with four-decay constants however, the fit was unstable. A possible explanation could be that the first and second components are too close to be resolved separately.

The fit results show that for low solute concentrations, the first time constant τ_1 in LAB as solvent is much larger than for PXE, the amplitudes N_1 being also smaller (between 56 and 77%). A possible explanation could be related to the geometry of the molecule as LAB consists of a benzene ring with a long hydrocarbon chain (see chapter 8). The long time constant τ_1 and the low correspondingly amplitude N_1 makes LAB solvent in combination with PPO unfavorable from this aspect compared to PXE as solvent. Large values of τ_1 for PPO dissolved in LAB have been also observed elsewhere [125].

PXE with 1, 2, 6 and $9\,\mathrm{g}/\ell$ PMP

In figure 6.13, the PMP solute has been investigated when it is dissolved in the solvent PXE. The highest concentration of PMP is this study was $9\,\mathrm{g}/\ell$ and not 10 as in the previous cases due to the limited amount of PMP available[4].

In this case all fits were performed by three decay components again due to the instability of the resulting fit values in case of four components. The PDFs are characterized by the absence of a decay constant of $\sim 10\,\mathrm{ns}$. For the two cases with concentrations of 1 and $2\,\mathrm{g}/\ell$, the fit was not even able to converge successfully. PMP is a wavelength-shifter with large Stokes-shift and therefore, solute self-absorption plays a minor role in the light propagation. This could explain the absence of a decay constant of the order of $10\,\mathrm{ns}$.

A further interesting feature of PMP is that although the shortest decay constant τ_1 is long compared to the ones of PPO in PXE, the amplitude N_1 is very high, between 91 and 96%. With increasing concentration, the constant τ_1 decreases but N_1 decreases as well resulting in larger values of the second and third amplitudes. The evolution of the decay constant τ_1 indicates that its minimum value could be reached at still higher solute concentrations. In this case, a high concentration could be used even for a large experiment due to the small self-absorption of PMP.

---

[4]The PMP used was a small remaining sample (few grams) from the wavelength-shifter used for the KARMEN experiment [114].
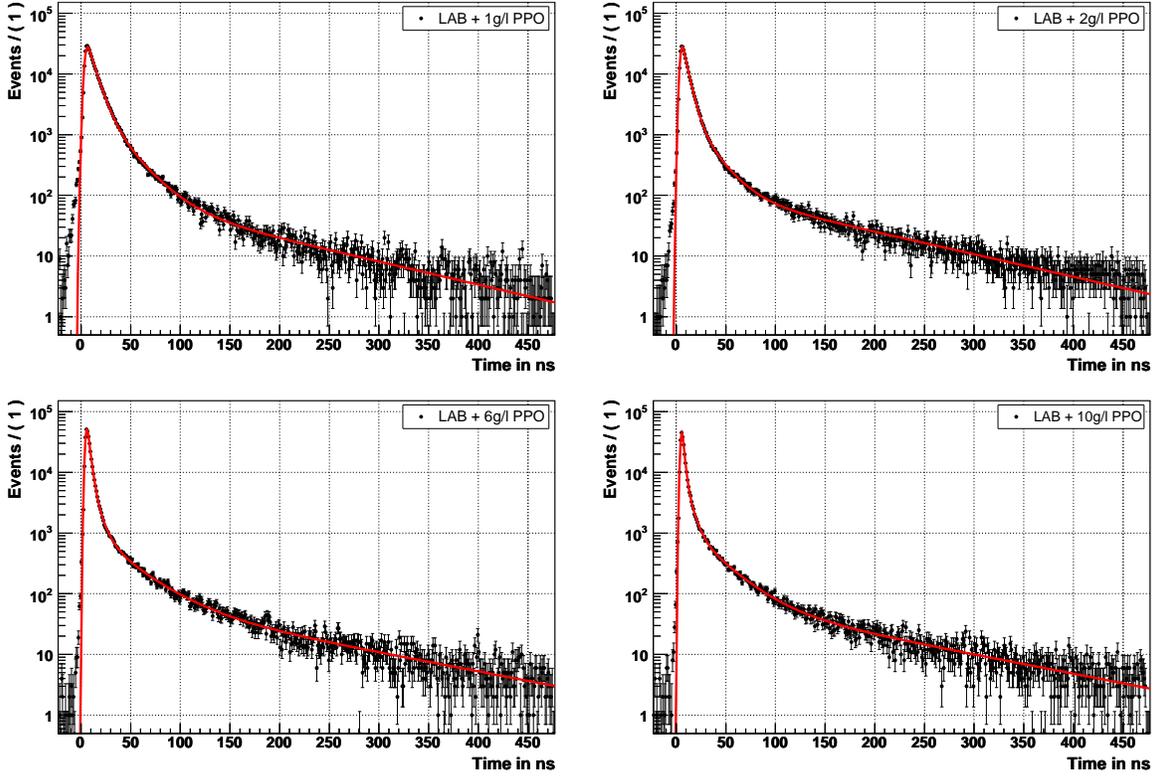
[c]	$1\,\mathrm{g}/\ell$	$2\,\mathrm{g}/\ell$	$6\,\mathrm{g}/\ell$	$10\,\mathrm{g}/\ell$
σ (ns)	1.92 ± 0.01	1.58 ± 0.01	1.236 ± 0.009	1.133 ± 0.008

[c]	$\tau_1 \pm \delta_{stat} \pm \delta_{sys}$	$\tau_2 \pm \delta_{stat} \pm \delta_{sys}$	$\tau_3 \pm \delta_{stat} \pm \delta_{sys}$	$\tau_4 \pm \delta_{stat} \pm \delta_{sys}$	$t_0 \pm \delta_{stat} \pm \delta_{sys}$
$1\,\mathrm{g}/\ell$	$7.46^{+0\ +0.04}_{-0.07-0.03}$	$22.3 \pm 0.6 \pm 0.2$	115^{+4+0}_{-3-1}	-	$4.01 \pm 0.01^{+0.01}_{-0.01}$
$2\,\mathrm{g}/\ell$	$5.21^{+0.04}_{-0.05} \pm 0.03$	$18.4 \pm 0.6 \pm 0.2$	118^{+3+0}_{-2-1}	-	$4.161^{+0.009+0.009}_{-0.009-0.01}$
$6\,\mathrm{g}/\ell$	$2.71^{+0.06+0.07}_{-0.08-0.08}$	$6.7 \pm 0.6^{+0.5}_{-0.4}$	$30 \pm 2 \pm 1$	$136^{+6}_{-5} \pm 2$	$4.577^{+0.007+0.01}_{-0.007-0.01}$
$10\,\mathrm{g}/\ell$	$1.94^{+0.04}_{-0.05} \pm 0.04$	$5.9 \pm 0.3 \pm 0.2$	$26.9^{+1\ +1}_{-0.9-0.3}$	137^{+5+0}_{-4-1}	$4.550^{+0.007+0.01}_{-0.007-0.01}$

[c]	$N_1 \pm \delta_{stat} \pm \delta_{sys}$	$N_2 \pm \delta_{stat} \pm \delta_{sys}$	$N_3 \pm \delta_{stat} \pm \delta_{sys}$	$N_{l,cal} \pm \delta_{max}$
$1\,\mathrm{g}/\ell$	$0.759 \pm 0.009^{+0.004}_{-0.003}$	$0.21 \pm 0.008^{+0.003}_{-0.003}$	-	0.031 ± 0.012
$2\,\mathrm{g}/\ell$	$0.777 \pm 0.007^{+0.003}_{-0.003}$	$0.170 \pm 0.006^{+0.002}_{-0.003}$	-	0.053 ± 0.009
$6\,\mathrm{g}/\ell$	$0.65^{+0.03}_{-0.04} \pm 0.03$	$0.21^{+0.02+0.03}_{-0\ -0.02}$	$0.100 \pm 0.004^{+0.002}_{-0.003}$	0.040 ± 0.036
$10\,\mathrm{g}/\ell$	$0.56 \pm 0.02 \pm 0.01$	$0.27 \pm 0.01 \pm 0.01$	$0.133 \pm 0.004^{+0.01}_{-0.02}$	0.037 ± 0.023

Figure 6.12: PDFs for different concentrations of PPO in LAB and the time resolution σ of the system (all in ns). Further details as in figure 6.10.
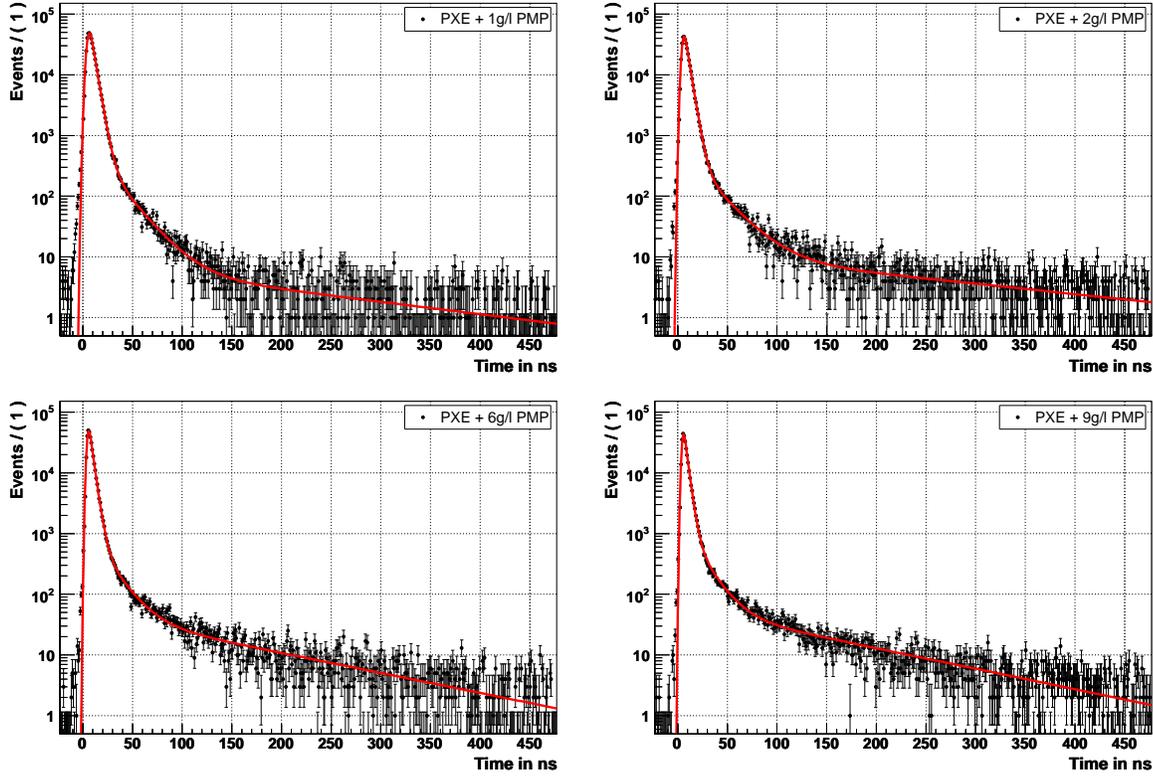
[c]	1 g/ℓ	2 g/ℓ	6 g/ℓ	9 g/ℓ
σ (ns)	2.12 ± 0.01	1.77 ± 0.01	1.362 ± 0.009	1.258 ± 0.009

[c]	$\tau_1 \pm \delta_{stat} \pm \delta_{sys}$	$\tau_2 \pm \delta_{stat} \pm \delta_{sys}$	$\tau_3 \pm \delta_{stat} \pm \delta_{sys}$	$t_0 \pm \delta_{stat} \pm \delta_{sys}$
1 g/ℓ	$4.30 \pm 0.01^{+0.01}_{-0.02}$	$21.4 \pm 0.6 \pm 0.2$	212^{+22+3}_{-18-1}	$4.466 \pm 0.007 \pm 0.009$
2 g/ℓ	$4.15 \pm 0.01 \pm 0.01$	$23.7 \pm 0.8 \pm 0.2$	255^{+23+2}_{-20-3}	$4.557 \pm 0.007^{+0.008}_{-0.009}$
6 g/ℓ	$3.62 \pm 0.01 \pm 0.01$	$18.5 \pm 0.7^{+0.3}_{-0.2}$	$137 \pm 5 \pm 1$	$4.375 \pm 0.006 \pm 0.008$
9 g/ℓ	$3.44 \pm 0.02 \pm 0.01$	$17.6 \pm 0.7 \pm 0.3$	$135 \pm 4 \pm 1$	$4.381 \pm 0.006^{+0.008}_{-0.007}$

[c]	$N_1 \pm \delta_{stat} \pm \delta_{sys}$	$N_2 \pm \delta_{stat} \pm \delta_{sys}$	$N_{3,cal} \pm \delta_{max}$
1 g/ℓ	$0.956 \pm 0.001^{+0}_{-0.001}$	$0.032 \pm 0.001 \pm 0$	0.012 ± 0.001
2 g/ℓ	$0.959 \pm 0.001^{+0}_{-0.001}$	$0.035 \pm 0.001^{+0}_{-0.001}$	0.006 ± 0.001
6 g/ℓ	$0.935 \pm 0.002^{+0}_{-0.001}$	$0.048 \pm 0.002^{+0.001}_{-0}$	0.017 ± 0.003
9 g/ℓ	$0.912 \pm 0.006 \pm 0.001$	$0.064 \pm 0.002 \pm 0.001$	0.024 ± 0.006

Figure 6.13: Summary of the fluorescence decay constants for different concentrations of PMP in PXE and the time resolution σ of the system (all times in ns). Further details as in figure 6.10.

PXE with 1 and 2 g/ℓ bisMSB

Figure 6.14 shows the PDFs of bisMSB dissolved with concentrations of 1 and 2 g/ℓ in PXE. BisMSB is commonly used as secondary wavelength-shifter because its absorption
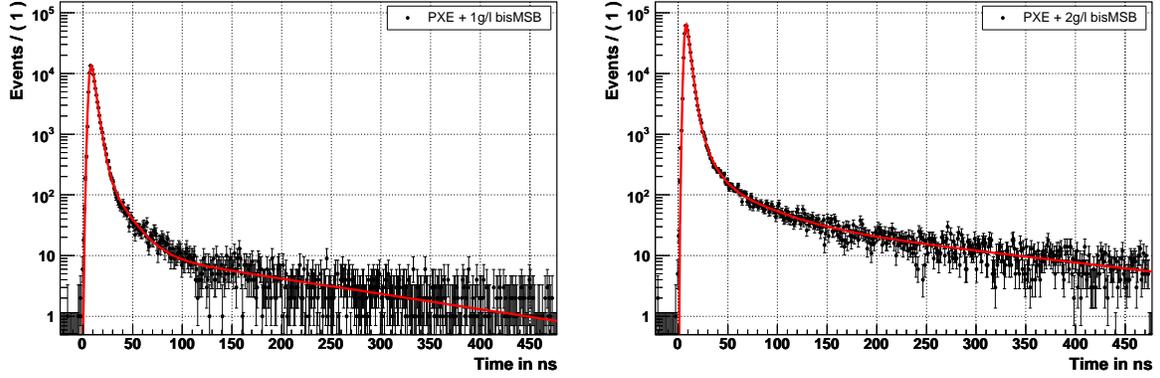
[c]	1 g/ℓ	2 g/ℓ
σ (ns)	1.58 ± 0.02	1.352 ± 0.009

[c]	$\tau_1 \pm \delta_{stat} \pm \delta_{sys}$	$\tau_2 \pm \delta_{stat} \pm \delta_{sys}$	$\tau_3 \pm \delta_{stat} \pm \delta_{sys}$	$\tau_4 \pm \delta_{stat} \pm \delta_{sys}$	$t_0 \pm \delta_{stat} \pm \delta_{sys}$
1 g/ℓ	$3.60^{+0.03+0.01}_{-0.04-0.02}$	$15.8 \pm 1.0 \pm 0.3$	172^{+11+2}_{-10-1}	-	$6.59 \pm 0.01^{+0.01}_{-0.01}$
2 g/ℓ	$2.99 \pm 0.02^{+0.02}_{-0.03}$	$8.9 \pm 0.5^{+0.2}_{-0.3}$	$40 \pm 4^{+0}_{-1}$	277^{+18+1}_{-15-2}	$6.665^{+0.006}_{-0.005} \pm 0.01$

[c]	$N_1 \pm \delta_{stat} \pm \delta_{sys}$	$N_2 \pm \delta_{stat} \pm \delta_{sys}$	$N_3 \pm \delta_{stat} \pm \delta_{sys}$	$N_{l,cal} \pm \delta_{max}$
1 g/ℓ	$0.909^{+0.005}_{-0.006} \pm 0.002$	$0.071^{+0.006+0.001}_{-0.005-0.002}$	-	0.020 ± 0.008
2 g/ℓ	$0.860^{+0.007+0.005}_{-0.009-0.006}$	$0.095^{+0.008+0.005}_{-0.006-0.004}$	$0.024 \pm 0.002^{+0.001}_{-0}$	0.021 ± 0.012

Figure 6.14: Probability density function for PXE with 1 g/ℓ and 2 g/ℓ bisMSB. Further details as in figure 6.10.

spectrum overlaps with the emission spectra of common primary wavelength-shifters. The measurements were performed without primary fluor to find out to which extend the overlap of the solvent emission-spectrum (for PXE: peak value at 290 nm) and the solute absorption-spectrum (peak of bisMSB at 345 nm) plays a role in the fluorescence decay constants. The values of τ_1 for both concentration (~ 3 and 3.6 ns) are not very large revealing that the solvent and solute spectra are not the main cause for a large τ_1. However, the light output for theses mixtures is significantly lower (see section 6.6.3).

The mixture with 1 g/ℓ has been fitted with three components while the mixture with 2 g/ℓ with four. In this case, the absence of a fourth component for the low concentration could be due to the low statistics of this measurement.

67

Dodecan + 2 g/ℓ PPO and LAB + 2 g/ℓ PMP

Figure 6.15 shows the PDFs of the non-scintillating oil named dodecan with 2 g/ℓ PPO and of LAB with 2 g/ℓ PMP. The mixture using dodecan has been fitted with four decay-
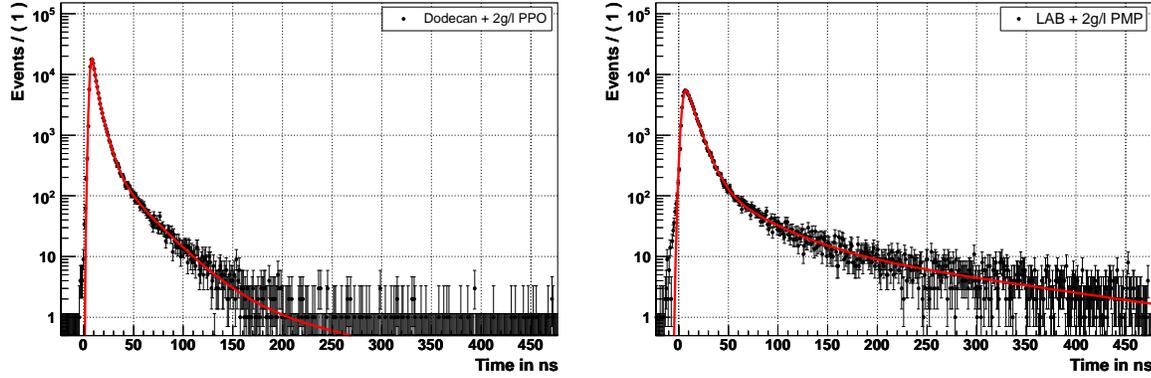
Solvent (S)	Dodecan	LAB
Primary solute	PPO	PMP
σ (ns)	1.44 ± 0.014	2.36 ± 0.03

S	$\tau_1 \pm \delta_{stat} \pm \delta_{sys}$	$\tau_2 \pm \delta_{stat} \pm \delta_{sys}$	$\tau_3 \pm \delta_{stat} \pm \delta_{sys}$	$\tau_4 \pm \delta_{stat} \pm \delta_{sys}$	$t_0 \pm \delta_{stat} \pm \delta_{sys}$
Dodecan	$2.43 \pm 0.2 \pm 0.2$	$6.3 \pm 0.3 \pm 0.2$	$26 \pm 1^{+0}_{-1}$	120^{+30+6}_{-18-5}	$6.62 \pm 0.01^{+0.03}_{-0.04}$
LAB	$8.53 \pm 0.08^{+0.07}_{-0.07}$	$38 \pm 3^{+1}_{-0}$	$182^{+19}_{-15} \pm 2$	-	$4.20 \pm 0.02^{+0.04}_{-0.04}$

S	$N_1 \pm \delta_{stat} \pm \delta_{sys}$	$N_2 \pm \delta_{stat} \pm \delta_{sys}$	$N_3 \pm \delta_{stat} \pm \delta_{sys}$	$N_{l,cal} \pm \delta_{max}$
Dodecan	$0.39^{+0\ +0.04}_{-0.04-0.03}$	$0.52^{+0\ +0.02}_{-0.03-0.03}$	$0.084 \pm 0.006^{+0.003}_{-0.003}$	0.006 ± 0.050
LAB	$0.851^{+0.006+0.003}_{-0.007-0.002}$	$0.105 \pm 0.005^{+0.002}_{-0.001}$	-	0.044 ± 0.009

Figure 6.15: PDF for dodecan with 2 g/ℓ PPO and for LAB with 2 g/ℓ PMP. Further details as in figure 6.10.

constants and shows a quite different shape compared with the ones presented up to now. It has two relatively short components which account for 39 and 52% of the pulses, respectively. The third one has an amplitude of 8.4%, having the fourth one only 0.6%. This low amplitude suggests than the longest decay constant could be solvent-related as for other mixtures, where the solvents consist of scintillating molecules, the longest component accounts for a few % of the photons produced in a pulse.

For the case LAB with PMP, the decay constant $\tau_1 = 8.53$ ns is quite long showing that the energy transfer between LAB and PMP is not very efficient. It would be of interest to study the evolution of this short decay constant with increasing PMP

concentration as for LAB with PPO a very short time constant τ_1 has been observed for high solute concentrations.

6.6.2 Discussion of the errors and outlook

In the presented results, the fluorescence decay-constant τ_1 is determined with an uncertainty of few per cent (between 1 and 8%). The question which arises immediately is the reliability of these relatively small errors especially when strong correlations between the time resolution and the shortest decay constant have been found. There is no definite answer but further tests could be performed in order to test the given systematic errors.

In section 6.4, an experiment has been presented to estimate the resolution of the measuring system. It has been shown that to a large extent a Gaussian curve describes the resolution of the system. However, photomultiplier-related contributions (e.g, pre- and late-pulses) differ from the Gaussian shape. A further systematic study could be performed where the system resolution function is parametrized with the sum of a Gaussian and additional non-Gaussian contributions (e.g. polynomial). By simulating a convolution of this response function with an exponential decay and comparing to the convolution with a Gaussian function, a possible systematic error of the time-constants determination could be extracted.

6.6.3 Determination of the relative output

Besides the measurements of the fluorescence decay constants, the relative light output of the different samples can be derived from the data. For every sample, both the close- and the far-PMT signals have been recorded. The close-PMT signals can be expected to correspond to a Compton spectrum if, for example, the pulse height is plotted. However, the spectrum is affected by a trigger acceptance because the data selection is bias by the trigger. Due to the coincidence requirement for the trigger, events with a large energy deposition are favored. For such events, the number of produced photons is higher and the probability to have a single photon in the far PMT (and therefore a trigger) is also higher. This effect distorts the spectrum and a difference between large light outputs is larger than the same difference for low outputs.

To determine the relative light output of a scintillator mixture, a Gaussian function has been fitted around the maximum of the pulse height spectrum which corresponds approximately to the Compton edge. Figure 6.16 shows an example for the close PMT. The light output is then extracted from the position of the Gaussian peak. The statistical error for the position δ_{stat} is given by the fit. A systematic error δ_{sys} has been derived by taking the spectra recorded at different days and looking for oscillations in the position of the Gaussian peak.

69
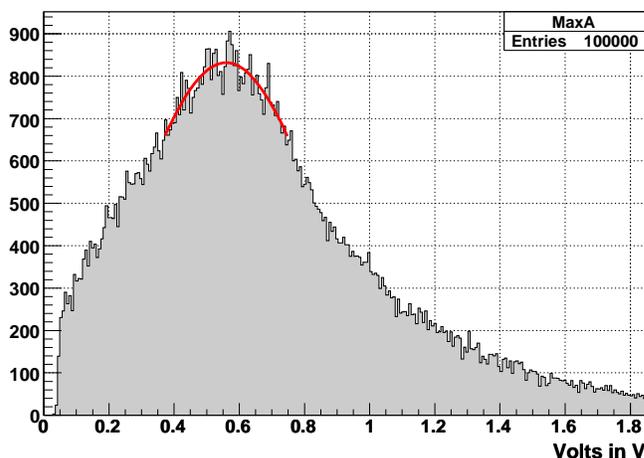
Figure 6.16: Spectrum of the pulse height in the close PMT. A Gaussian curve is fitted approximately around the maximum to determine the relative light output.

This estimate of the light output is not a very precise method but it delivers a qualitative variation of the light output depending on the mixture or the solute concentration. In this way, a first hint on the relative light output can be obtained. An improved method to compare light yields of different materials is to select the Compton edge of a gamma interaction (as performed in [51]). For this purpose a coincidence setup can be designed where back-scattered gammas are selected by using a coincidence, for example under 180°, with a further detector. In this case, the energy of the scattered electron corresponding to the Compton edge is selected. A Gaussian distribution appears around this energy due to the energy resolution of the system.

Table 6.2 summarizes the relative light outputs for mixtures of PXE- PPO, LAB-PPO and PXE-PMP with the light output of PXE + 6g/ℓ PPO being normalized to 1 as this is the highest measured light output. For the first two mixtures, the light output increases with the concentration up to 6g/ℓ PPO and then it decreases slightly. This behavior can be compared with the results of the resolution σ shown in figure 6.11 and 6.12. The time resolution of the measuring system gets better (smaller) for a higher light output. For PMP solute dissolved in PXE, the light output increases continuously up to the maximum concentration of 9 g/ℓ. Therefore, the maximum light output for this system is probably at a still larger concentration. Figure 6.17 shows a comparison of the light output of the mentioned systems.

It has to be emphasized here that this relative light-output comparison is based on the pulse-height spectra of the measured samples. As shown in section 6.6.1, the time constant of LAB-PPO and PXE-PMP is larger than that for PXE-PPO and thus for LAB-PPO, the emission time of the photons in a pulse is more smeared out and the peak
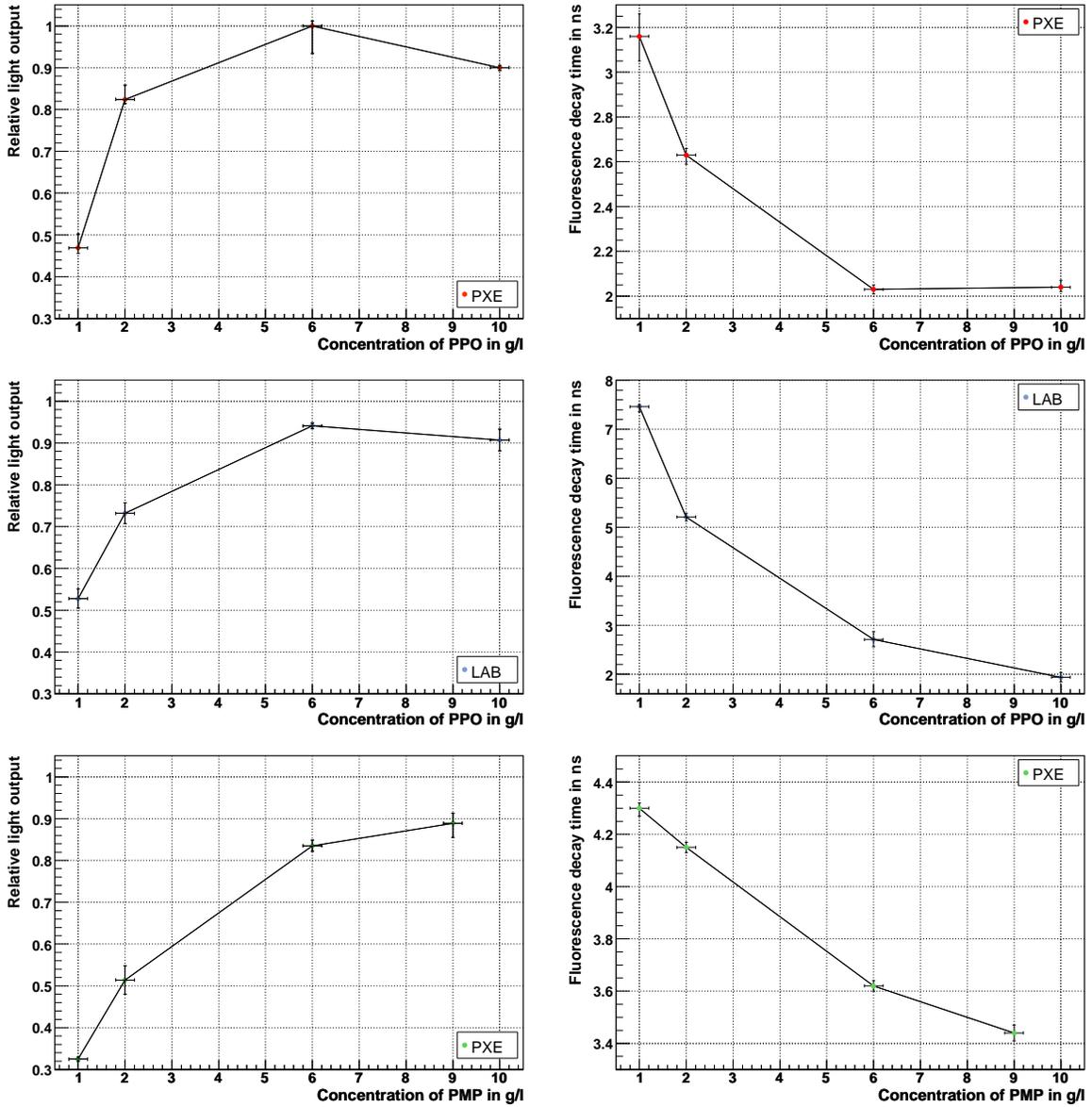
Figure 6.17: Left: evolution of the light output with the solute concentration for the mixtures PXE-PPO, LAB-PPO and PXE-PMP. Right: the evolution of the shortest fluorescence decay constant τ_1 is shown for the same systems. The errors in the concentrations are mainly coming from the precision of the balance for determining the weight. The errors in the light output are the linear sum of the statistical error and the systematic error. Due to a bias in the data selection via the trigger, the absolute differences between the light outputs are only qualitatively correct (see text).

71

[c]	$Y_{PXEPPO} + \delta_{stat} + \delta_{sys}$	$Y_{LABPPO} + \delta_{stat} + \delta_{sys}$	$Y_{PXEPMP} + \delta_{stat} + \delta_{sys}$
$1\,g/\ell$	$0.469 \pm 0.003^{+0.03}_{-0.01}$	$0.528 \pm 0.003 \pm 0.02$	$0.316 \pm 0.002 \pm 0.003$
$2\,g/\ell$	$0.824 \pm 0.004 \pm 0.03$	$0.732 \pm 0.005 \pm 0.02$	$0.499 \pm 0.004 \pm 0.03$
$6\,g/\ell$	$1.000 \pm 0.006^{+0.006}_{-0.06}$	$0.941 \pm 0.005 \pm 0.002$	$0.811 \pm 0.004^{+0.009}_{-0.01}$
$9\,g/\ell$	-	-	$0.863 \pm 0.004^{+0.02}_{-0.03}$
$10\,g/\ell$	$0.900 \pm 0.004^{+0.001}_{-0.003}$	$0.907 \pm 0.006 \pm 0.02$	-

Table 6.2: Summary of the relative light outputs of mixtures of PPO in PXE (left column) and LAB (middle) and PMP in PXE (right). Due to a bias in the data selection via the trigger, the absolute differences between the light outputs are only qualitatively correct (see text).

	Mixture	$Y + \delta_{stat} + \delta_{sys}$
(1)	PXE + $2\,g/\ell$ pTP + $20\,mg/\ell$ bisMSB	$0.596 \pm 0.003 \pm 0.007$
(2)	PXE + $2\,g/\ell$ PPO + $20\,mg/\ell$ bisMSB	$0.711 \pm 0.004 \pm 0.01$
(3)	PXE + $1\,g/\ell$ bisMSB	$0.325 \pm 0.001^{+0.001}_{-0.003}$
(4)	PXE + $2\,g/\ell$ bisMSB	$0.537 \pm 0.003 \pm 0.006$
(5)	Dodecan + $2\,g/\ell$ PPO	$0.358 \pm 0.003^{+0.03}_{-0.02}$
(6)	LAB + $2\,g/\ell$ PMP	$0.776 \pm 0.004 \pm 0.01$

Table 6.3: Summary of the relative light outputs in additional systems investigated. Due to a bias in the data selection via the trigger, the absolute differences between the light outputs are only qualitatively correct (see text).

decreases. A similar analysis of the data could be performed by taking the spectrum of the pulse area to compare the total number of emitted photons. It is expected that in such an analysis the relative light output of LAB-PPO, for example at $2\,g/\ell$, is larger than PXE-PPO due to its larger τ_1 lifetime.

Table 6.3 shows the relative light output for the rest of the mixtures measured. A further factor which should be taken into account when relative light outputs are compared is the emitted wavelength. For the mixtures which spectra overlaps to a large extend with the cathode sensitivity, the relative light output measured is higher. As an example, the peak value of the emission spectra for PMP correspond to a cathode sensitivity of 75% of the maximum. Although this cathode spectral correction can be easily performed, here it hasn't been done as the quantitative relative light output has, as mentioned before, a bias in the data selection via the trigger.

In table 6.3 can be observed that, for the three-component mixtures (1) and (2), the energy transfer in the sample containing PPO is performed more efficiently as it produces larger amount of light. The mixtures with bisMSB, (3) and (4), have a relatively small

light output showing that its use in high concentrations and only with one solvent is not desired for a detector application. The same applies for dodecan (5). As explained before, dodecan is a non-scintillating organic liquid and therefore it wasn't expected to see much light emission. The last mixture seems very promising as the relative light output is rather high. It would be interesting to see the evolution of the LAB light output with increasing PMP concentration.

Chapter 7

Spectroscopy measurements

For the choice of a liquid-scintillator mixture, several parameters have to be taken into account. The scintillation emission spectrum is one of them as it has an impact on the light propagation through the liquid. Absorption and scattering processes are actually wavelength dependent. Additionally, the photo-cathode of the light sensors in the experiment has a wavelength-dependent sensitivity. For these reasons, emission spectra of several samples have been studied and are presented in this chapter. Two methods have been used for the excitation of the scintillator: an ultraviolet-light emitter (a Deuterium lamp) and an electron beam of about $10\,\text{keV}$ energy. The experimental setups for both methods are described. The experiments were performed from July to November 2007 at the spectroscopy laboratory of E12 at the MLL (Maier-Leibnitz-Laboratorium) in the tandem accelerator building in Garching.

7.1 Spectrometer

The scintillation light is detected and analyzed by an Ocean Optics HR2000CG-UV-NIR spectrometer [126]. After a short description of the analyzing device, the calibration of the response of the spectrometer at different wavelengths and the calibration concerning shifts in the wavelength are explained.

7.1.1 Description

The Ocean Optics HR2000CG-UV-NIR is a medium-resolution miniature spectrometer [126] which covers a wavelength range from 200 to $1100\,\text{nm}$ with a resolution of $0.53\,\text{nm}$ (full width at half maximum, FWHM) [127]. The light is introduced into the spectrometer through a quartz light-guide ($210\,\text{cm}$ long and $600\,\mu\text{m}$ in diameter). The module utilizes a $5\,\mu\text{m}$ entrance slit. Inside the spectrometer, the light is focused on a

blaze grating. This grating, which has a groove-spacing density of 300 lines/mm, ana-
lyzes the spectral information and a mirror focuses the light in the detection plane. The
light is finally recorded in a Sony ILX511 linear CCD (charge-coupled device) array.
Special filters for the ultraviolet (UV) and near infrared (NIR) regions are included.

The readout of the detector is performed extracting the CCD data by a USB cable
which connects the spectrometer to a computer. On a Windows machine, Ocean Optics
software is installed to read incoming data. The output is stored in text files and can
be analyzed offline with a custom-made ROOT [120] program.

7.1.2 Calibration

The spectrometer has to be calibrated in order to identify erroneous shifts of the mea-
sured wavelength. A shift can originate from a mechanical angle shift in the CCD
camera or from an erroneous allocation of the wavelength in the software. In addition,
the spectra have to be corrected for the intensity response at different wavelengths. For
the calibration of the wavelength, an argon lamp is used. Figure 7.1 (left) shows the
measured spectrum of the argon lamp. The positions of distinct lines in the spectrum
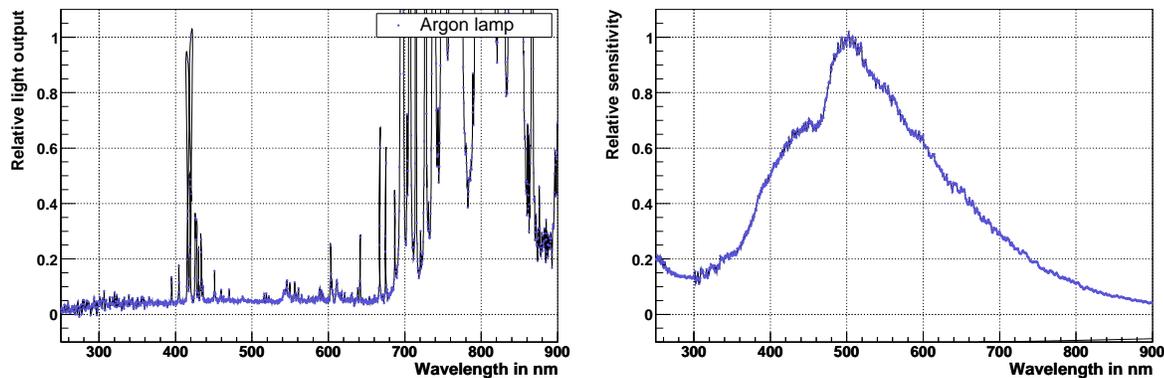
Figure 7.1: Left: measured spectrum of the argon lamp. Right: measured response of
the spectrometer at different wavelenghts. The detector is most sensitive at 500 nm,
while e.g. at 300 nm the efficiency drops to 15% of the maximum.

are well known. These lines correspond to transitions of excited or ionized states of Ar_2
molecules. Several lines between 250 and 650 nm were used. The calibration showed a
shift of the argon spectrum by 1.22 ± 0.04 nm to higher values of the wavelength. The
error given is the standard deviation of the mean value measured for the shift.

The dependence of the sensitivity as a function of the wavelength is measured with
the help of a standard halogen lamp (LOT-Oriel [128]). The lamp has a very precisely

known spectral form (when it is powered with 6.6 A and 16.1 V and the spectrum is measured at 70 cm distance). The spectrometer was placed at this distance and the measured spectrum was compared to the one given by the manufacturer of the halogen lamp. In figure 7.1 (right), the relative response of the spectrometer to different wavelenghts is shown.

The shape of the intensity response is due to the overlap of several filters in front of the CCD array. These filters are optimized for different wavelength regions and by combining them a wide sensitive wavelength-region is obtained. In the following data analysis, both described corrections (intensity response, wavelength shifts) have been taken into account.

7.2 Spectra obtained by excitation with UV-light

The first approach to measure the emission spectrum of a scintillator is to excite the π-orbitals of the solvent molecules (see chapter 4) by ultraviolet light. In this section, the description of the experimental setup is presented.

7.2.1 Description of the experiment

As an UV-light source, a deuterium lamp is used. The lamp is a low-pressure gas-discharge light source. The optical output-window of the lamp is made of magnesium fluoride in order to prevent UV-light absorption. A zoom $(250 - 900 \, \text{nm})$ into the
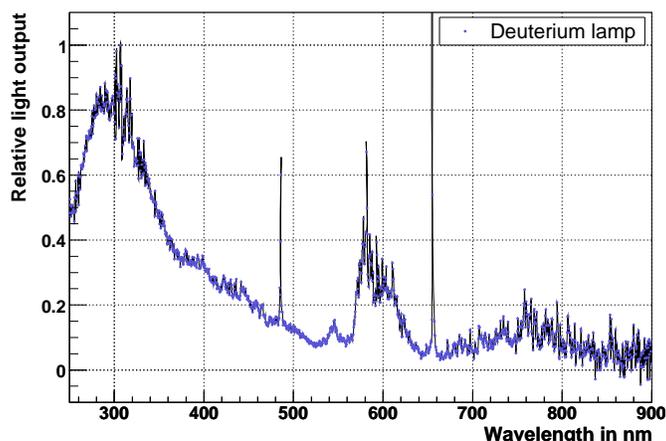
Figure 7.2: Measured spectrum of the deuterium lamp. The spectrum is corrected for the spectral response function of the detection system (see figure 7.1).

measured spectrum of the lamp is shown in figure 7.2. The emission spectrum covers a wide wavelength range with a significant contribution in the UV-region originating from the molecular continuum of the deuterium molecule D_2. Molecular transition of D_2 are also responsible for the Fulcher-α band from 560 to 640 nm. Furthermore, characteristic hydrogen Balmer lines, D_α and D_β, can be seen at 486 and 656 nm, respectively.

The light emitted by the lamp is collimated by a quartz lens and focused onto the scintillator sample as shown in figure 7.3. The lens is placed about 0.5 cm in front of the
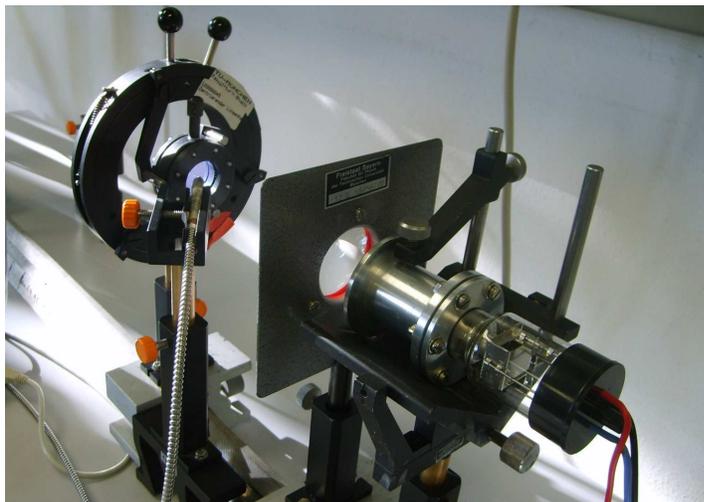
Figure 7.3: Picture of the setup.

lamp. The choice of the lens material is important to avoid the absorption of the UV part of the spectrum. The image of the light source (about 25 cm from the lens) had to be determined carefully.

The UV-light is absorbed in the first μm to mm of the liquid. Therefore, the emission takes place also in the foremost layer of the scintillator sample. For each measurement, a light guide was used to collect the emitted light and to pass it onto the spectrometer's aperture. The light guide was positioned in two different configurations, A and B as shown in the figure 7.4. In position A, the light guide is placed on the same side as the deuterium lamp while in position B, the light guide is placed on the other side. In both cases, the spectrum was observed with a 45° angle relative to the light-beam. In position B, the light emitted by the scintillator propagates through ~ 1.4 cm of liquid (as the length of the scintillator container is 1 cm and the angle 45°). For position A, propagation effects are almost negligible as the emission takes place in the first molecular planes. In both positions, the light crosses two quartz surfaces leading to an equal loss of light due to reflections. Using the Fresnel [129] formula and taking a refraction index of 1.0 for air, 1.55 for quartz and 1.53 for scintillator, it can be shown that for every
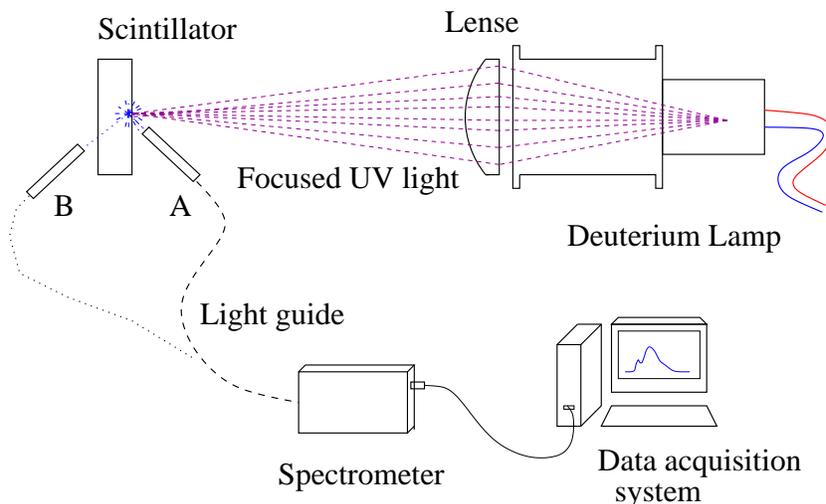
Figure 7.4: Setup of the spectral measurement of liquid scintillators when exciting the sample with UV-light (deuterium lamp).

transition from air to quartz and from quart to scintillator about 4.7% of the light is lost. However, the transition from quartz to scintillator makes a negligible contribution. Finally, the scintillation light is analyzed with the spectrometer as described in the previous section.

Every scintillator mixture tested consists of a solvent and at least one solute. When UV-light enters the mixture, mainly solvent molecules are excited. The solvents used are PXE and LAB (see chapter 5). Both efficiently absorb UV-light (absorption peaks are at 270 and 260 nm, respectively) and emit at longer wavelength values (emission at 290 and 283 nm respectively). As explained in chapter 4, the energy of the solvent is transferred to the solute (wavelength-shifter) molecules. Therefore, the measured spectra arise mainly from the solute emission. The absorption spectra of the solute molecules overlap slightly with their own emission spectra[1]. Hence, short wavelengths are expected to be absorbed to a large extent after the propagation through the liquid.

7.2.2 Measured emission spectra

In this section, the experimental spectra measured with the UV-light excitation method are presented. The full names, formulas and properties of the scintillator components used can be found in chapter 5. For every scintillator mixture, two data sets are plotted together: in blue, the direct emission spectra that were recorded when the light guide was placed on position A (see figure 7.4); in red open circles, the spectra obtained with

---

[1] Absorption and emission spectra of several components can be found in [94].

the light guide in position B. The normalization is performed such that the spectrum measured in position A has its maximum at 1. The spectrum at position B is normalized by adjusting the spectral tail to the same height as that of spectrum A. All shown spectra are corrected for the spectral response of the detection system. In some of the data sets, the UV-region is quite noisy; the reason is the comparatively low sensitivity of the spectrometer in this wavelength region (see right part of figure 7.1). Moreover, some background light above $\sim 550\,\mathrm{nm}$ appears in some figures. This is due to a contribution of scattered Sun light during the measurements. The precision of the spectra depend on the wavelength region but overall a precision of at least 10% is obtained.

Figure 7.5 displays emission spectra of several wavelength-shifters dissolved in PXE.
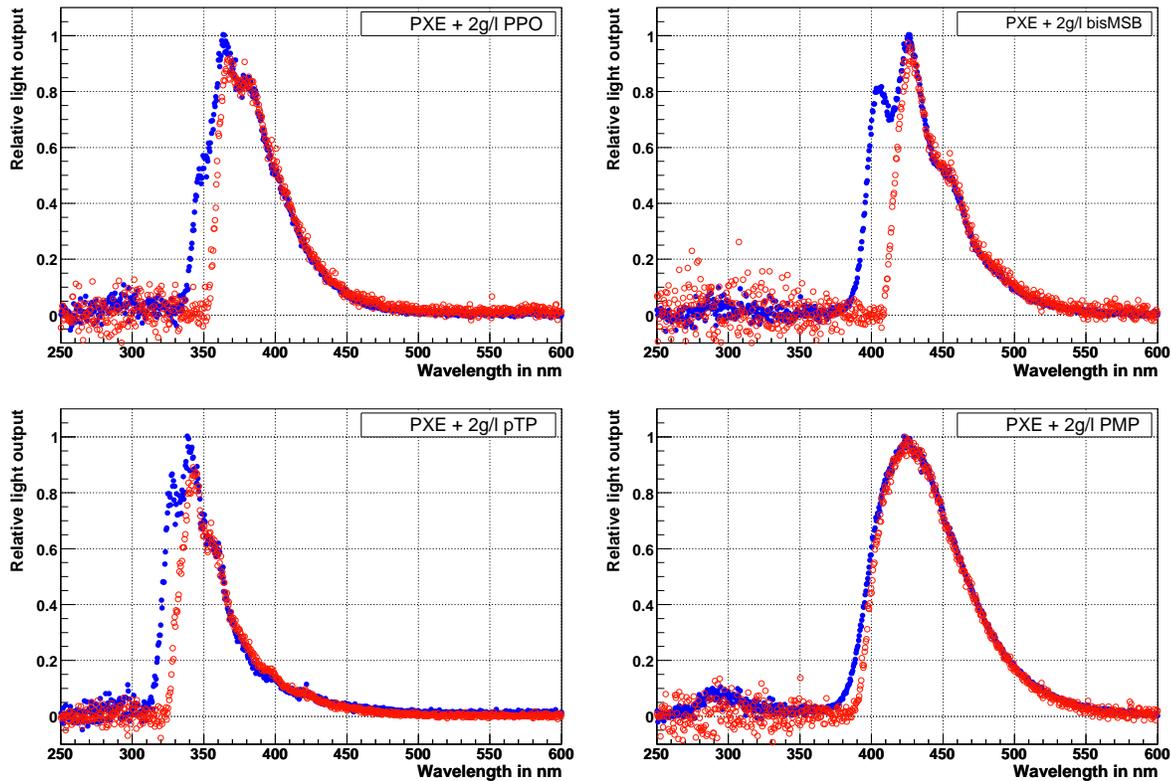
Figure 7.5: Emission spectra obtained with the UV-light excitation method. Blue circles represent data points of the direct emission spectrum (light guide in position A, see figure 7.4) and the red open circles the spectrum after $\sim 1.4\,\mathrm{cm}$ propagation through the mixture (light guide in position B). All samples were based on the solvent PXE. The wavelength-shifters, always with a concentration of 2 g/l are: PPO, bisMSB, pTP and PMP (for a description of the components see chapter 5).

The two on the left (PPO and pTP) are primary wavelength-shifter. PPO emits between

80

~ 330 and $450\,\mathrm{nm}$ and pTP between ~ 310 and $430\,\mathrm{nm}$. The upper spectrum on the right belongs to the secondary wavelength-shifter bisMSB. BisMSB absorbs where primary solutes emit (around $350\,\mathrm{nm}$) and emits from ~ 380 to $\sim 520\,\mathrm{nm}$. Alternatively, a single large Stokes-shift solvent like PMP (lower plot on the right) can be used. PMP has the advantage that its absorption spectrum peaks at about $300\,\mathrm{nm}$ while the emission is from 380 to $530\,\mathrm{nm}$. This leads to a highly reduced self-absorption compared to combinations of PPO/pTP with bisMSB that produces similarly large shifts but features self-absorption of the secondary fluor. This is corroborated by the small difference between the spectra for PMP at the positions A and B.

Except for the PMP solute, the emission spectra show four main peaks. For example in the case of the PPO solute (upper left in figure 7.5), the peaks are at approximately 350, 365, 380 and $395\,\mathrm{nm}$. These peaks show the energy spacing between the first singlet excited state, S_1, and the different vibrational levels of the ground state, S_{0i} (see chapter 4). The rotational levels of the molecule can not be resolved at room temperature. The Franck-Condon [92][93] principle gives the relative intensities of the transitions. These relative intensities of the vibrational lines in the spectra of PPO, pTP and bisMSB are compatible with the literature results [94]. The energy spacing between the ground state and the first excited triplet state is, in general, smaller than the one of the singlet state, i.e. at longer wavelengths. As above $\sim 500\,\mathrm{nm}$ no significant contribution appears, it can be concluded that there is no evidence for phosphorescence in the measured spectra. PMP displays an unstructured fluorescence spectrum which has also been reported in the literature [110].

Figure 7.6 shows PPO emission spectra of various concentrations of PPO in the
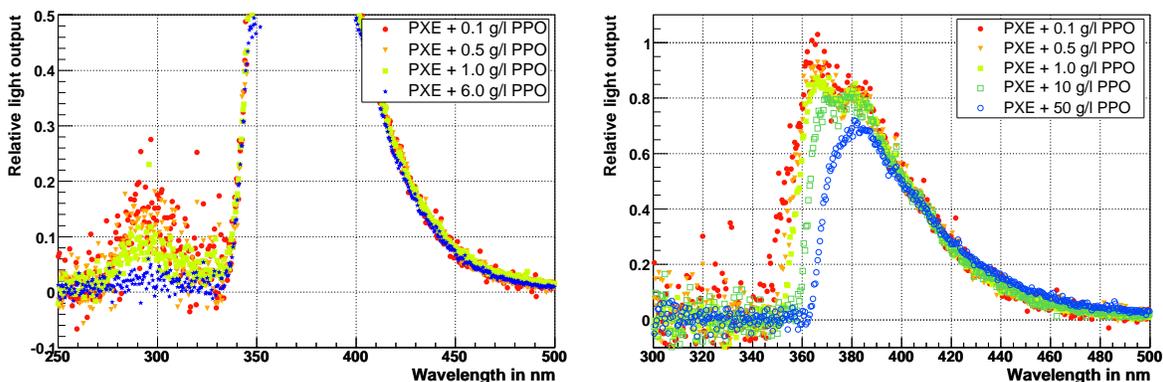
Figure 7.6: Spectra of mixtures based on PXE and PPO. Left: emission spectra where the variation of the PXE emission can be observed (position A, see figure 7.4). Right: evolution of the spectra with the concentration after $1.4\,\mathrm{cm}$ propagation (position B).

solvent PXE. In each figure only some distinctive examples are plotted. The complete
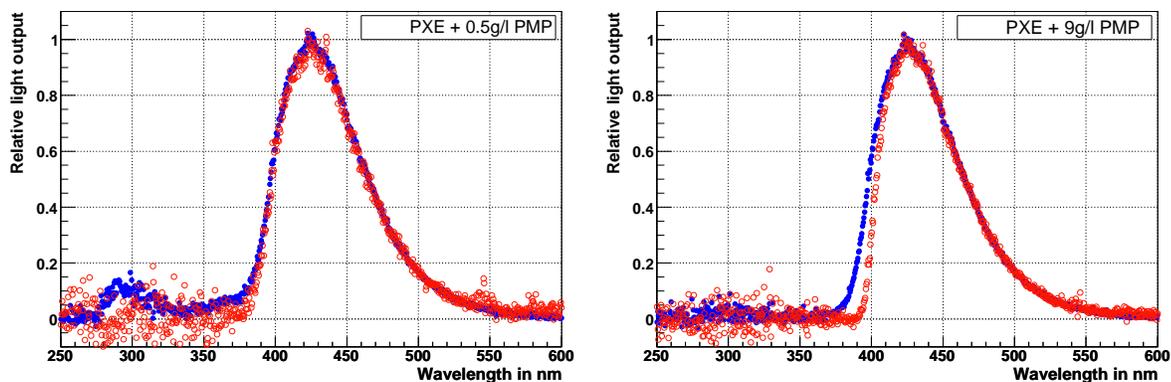
Figure 7.7: PXE solvent with 0.5 (left) and $9\,g/l$ PMP (right). It can be seen that the self-absorption of PMP is rather small. Further details as in figure 7.5.
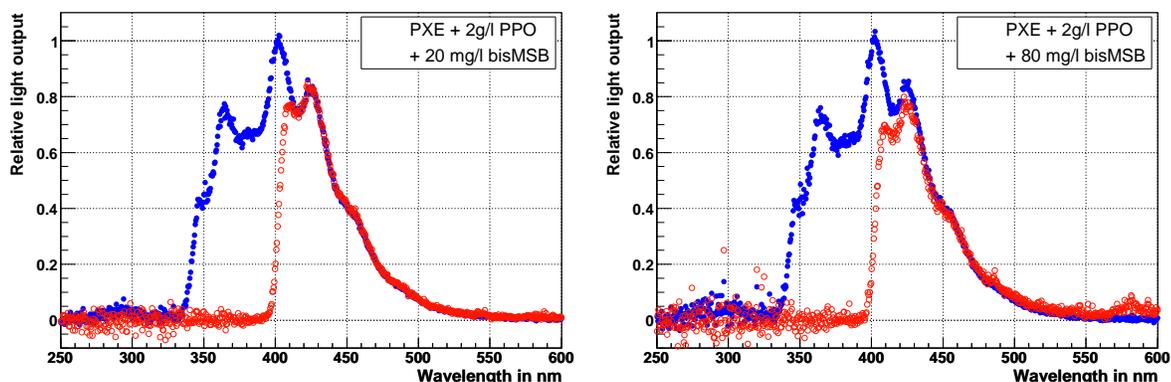
Figure 7.8: PXE solvent with $2\,g/l$ PPO and bisMSB is at 20 (left) and $80\,mg/l$ (right) concentration. Further details as in figure 7.5.

set of spectra can be found in the Appendix. On the left, a zoom into the emission region of PXE is shown (around 290 nm). The PXE peak is visible for low concentrations and disappears at higher concentrations as the excitation energy in PXE can be transferred completely to the solute. On the right, the complete PPO spectra are plotted for different concentrations. As the concentration increases, the shape of the transmitted spectrum (on position B) changes: the mean wavelength moves to larger values. This is a consequence of the self-absorption of the solute at short wavelengths.

The emission spectra of 0.5 and $9\,g/\ell$ PMP dissolved in PXE are presented in figure 7.7. Similar features as in the PXE-PPO system can be observed in the spectra. However, a significant difference is the low self-absorption of PMP. Even for a concentration of $9\,g/\ell$ only a small change in the spectrum B is observed. Figure 7.8 displays the emission spectra of mixtures of PXE and $2\,g/\ell$ PPO with an addition of 20 (left)

and 80 mg/ℓ bisMSB (right), respectively. When the UV-light from the deuterium lamp enters the scintillator, mostly PXE molecules are excited. Rapidly the energy is transferred to PPO mainly by nonradiative processes. Part of the energy in the PPO molecule is transferred further on to bisMSB molecules in the same manner (compare figure 7.8 and figure 7.5 top, left). As the concentration of bisMSB is low (in the order of several mg/ℓ), some of the PPO molecules find no bisMSB partner to transfer energy. As a consequence, the light is emitted by the PPO molecules themselves. After propagating a short distance, the light is absorbed very efficiently by bisMSB: although the concentration of bisMSB has been changed by a factor of four, the difference between both sets of spectra is figure 7.8 is small. In figure 7.9, the spectra of PXE with 2 g/ℓ PPO
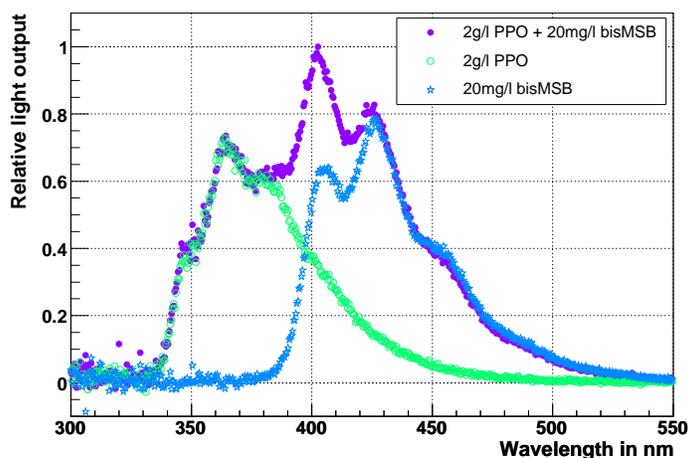
Figure 7.9: Zoom into the spectra of 2 g/ℓ PPO and 20mg/ℓ bisMSB (violet circles), 2 g/ℓ PPO (green empty circles) and 20mg/ℓ bisMSB (blue stars). All mixtures dissolved in the solvent PXE. The three-component scintillator shows the sum of the spectra of both solutes.

and 20mg/ℓ bisMSB (violet circles), PXE with 2 g/ℓ PPO (green empty circles) and PXE with 20mg/ℓ bisMSB (blue stars) are displayed together. The plot shows how the three-component spectrum (violet) results as the sum of the PPO and bisMSB spectra. Although the concentration of bisMSB is only 20 mg/ℓ bisMSB, its contribution to the sum spectrum is almost 50%. This illustrates the efficient energy transfer from PPO to bisMSB.

In figure 7.10, spectra of PPO dissolved in LAB are shown. In this case, the PPO concentration remains constant but the thickness of the scintillator container is varied from 1 cm to 2 cm. The corresponding propagation distances for the produced scintillation light are 1.4 (left plot) and 2.8 cm (right plot), respectively, due to the inclination of the light guide by an angle of 45° (see picture 7.4). A longer propagation distance
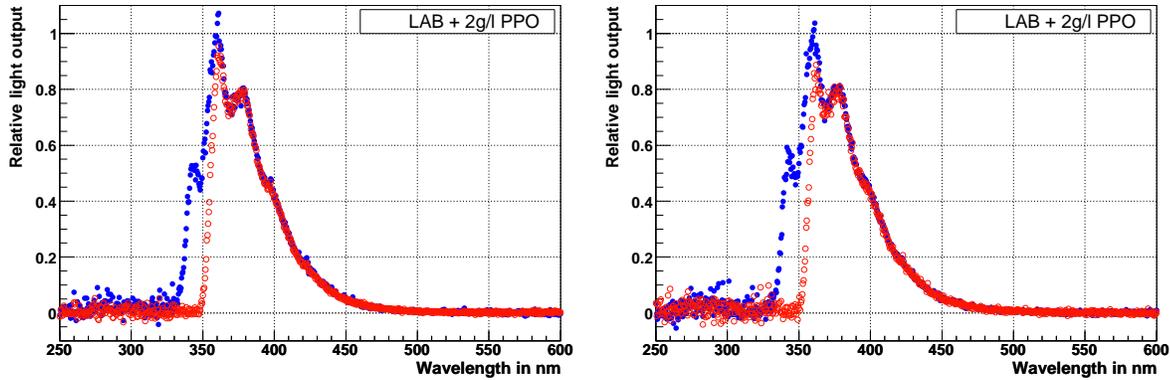
Figure 7.10: LAB solvent with $2\,\mathrm{g}/\ell$ PPO. Blue data points represent the direct emission spectrum. Red points in the left plot show the spectrum after $\sim 1.4\,\mathrm{cm}$ and in the right plot after $\sim 2.8\,\mathrm{cm}$ propagation through the sample.

through the sample effects the absorption similarly (see chapter 8) as an increase in the solute concentration. The difference in the propagation distances is however small leading to very similar spectra.

7.2.3   Study of the solute self-absorption

In the spectra shown in the previous section, an increase of the absorption at short wavelengths with the light propagation distance has been observed. Similarly to the solvent itself, the solute absorption spectrum partially overlaps with its emission spectrum. As a consequence, the short wavelengths are absorbed and reemitted into a solid angle of 4π. This leads to a loss in the number of photons detected in forward direction as the solid angle accepted by the light guide is small (its diameter is $600\,\mu\mathrm{m}$). In this section, the effect of solute self-absorption is studied. The extrapolation of this effect to a large experiment is discussed in chapter 8.

To investigate the wavelength dependence of the solute self-absorption, a systematic study has been carried out. Measurements of the direct emission and emission after propagation through x cm of scintillator with solute at concentrations varying over two orders of magnitude. As the self-absorption by the solute dominates at the wavelength region investigated [89], the absorption by the solvent can be neglected. This study has been carried out using the spectra of the sample mixtures shown in figures 7.6, 7.7 and 7.8 and covers two orders of magnitude in solute concentration.

In chapter 4, the intensity of light after a propagation distance x through liquid scintillator in one direction is considered. The absorption and the scattering processes can be neglected for the given experiment as the solute self-absorption dominates. The

84

intensity can therefore be written as:

$$I = I_0 \cdot e^{-\frac{x}{\lambda_{sa}(c)}}, \qquad \lambda_{sa}(c) = \lambda_{sa,0} \cdot \frac{c}{c_0} \qquad (7.1)$$

where I_0 is the intensity at the emission point, c the solute concentration in the measured mixture, c_0 is the reference concentration at which the self-absorption length is studied, λ_{sa} the self-absorption length for a given concentration, $\lambda_{sa,0}$ corresponds to $\lambda_{sa}(c = c_0)$ and x is the propagation distance. From this formula, λ_{sa} can be derived:

$$\lambda_{sa,0} = \frac{x \cdot c_0/c}{-\ln(I/I_0)}. \qquad (7.2)$$

For the evaluation of the results, expression 7.2 has been applied in the wavelength transition-region of each spectrum in position B between full absorption (at short wavelengths) and full transmission (at long wavelengths). The transition region changes with the solute concentration. For example, for PXE with PMP in the right plot of figure 7.7, the region ranges from 390 to 420 nm. When the solute concentration increases, the analysis region moves to longer values of the wavelength.

Figure 7.11 shows the results for the self-absorption $2\,g/\ell$ PMP and $2\,g/\ell$ PPO + $20\,mg/\ell$ bisMSB. length $(\lambda_{sa,0})$ for the following solutes and concentrations: $2\,g/\ell$ PPO, The self-absorption length for bisMSB is given for a PXE-PPO solvent mixture as this would be a more realistic approach for a large-scale detector. The peak values of the emission spectra of the measured samples are 365 nm for PPO, 415 nm for PMP and 420 nm for bisMSB (see figure 7.5). In all cases PXE solvent has been used, however, the influence of the solvent on the measurement is negligible (see chapter 8). Both statistic and systematic errors are included. The statistical error also includes the uncertainty of $\ln(I/I_0)$ due to the noise of the original data. This noise is either caused by scattered light or is thermal noise in the CCD camera. The systematic error is due to the uncertainties on the propagation distance x and the determination of the concentration c:

$$\Delta\lambda_{sys} = \lambda \cdot \left(\frac{\Delta x}{x} + \frac{\Delta c}{c} \right). \qquad (7.3)$$

This error which arises mainly from $\Delta x/x$ has been added linearly to the statistic one. A typical value for $\Delta c/c$ is 0.1. Within the error bars, the results shown in the upper left part of figure 7.11 for the self-absorption of $2\,g/\ell$ PPO in PXE are compatible with the values published in the literature [89].

As explained in section 7.2.1, the angle relative to the axis of the experiment at which the light guide is placed determines the propagation distance of the light through the liquid sample. During the measurement, this angle was set approximately at 45° but without measuring this angle precisely. However, the analysis of the data shows that this uncertainty contributes significantly to the systematic error. For an estimate of this
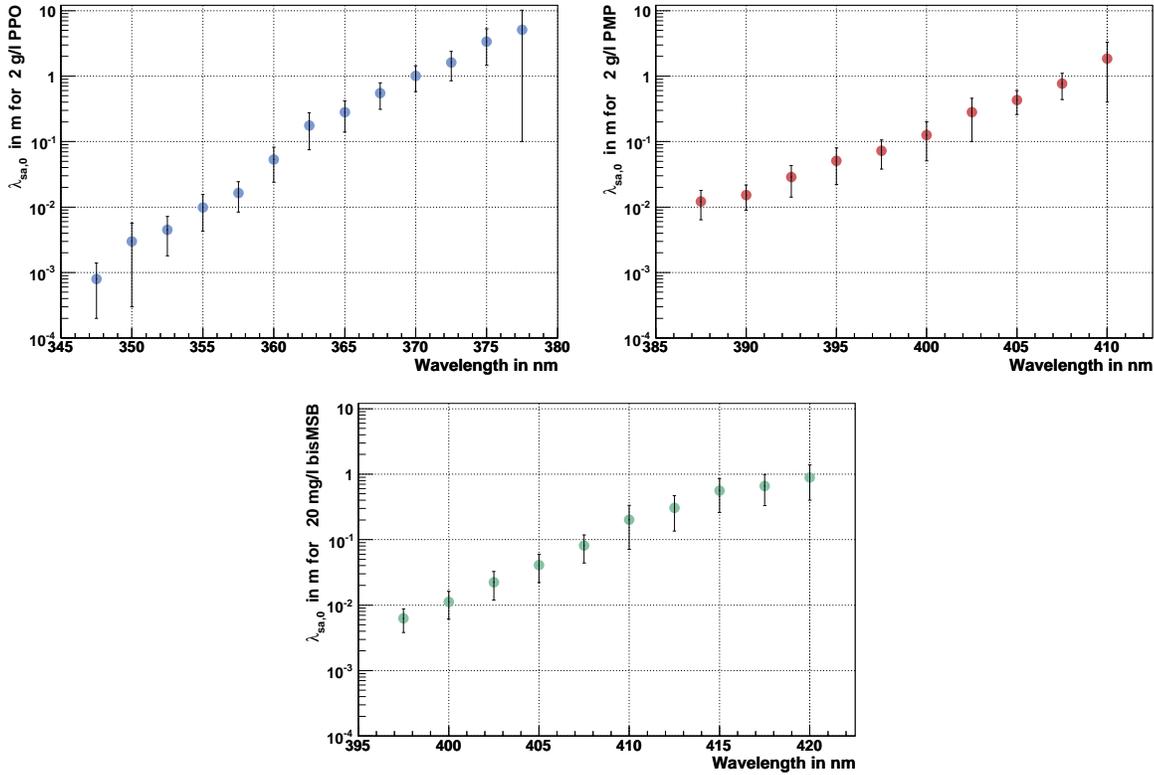
Figure 7.11: Self-absorption length $\lambda_{sa,0}$ of PPO, PMP and bisMSB solutes as a function of the wavelength. The first two solutes are dissolved in PXE while for the third PXE $+ 2\,\mathrm{g}/\ell$ PPO is used.

contribution, a series of measurements has been performed. The light guide has been adjusted in an approximate fashion as before several times and later it has been measured precisely. The systematic error estimated by this method is $\frac{\Delta x}{x} = 0.28$. Despite of this relatively large error, the precision indicated by the error bars in figure 7.11 is sufficient for the purpose of this thesis.

The solute self-absorption results in a longer effective fluorescence-time constant. To evaluate the importance of this effect, the fraction of the emitted light which is absorbed by the solute during the propagation has been estimated. To this end, the area below the scintillator spectra in position A from 250 to 600 nm has been calculated as reference. Next, the same area has been calculated but starting at the wavelength at which the intensity falls to $1/e$ after 1 cm, 1 m and 10 m. The values of the corresponding wavelengths are taken from figure 7.11. By dividing both areas the fraction of absorbed light is obtained. Table 7.1 summarizes the fraction of the intensity which is absorbed after 10 m, 1 m and 1 cm distance. The values of the self-absorption for 10 m in the case

Mixture	Distance	Fraction
2 g/ℓ PPO	1 cm	14%
	1 m	37%
	10 m	52%
2 g/ℓ PMP	1 cm	2%
	1 m	16%
	10 m	26%*
2 g/ℓ PPO + 20 mg/ℓ bisMSB	1 cm	45%
	1 m	65%
	10 m	78%*

Table 7.1: Estimate of the fraction of the emitted light which is absorbed by the solute for different propagation distances. (*These values have been extrapolated from figure 7.11 and can be affected by a large error, up to 50%.)

of 2 g/ℓ PMP and for 2 g/ℓ PPO + 20 mg/ℓ bisMSB are extrapolated from figure 7.11 assuming a linear behavior (in logarithmic scale). This assumption is not necessarily true leading to a large uncertainty in the extrapolated values. As expected, PMP has the lowest self-absorption length. The solvent used for the measurement was always PXE. In principle, spectral absorption depends on the solvent. However, the effect is small enough to be neglected in a good approximation (see chapter 8).

The solute self-absorption and reemission effect investigated here has consequences on the signal pulse-shape in a large detector. Several absorption and reemission processes result in longer decay-time constants. In chapter 8, an estimate of this effect for large propagation distances (about 10 m) is given.

7.3 Spectra obtained by excitation with an e⁻-source

When a particle detector is considered, the scintillator is excited by the energy deposition of charged particles. For this reason, the study of the emission spectra obtained by excitation of the scintillator via particle radiation is a more realistic approach than exciting the medium with UV-light. In this section, an experiment using low-energy electrons of about 10 keV is presented and the resulting spectra are shown.

7.3.1 Setup description

The radiation source used for this measurements was a compact (∼20 cm long) low-energy electron-beam device which is described in detail in [130][131]. This device is

housed in a glass-metal chamber which is kept at $5 \cdot 10^{-6}$ hPa vacuum. As indicated in figure 7.12, a heated tungsten filament is used to produce the electrons. Applying a DC voltage of 10-20 kV, the electrons are accelerated towards the exit window. Magnetic steering is used to guide the beam in x- and y- directions (perpendicular to the electron trajectories). On the other end of the device, the exit window is realized as a $300\,\mu$m thick silicon wafer with a $0.7 \times 0.7\,$mm^2 and $300\,$nm thick foil in the center. The foil is made of Si_3N_4 with a slight deviation from the exact stoichiometry to avoid material tensions. $20\,$keV electrons can pass through it, losing only about 8% of their energy [131]. The energy loss increases in such a membrane when the electron energy decreases (15% at $15\,$keV and 40% at $10\,$keV).

Figure 7.12 shows on the left a drawing of the experimental setup together with the electron source. On the right a picture of the setup is illustrated. The vertical metal
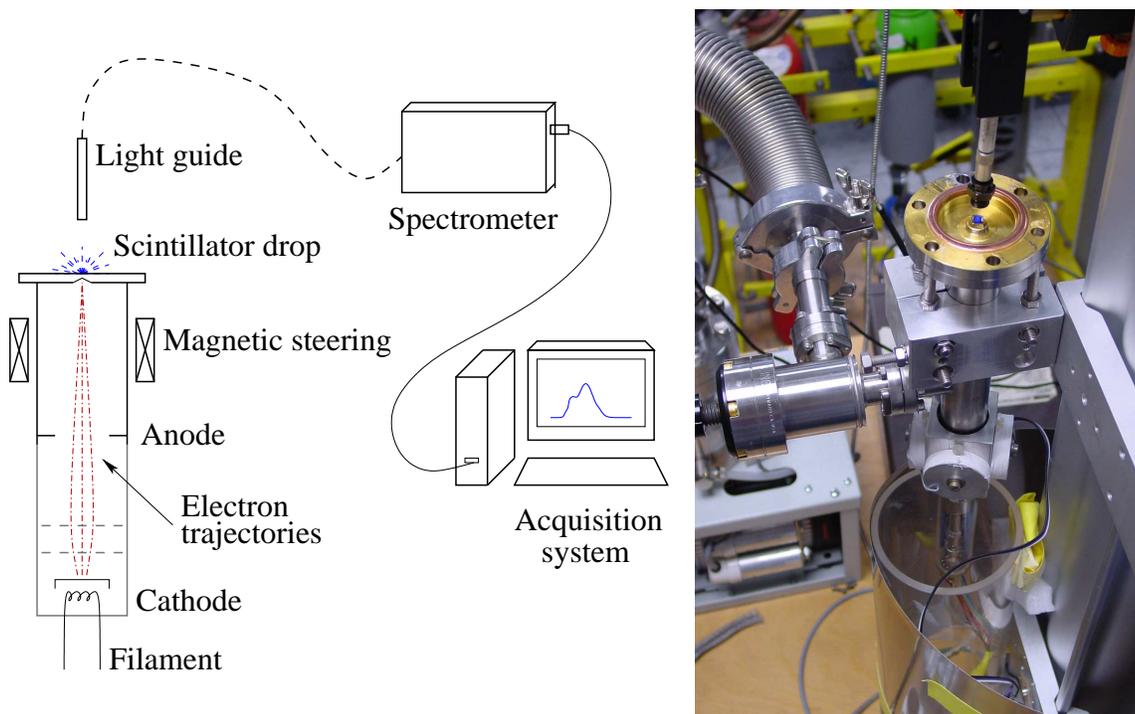
Figure 7.12: Setup for the spectral measurements of liquid scintillators when exciting the sample with $\sim$10 keV electrons.

structure is the electron accelerator which is connected to a vacuum pump (left part of the picture shows the pump line). On top, in the middle of a golden structure the exit window can be seen together with the sample to be investigated. As the picture was taken during a measurement, a blue light spot from the scintillating sample can be recognized.

The electron source was placed in vertical position leading to electrons which exit in

the upper direction. To observe the scintillation light, a drop of the liquid sample was deposited on top of the 300 nm thin Si$_3$N$_4$ window. The drop volume was not measured but it covered a surface of about 5 mm ×5 mm and it was about 1 mm in height. The end of the light guide was positioned about 1 cm above the window. The samples were taken from nitrogen-bubbled bottles and the measurements were performed immediately (within the next 10 min) to avoid oxygen diffusion into the sample, i.e. scintillator degradation. During the measurements, a decrease of the emitted light intensity with time was observed. However, there are two probable explanations for it. Either the scintillator drop evaporated with time or the intense e$^-$-radiation damaged the liquid by destroying σ-bonds (see chapter 4).

7.3.2   Data obtained with the e-beam excitation

The spectra of the samples measured by electron irradiation are presented in this section. As before, the resulting plots are normalized in intensity such that the highest intensity corresponds to 1. The spectrometer was calibrated as described in section 7.1.2.

The results of the mixtures measured with this method are shown in figure 7.13. Four samples were chosen for this measurement: PXE with 2 g/ℓ PPO, PXE with 2 g/ℓ PPO, and 20 mg/ℓ bisMSB, LAB (P550 Q) with 2 g/ℓ PPO and PXE with 2 g/ℓ PMP.

For mixtures of PPO with the solvents PXE and LAB, the shape of the spectrum is similar to those measured by UV-light excitation. The main difference arises from the absorption at short wavelengths due to the transmission through the scintillator drop. Moreover, in the spectra of PXE with PMP for the electron excitation method a small shift to longer wavelengths appears from 450 to 500 nm. However, in general it has been found that the spectral shape does not depend on the excitation method.

The spectrum of the mixture of PXE with 2 g/ℓ PPO and 20 mg/ℓ bisMSB shows very interesting features. Above 400 nm, the spectrum is similar to the one measured by the UV-light excitation method. Around 350 nm, the absorption at short wavelengths can be observed as in the previous cases. The most interesting region is between 350 and 400 nm as the contribution of PPO to the spectrum (see figure 7.9) is highly reduced. During the first μm to mm propagation distance (thickness of the scintillator drop), bisMSB absorbs very efficiently the light emitted by PPO. Consequently, the part of the spectrum by bisMSB is increased compared to the part of PPO. Unfortunately, the sample of PXE with 2 g/ℓ PPO and 20 mg/ℓ bisMSB belongs to a sample which was not mixed precisely. Probably, the concentration of PPO was higher than 2 g/ℓ, since the plots in figure 7.9 were prepared carefully and show a lower PPO contribution. For comparison a measurement with UV-light for the sample mixture has been taken. In conclusion, the differences between the spectral shapes from both excitation methods can be explained by the effect of the propagation of the light through the scintillator drop.
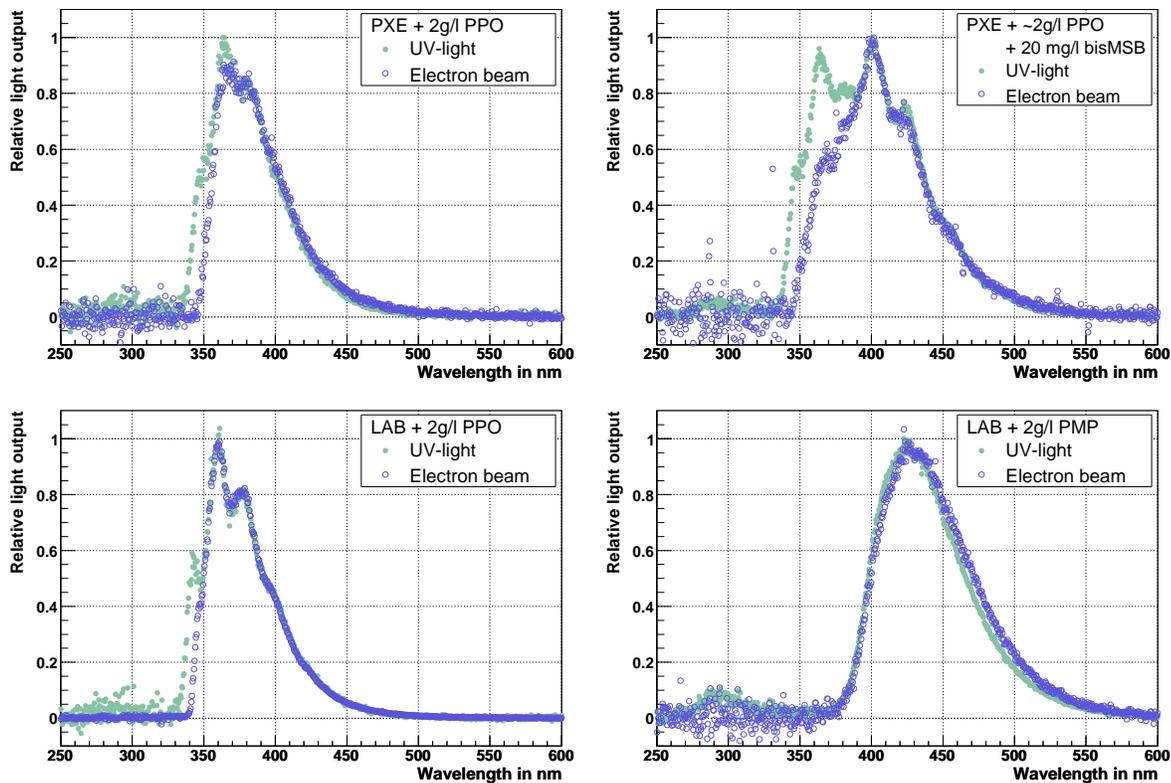
Figure 7.13: Spectra obtained with the electron-beam excitation method. The blue data points (empty circles) represent the emission spectra of different scintillator mixtures after the light has propagated through the drop. Samples: PXE + $2\,\mathrm{g}/\ell$ PPO + $20\,\mathrm{mg}/\ell$ bisMSB, LAB (P550 Q) + $2\,\mathrm{g}/\ell$ PPO, and PXE + $2\,\mathrm{g}/\ell$ PMP. The excitation is produced by ~10 keV electrons. For comparison, data from the UV-light excitation method is also plotted (green full circles).

For the calculation of the self-absorption lengths of the solutes, data from the method where excitation is performed by UV-light were used. Due to the similar spectra shown by both methods, it is guaranteed that the results of self-absorption lengths apply also when the scintillator is excited by charge particles.

Chapter 8

Discussion of the experimental results

In chapters 6 and 7, the experiments performed to measure the pulse shape and the spectra of several scintillator mixtures have been described and the results presented. This chapter contains the interpretation of the results by using the microscopic scintillation model which has been introduced in chapter 4. At the end, the results are summarized and conclusions concerning the liquid scintillator desirable for the proposed LENA detector are presented.

8.1 Fluorescence decay-time constants

The time evolution of the photon emission in several organic liquid-scintillator mixtures (probability density function, PDF) has been measured and the results are shown in chapter 6. The corresponding distributions have been fitted with a convolution of three or four exponential functions with a Gaussian function which represents the system's time-resolution. In this section, the origin of the fluorescence-decay constants is discussed considering the values obtained experimentally. The evolution of the shortest decay-time constant τ_1 with the solute concentration is also explained.

8.1.1 Origin of the decay-time constants

The shortest decay-time constant τ_1 has a value of several nanoseconds (2-9 ns) and represents the main contribution of the photon emission (its amplitude varies between 60 and 95% of the total emission). This contribution is usually interpreted [90] as the transition between the lowest excited state in the solute S_{1y} and its ground state S_{0y} (see chapter 4).

For the mixtures which have a convergent fit with four decay components, the second contribution (τ_2) could be related to absorption re-emission processes within the solute. The results of PXE-PMP mixtures support this explanation. Their fluorescence measurements indicate that the data can be described with three decay constants and spectroscopy measurements have shown the small self-absorption of PMP solute. A variation of this second decay constant and its amplitude with the solute concentration would be expected for the PXE-PPO system. However, it is not present as all τ_2's and N_2's are compatible within the errors.

The third and fourth components (second and third for mixtures fitted with three components) correspond to additional molecular processes and cannot be easily disentangled. A possible explanation for these longer components is the delayed light emission due to the existence of triplet states in the solvent as explained in section 4.2. Solvent molecules excited in triplet states have a different energy gap to the ground state and for this reason the energy can not be efficiently transferred to the solute. The energy remains in this states until thermal energy is acquired allowing for the spin-flip reaction $T_1 \rightarrow S_1$ or until the reaction $T_1 + T_1 \rightarrow S_1 + S_0$ takes place. The S_{1x} state can then, as usual, transfer its energy to the solute and delayed light-emission appears. If none of the mentioned reactions take place, the excitation energy remains at T_1 and light can be emitted via $T_1 \rightarrow S_0$. This transition is highly forbidden by selection rules and its lifetime is long (for example the phosphorescence lifetime of *benzene* solvent is 16 s [94]). In the experiment, the photon is lost most of the times as the photon-emission time is longer than a typical signal length (in the order of microseconds).

In addition, the formation of *dimeric* molecules has been reported in the literature [90] and could contribute to the multi-exponential decay. Dimeric states are formed when an excited molecule builds a metastable state with a molecule in the ground state:

$$S_1 + S_0 \rightarrow D^*, \quad D^* \rightarrow S_0 + S_0 + photon. \tag{8.1}$$
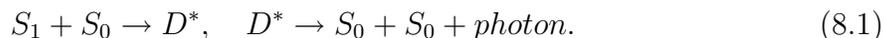
In principle, both solvent and solute can form dimeric states. However, the probability is higher for the solvent as its molecules are close to each other. For dimeric states in the solute, the wavelength of the peak value of the emission spectrum is within the singlet emission spectrum. For example, for PPO the peak of the dimeric emission takes place at 445 nm [90] and the intensity of its singlet state emission is between 335 and 445 nm above 10% of its peak intensity. The dimer intensity is in general small and it is difficult to measure its contribution in an emission spectrum. In addition, the dimer spectrum has no structure because the ground state potential between the two molecules, which have formed the dimer, is repulsive [94]. Furthermore, organic impurities can absorb the emitted light and reemit it with a longer time-constant accounting for a further decay-time contribution. Finally, although electron recombination is a slow process in organic liquids, a small number of photons could arise from this process [90].

In the measurement of the non-scintillating oil dodecan with PPO wavelength-shifter,

a long component with a tiny amplitude (0.6%) appears. This amplitude is about one order of magnitude smaller than in measurements where a scintillating solvent has been used. This indicates that the longer decay constant (τ_3 or τ_4 depending on the fit) could be a solvent-related process.

8.1.2 Evolution of τ_1 with the concentration

For three scintillator systems (PXE-PPO, LAB-PPO and PXE-PMP), the evolution of the shortest time emission τ_1 with the solute concentration c has been studied. By considering the variation of this decay-time constant, information on the energy transfer in the different systems can be obtained. This decay constant is, as mentioned before, related to the transition $S_{1y} \rightarrow S_{0y}$. However, in the measurements described in chapter 6, the intrinsic value of the S_{1y} lifetime has not been measured separately, because additional molecular processes are involved. After the energy deposition by a charged particle, the solvent molecule remains in the first excited state S_{1x}. Via collisions with neighboring solvent molecules, the excitation energy can propagate between solvent molecules with a rate k_{txx} in s^{-1} (see chapter 4). This process is also known as *energy hopping* [95]. The excitation energy moves spatially until a solute molecule is close enough to get the energy transferred by dipole-dipole interaction (process k_{txy}) [97]. The measured decay-constant τ_1 is mainly the sum of the energy-hopping time $\tau_{txx}(c) = \frac{1}{n(c) \cdot k_{txx}}$ and the intrinsic lifetime of the solute τ_s. The number of solvent-solvent collision processes n depends on the solute concentration, the higher the concentration the lower n.

Taking a linear dependence of the transfer rate on the concentration [99][100] and defining an effective hopping rate k_h, it follows that: $n(c) \cdot k_{txx} = k_h \cdot c$ and the measured τ_1 decay constant can be written as:

$$\tau_1(c) = \tau_s + \tau_{txx}(c) \qquad \tau_1(c) = \tau_s + \frac{1}{k_h \cdot c}. \tag{8.2}$$

By fitting this quite simple formula to the experimental data, the intrinsic lifetime of the solute τ_s can be extracted. Moreover, the value of k_h represents the efficiency of the energy transfer via collisions (hopping) between solvent molecules.

Figure 8.1 shows the evolution of τ_1 with the PPO concentration when it is dissolved in the solvents PXE (upper left) and LAB (upper right). The lower panel shows the concentration dependence for the PMP solute dissolved in PXE. The errors assigned to the data points are the sum of the statistic and systematic uncertainties and are explained in section 6.5.3. The fit applied to the data points corresponds to equation 8.2. For each plot, the right upper-box shows the fit results where the parameter τ_s is labeled with the name of the solute and k_h with the name of the solvent. The fit takes into account both the uncertainties in the solute concentrations and the errors on the decay-time constants, the latter errors being asymmetric (see chapter 6).

93
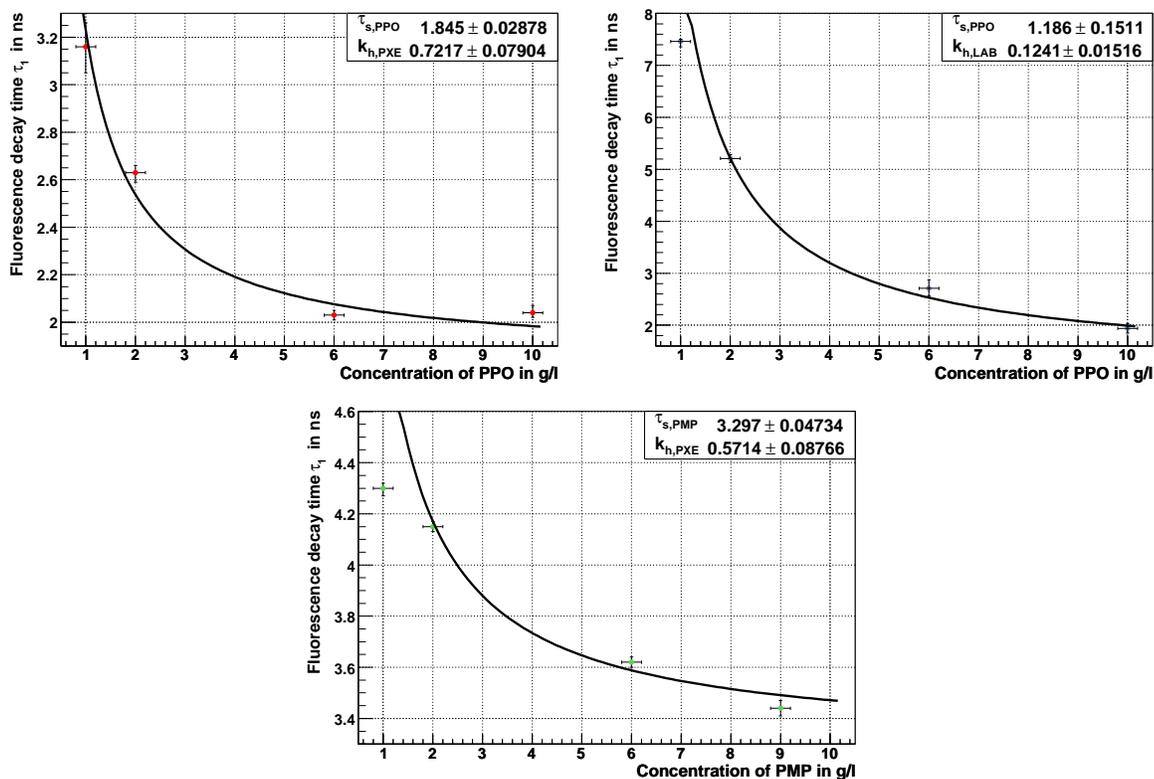
Figure 8.1: Upper part: evolution of the fluorescence decay time τ_1 for different concentrations of PPO in the solvents PXE (left) and LAB (right). Bottom: evolution of τ_1 for different concentrations of PMP in PXE.

From the fits, the intrinsic lifetime of the PPO singlet-state S_1 can be extracted. For the PXE-PPO mixtures $\tau_{s,\text{PPO}} = 1.85 \pm 0.03$ is obtained and $\tau_{s,\text{PPO}} = 1.2 \pm 0.2$ for the mixtures of LAB-PPO. Thus, the obtained value for τ_s is lower when the LAB solvent is used. The relative uncertainties on these parameters are ~ 1.6 and 17%, respectively. Obviously, the uncertainty for the mixture with LAB is much larger. It is important to keep in mind that the values for τ_1 in LAB arise from a three-component fit to the PDF for the two lower concentrations and a four-component fit for the higher concentrations. In the literature, the value for the intrinsic lifetime of the S_1 state in PPO varies slightly. In [94] the values 1.44 and 1.8 ns are reported. They result from different theoretical calculations of the $S_1 \rightarrow S_0$ transition and include a factor which takes the index of refraction of the solvent medium into account (cyclohexane in the published cases). A discussion of the solvent influence on τ_s can be found in section 8.2.2. Finally, in [89] the value 1.6 ns is used. The agreement with the results presented here for τ_1 is very convincing.

The parameter k_h quantifies, as explained before, the transfer of energy between solvent molecules via collisions. This transfer rate is faster for PXE than for LAB which explains why for low PPO concentrations the measured τ_1 values are much shorter than those for PPO dissolved in LAB. As an example for a concentration of $2\,\mathrm{g}/\ell$ PPO, $\tau_{txx,\mathrm{PXE}} = 0.69\,\mathrm{ns}$ and $\tau_{txx,\mathrm{LAB}} = 4.03\,\mathrm{ns}$ (see equation 8.2). This effect could be related to the structure of the LAB molecule (see chapter 5) as the long hydrocarbon-chain might disturb the energy transfer between benzene rings.

The obtained value for the intrinsic lifetime of PMP, $\tau_{s,\mathrm{PMP}} = 3.30 \pm 0.05\,\mathrm{ns}$ is close to the measured value of $3.01\,\mathrm{ns}$ given in reference [110]. $\tau_{s,\mathrm{PMP}}$ is significantly larger than the intrinsic lifetime of PPO. The value of $k_{h,\mathrm{PXE}}$ from this fit is compatible within the error bars to the one measured with the PXE-PPO system ($k_{h,\mathrm{PXE}} = 0.57 \pm 0.09$ when PMP is used and $k_{h,\mathrm{PXE}} = 0.72 \pm 0.08$ for the mixture with PPO).

8.1.3 Efficiency of the solvent-solute energy transfer

As described in chapter 4, the energy transfer between a solvent and a solute molecule (k_{txy} [90]) takes place via dipole-dipole interactions and depends mainly on the overlap between the solvent emission-spectrum and the solute absorption-spectrum [97]. This transfer has an influence on the scintillator light yield as for a high spectral overlap the energy losses decrease. The solvent is responsible for the conversion of the deposited energy into quantified excited states which can lead to photons. However, the transfer processes between solvent and solute can lead to further energy losses. The dipole-dipole energy transfer is a resonance effect and therefore, the better the spectra overlap the less the probability to loose energy thermally. The decay-time constant τ_1 should, in principle, not be affected by this overlap because the energy transfer happens immediately when the excited solvent molecule is close enough ($r < R_0$ in equation 4.2) to the solute molecule. However, the amplitude N_1 could be affected by the solvent-solute energy transfer since the more efficient the energy transfer the larger the intensity of the $S_1 \rightarrow S_0$ transition. The excitation energy doesn't remain within long-lived states of the solvent but is emitted by the solute in the form of photons.

In the tables 6.2 and 6.3, the relative light outputs between different solvents, solutes and solute concentrations have been presented. For a given solvent (for example PXE) and a fixed solute concentration (e.g., $2\,\mathrm{g}/\ell$), significant differences have been observed between the light output of different solutes. While PPO emits a large number of photons, for bisMSB the number of detected photons is strongly reduced. This reflects the fact that the overlap between PXE and PPO spectra is larger than for PXE and bisMSB. When the solute type and concentration remains the same but the solvent is varied, the change on the light output contains information on both the efficiency of the solvent to convert deposited energy into excited states and on the energy transfer to the solute.

Also a variation of the light output with the solute concentration has been observed. For low solute concentrations (typically $< 5 - 10\,\mathrm{g}/\ell$, depending on the solute), the light output decreases with decreasing concentration. As already mentioned, after the energy deposition, the excitation energy hops from solvent to solvent molecule. For concentrations up to $\sim 5\,\mathrm{g}/\ell$, the excitation energy can be trapped into a triplet state (T_{1x}) resulting eventually in a loss of the photon because of possible deexcitation via collisions. A photon in the S_{1x} state can be lost when the lifetime of the level is too large (up to several seconds) compared to the recorded time interval for a signal (in the order of μs). Until a certain limit, an increase of the solute concentration leads to an increase in the light yield (see figure 6.11). However, for very large concentrations photon losses can become more important (usually called concentration quenching [90]): Multiple photon absorption and reemission processes of the solute can result in a quenching transition ($S_{1y} \rightarrow S_{0y}$ without photon emission) or in an energy release in the form of phonons. In addition, if the solute concentration is high, solute molecules are closer to each other and the probability for dimeric formation increases. The formation of a dimeric state doesn't imply the loss of a photon, but it is emitted eventually with a longer decay-time and can be lost because a recorded time-interval has a limited length. This concentration quenching effect has been observed for the PPO solute in both PXE and LAB. For the PMP solute, within the range of concentrations investigated, the light output increases continuously (see figure 6.11). Thus in this case, the maximum light output could be reached at still larger solute concentrations than those investigated in this thesis.

8.2   Spectroscopy of organic liquids

In chapter 7, spectra of several scintillator samples have been shown. For most of the solutes, the vibrational structure of the solute molecule could be resolved. The effect of solute absorption-reemission has also been studied by changing the solute concentration. In this section, the influence of absorption-reemission processes on the fluorescence decay-constant τ_1 is discussed. In addition, the effect of the solvent type on the fluorescence-emission process is briefly described.

8.2.1   Effect of absorption-reemission processes on τ_1

The measurements of the fluorescence decay-time constants have been performed for a small volume of $\sim 10\,\mathrm{ml}$, where the maximum light propagation distance is $2\,\mathrm{cm}$ (approximately $1\,\mathrm{cm}$ mean propagation distance). In a large detector like LENA, the emitted light propagates over several meters (about $10\,\mathrm{m}$) and therefore solute absorption-reemission processes play a major role. In this section, a very simplified calculation has been performed in order to estimate the effect of solute absorption-reemission pro-

Mixture	$\tau_{1,1cm}$	F_{10m}	F_{1cm}	τ_s	$\tau_{1,10m}$
PXE + 2 g/ℓ PPO	2.61 ns	52%	14%	1.85 ns	3.3 ns
PXE + 2 g/ℓ PMP	4.15 ns	26%	2%	3.30 ns	4.9 ns
PXE + 2 g/ℓ PPO + 20 mg/ℓ bisMSB	2.63 ns	78%	45%	1.24 ns [94]	3.0 ns

Table 8.1: Summary of parameters connected to solute self-absorption and reemission used to estimate the increase of τ_1 after light propagation of 10 m in a large detector (for further details see text).

cesses on the main decay-time constant τ_1. The goal is to investigate the effect of self-absorption of different solutes for the case of a large liquid-scintillator detector.

As a starting point, the value of τ_1 as measured in the laboratory for a certain scintillator mixture is used (see section 6.6). It is assumed that the mean distance for the light propagation in this experiment is 1 cm. In chapter 7, the solute self-absorption lengths have been calculated for three scintillator mixtures which are summarized in figure 7.11. In table 7.1, the fraction of light which is absorbed (the intensity decreases as $1/e$) after a certain distance has been calculated as well. With these results, the fraction (in %) of light absorbed after 1 cm (F_{1cm}) can be estimated and also the fraction after 10 m (F_{10m}) which is a typical propagation distance in the LENA detector.

When a photon is absorbed by a solute molecule, it can be reemitted only with a longer wavelength than the initial one (lower energy). For the calculation, it is assumed that each photon is absorbed and reemitted only once. Actually, the absorbed photons are reemitted within a 4π solid angle, but the longer light propagation path is not considered in this approximation. The effective shortest decay-time after 10 m propagation distance ($\tau_{1,10m}$) can be then written as the sum of the decay-time measured in the laboratory after 1 cm propagation ($\tau_{1,1cm}$) and the effect of the propagation from 1 cm to 10 m. Here, only solute self-absorption is considered in the propagation. The time increase corresponding to this propagation can be described as the fraction of light absorbed and reemitted between 1 cm and 10 m multiplied by the intrinsic lifetime of the solute:

$$\tau_{1,10m} = \tau_{1,1cm} + (F_{10m} - F_{1cm}) \cdot \tau_s. \tag{8.3}$$

Taking the values of $\tau_{1,1cm}$ from section 6.6, the fractions F_{1cm} and F_{10m} from table 7.1, the measured values of τ_s for PPO and PMP and the literature value for bisMSB of $\tau_{s,\text{bisMSB}} = 1.24$ ns [94], the effective value of τ_1 after 10 m propagation can be estimated. Table 8.1 summarizes the results for three mixtures: PXE + 2 g/ℓ PPO, PXE + 2 g/ℓ PMP and PXE + 2 g/ℓ PPO + 20 mg/ℓ bisMSB. The solute self-absorption and reemission process increases $\tau_{1,1cm}$ by 26, 18 and 14%, respectively. For PXE + 2 g/ℓ PPO, both with or without bisMSB, the resulting decay-time constant $\tau_{1,10m}$ remains quite fast and acceptable for a large detector. For PMP the effect of the propagation is not

97

very large due to the low self-absorption, but the decay time $\tau_{1,10m}$ is significantly larger than for PPO. For a large experiment, a higher PMP concentration could be used.

It is emphasized that all estimations are affected by several uncertainties. The dominating contribution is due to the uncertainty in the fraction F_{10m} (up to 50%). In addition, the calculation assumes a negligible scattering length which, of course, contributes significantly to $\tau_{1,10m}$. The model also does not properly take into account the 3-dimensional aspect. To have a realistic value of $\tau_{1,10m}$, a full simulation including an optical model where the underlying scintillation-processes are considered has to be performed. To this end, the fluorescence decay-time and solute self-absorption lengths measured in this thesis can be used. In addition, a wavelength-dependent measurement of scattering and absorption lengths is essential.

8.2.2   Dependence of the fluorescence spectra on the solvent

The emission spectra of the solute PPO have been measured when it is dissolved in the solvents PXE and LAB. Figure 8.2 shows a comparison of both spectra, exhibiting two
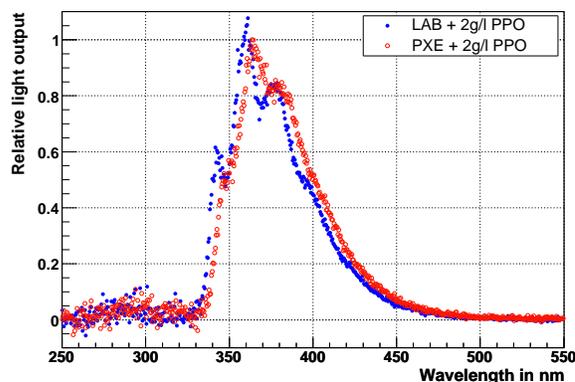
Figure 8.2: Comparison of the PPO spectra for the solvents LAB and PXE. With PXE as solvent, a shift of about 10 nm to longer wavelengths can be observed and a more smeared-out vibrational level structure.

interesting features. First of all, a shift of about 10 nm on all the PPO vibrational peaks is observed. Furthermore, the resolution of the vibrational levels varies: the peaks in the mixture with LAB are better resolved. These effects could be explained by considering the structure of the solvent molecules. The surroundings of the benzene rings produce a mean potential, which changes the orbital spacing of the π-bonds. A consequence of this could be the difference in the emission of the solvents PXE and LAB, namely 290 and 283 nm respectively [105][108]. PXE consists of two benzene rings and CH_3 groups while LAB has only one benzene ring and a long hydrocarbon-chain (see table 5.1 in

chapter 5). The solute also feels an effective potential which might result in a different emission spectrum.

Similar effects have already been observed and are reported in the literature [94]. A dependence of the position and structure of the fluorescence spectrum on the solvent has been found. The wavelength displacement can be correlated with a change in the dielectric constant of the solvent and therefore in its index of refraction. For example, if the solvent is polar [94], the sharpness of the vibrational level structure is lost and the spectra are shifted towards longer wavelengths. Moreover, it has been reported that the emission is more shifted than the absorption spectrum, leading to a larger Stokes shift. In such cases, even the intrinsic lifetime of the S_1 solute-state can increase. In general, the solvent-solute interaction is not fully understood but several mechanisms have been proposed ([94] and references therein). These are hydrogen bonding, electromagnetic interaction between the dipole moment of the solute and that of the polar solvent, and the reorientation of the solvent molecules.

Summarizing all experimental results, the spectra of PPO in the solvent PXE is $\sim 10\,\mathrm{nm}$ shifted to longer wavelengths, the vibrational structure is no longer highly resolved and the intrinsic lifetime obtained in section 8.1.2 is slightly longer than in LAB. The refractive index of PXE, $n_{\mathrm{PXE}} = 1.565$ is as well larger than that of LAB, $n_{\mathrm{LAB}} = 1.484$. In addition, it is known, that the PPO molecule is polar [132], supporting the possibility of different interactions with the solvent. The results of the measurements performed in this thesis are compatible with the description in the literature [94].

8.3 A liquid scintillator for the LENA detector

In chapter 3, the optical properties of the liquid scintillator required by the physics goals of LENA have been summarized. One of the most important parameter is the photo-electron yield which refers to the number of produced photo-electrons in the photomultiplier cathodes per unit deposited energy. This parameter directly influences the energy resolution and the energy threshold of the detector. The conditions to achieve a large photo-electron yield are a good conversion of the deposited energy into photons, an efficient energy transfer between solvent and solute molecules, and a transparent scintillator, i.e. a large attenuation-length ($\sim 10\,\mathrm{m}$). In addition, a scintillator which produces short pulses is desired to achieve a good position reconstruction and to be able to separate timely close pulses. To this end, a short lifetime of the excited states of the molecules and long scattering and self-absorption lengths are required.

In the presented work, some of these parameters have been investigated. Combining the results with the existing knowledge on scattering lengths and absorption lengths [133][134][105], some favored scintillator candidates for LENA can be discussed. LAB has shown a high transparency [134] and high light-yield. However, due to its low

99

efficiency to transfer energy between its own molecules, a high solute concentration has to be used. In this case, PMP is the only solute (from the investigated ones) which can be used at large concentrations with a reasonable self-absorption in a large detector. That means, if LAB is used it should be in combination with about $10\,\mathrm{g}/\ell$ PMP. PXE hasn't the good transparency of LAB but after purification satisfactory values can be achieved (about $10\,\mathrm{m}$ attenuation length [105]). As the energy transfer between PXE molecules is fast, several solute possibilities can be considered. PMP can be used as well at 6-10 g/ℓ but also a mixture with $2\,\mathrm{g}/\ell$ PPO and maybe also $20\,\mathrm{mg/l}$ bisMSB. As mentioned before, all parameters should be included in a full Monte Carlo simulation, however, concerning the timing (i.e., signal pulse-shape) mixtures including PXE and PPO are recommended because their first decay-time constant τ_1 is short and its amplitude N_1 is large. Finally, if dodecan is considered in the mixture to increase the number of free protons, it is certain that it influences the timing and the light yield in a negative way.

A further requirement for a liquid scintillator is the α/β-discrimination capability (see chapter 4). In the *Counting Test Facility* [105], the α/β-discrimination of PXE has been shown. This has to be prove as well for LAB. In this thesis, it has been assumed that the particle discrimination mainly depends on the solvent since the mechanism which produces a different pulse-shape can be explained by the combination of solvent T_1-states (see equation 4.1 in chapter 4). However, it would be of great interest to investigate the question whether the discrimination varies with the solute type.

Chapter 9

Sensitivity of the LENA detector to proton decay

One of the main aims of the future LENA detector is the search for proton decay, which is an important prediction of all Grand Unified Theories (GUT). Further physics goals are summarized in chapter 2. In the present chapter the simulation and analysis of the search for proton decay in a large liquid-scintillator detector is presented. After a brief description of the current theoretical and experimental situation, detailed information on the topology of the proton-decay reaction $p \rightarrow K^+ + \overline{\nu}$ in LENA is given. For this decay channel the sensitivity of LENA has been calculated. In addition, the variation of the detection sensitivity with the optical properties of the medium has been investigated. First studies concerning the proton-decay channel $p \rightarrow e^+ + \pi^0$ are also introduced and ideas to achieve a good background rejection for this channel are presented. At the end, a summary of other possible nucleon-decay channels and the potential of a liquid-scintillator detector to search for them is briefly described.

9.1 Theoretical predictions

In the standard model of particle physics, protons are stable. This is a consequence of the baryon number (B) conservation which has actually been introduced empirically into the model. It is interesting to realize that there is no fundamental gauge symmetry which generates the conservation of B. For this reason, the validity of B-conservation can be considered as an experimental question. This section is a very brief description of some of the first theories beyond the standard model which actually predicts baryon number violation: $SU(5)$, $SO(10)$ and Supersymmetry. Reviews of theories predicting nucleon decay can be found in [30][135].

9.1.1   Introduction to Grand Unified Theories

In a large range of energies, the standard model of particle physics, $SU(3) \times SU(2) \times U(1)$, correctly describes the elementary particle interactions. However, it is desirable to have a more unified theory with a set of transformations G which can combine all known interactions except gravity:

$$G \supset SU(3) \times SU(2) \times U(1). \tag{9.1}$$

This is the underlying idea of all GUTs where weak, electromagnetic and strong interaction with gauge couplings g, g' and α_S, belong to a larger gauge group with a single coupling constant g_{GUT}. The different gauge symmetries and coupling constants of the standard model are considered to be the result of spontaneous symmetry-breaking of the GUT symmetry at the scale M_X. Because of the large differences in the coupling strengths, this unification can not appear until the energy scale of $M_X \sim 10^{14}$ GeV is reached.

In these theories, leptons and quarks are often placed in the same multiplets allowing for baryon number violating processes. Therefore, proton decay is one of the most dramatic predictions of GUTs and its detection would strongly point towards a unification model.

9.1.2 $SU(5)$

Georgi and Glashow [24] proposed in 1974 that, for the presently known quarks and leptons, the simplest unification gauge group of color and flavor is $SU(5)$. These particles are accommodated in a fundamental $\overline{5}$ and 10 representation:

$$\overline{5} = (1,2) + (\overline{3},1) \tag{9.2}$$

$$10 = (1,1) + (\overline{3},1) + (3,2). \tag{9.3}$$

If it is written explicitly for left handed states:

$$\psi_{\overline{5}L} = \begin{pmatrix} d_1^c \\ d_2^c \\ d_3^c \\ e^- \\ -\nu_e \end{pmatrix}_L \qquad \psi_{10L} = \frac{1}{\sqrt{2}} \begin{pmatrix} 0 & u_3^c & -u_2^c & -u_1 & -d_1 \\ -u_3^c & 0 & u_1^c & -u_2 & -d_2 \\ u_2^c & -u_1^c & 0 & -u_3 & -d_3 \\ u_1 & u_2 & u_3 & 0 & -e^+ \\ d_1 & d_2 & d_3 & e^+ & 0 \end{pmatrix}_L \tag{9.4}$$

the gauge bosons of $SU(5)$ are $5^2 - 1 = 24$:

$$24 = (8,1) + (1,3) + (1,1) + (3,2) + (\overline{3},2) \tag{9.5}$$

and the gauge-boson matrix A can be written as:

$$A = \begin{pmatrix} G_1^1 - \frac{2B}{\sqrt{30}} & G_2^1 & G_3^1 & \overline{X^1} & \overline{Y^1} \\ G_1^2 & G_2^2 - \frac{2B}{\sqrt{30}} & G_3^2 & \overline{X^2} & \overline{Y^2} \\ G_1^3 & G_2^3 & G_3^3 - \frac{2B}{\sqrt{30}} & \overline{X^3} & \overline{Y^3} \\ X_1 & X_2 & X_3 & \frac{W^3}{\sqrt{2}} + \frac{3B}{\sqrt{30}} & W^+ \\ Y_1 & Y_2 & Y_3 & W^- & -\frac{W^3}{\sqrt{2}} + \frac{3B}{\sqrt{30}} \end{pmatrix} \tag{9.6}$$

where G_β^α are the $SU(3)_c$ gluons, $W^\pm$, B the gauge bosons of the standard electroweak model, and X, Y are 12 new gauge bosons. The bosons X and Y are vector particles, have color and flavor, carry fractional charges:

$$Q_X = 4/3 \quad \text{and} \quad Q_Y = 1/3 \tag{9.7}$$

and have masses in the order of the grand unification scale of $\sim 10^{14}\,\text{GeV}/c^2$. Since the photon is a $SU(5)$ gauge boson, the charge operator Q is a generator of the group [27]. Therefore the trace of each generator vanishes for any representation, $\text{Tr}\,Q = 0$, and the sum of the electrical charges in each multiplet is 0. For example, for the $\bar{5}$ representation:

$$\text{Tr}\,Q = Q_{d^c} + Q_{d^c} + Q_{d^c} + Q_\nu + Q_{e^-} = 0, \qquad Q_{e^-} = -3 \cdot Q_{d^c} \tag{9.8}$$

and the factor 3 appears from the number of colors. This result nicely explains the quantification of the electrical charge.

The X and Y bosons connect quarks and leptons and can therefore mediate proton-decay processes. In figure 9.1, possible Feynman diagrams [135] for proton decay with X, Y boson mediation are shown representing the favored decay mode in GUT based on a
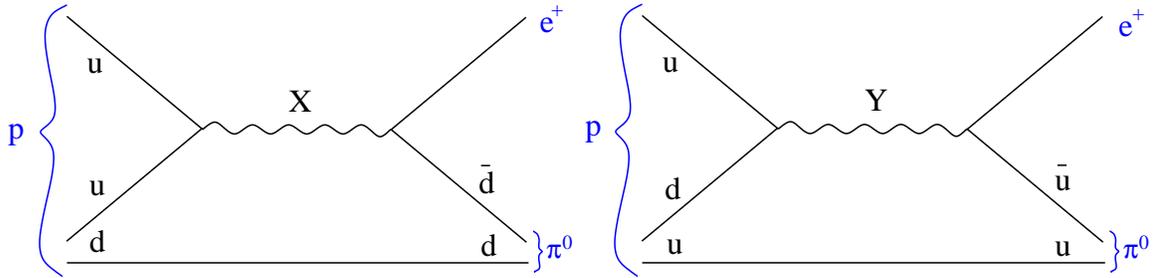
Figure 9.1: Possible Feynman diagrams for the $SU(5)$ favored proton-decay channel $p \to e^+\pi^0$ with the mediation of super-heavy X and Y bosons [135].

$SU(5)$ symmetry (minimal $SU(5)$), $p \to e^+\pi^0$. For this decay, the proton lifetime scales $\sim M_x^4$, where M_x is the mass of the X boson. In minimal $SU(5)$, $M_x \sim 10^{15}\,\text{GeV}/c^2$, yielding a predicted lifetime of $\tau(p \to e^+\pi^0) = 10^{29}$ years. The first generation of large

water-Cherenkov detectors motivated by this prediction, observed no evidence of proton decay in the $p \rightarrow e^+ \pi^0$ mode and therefore ruled out the model. The lifetime of the proton largely depends on the mass scale of the super-heavy particles mediating the process (X and Y bosons). Further extensions of the $SU(5)$ model predict a longer proton-decay lifetime with a larger uncertainty, typically from 10^{30} to 10^{36} years [136].

9.1.3 $SO(10)$

A famous possibility to extent the $SU(5)$ model is to use a larger group by introducing the $SO(10)$ symmetry [25]. This model has the advantage of introducing a right-left symmetry which predicts the existence of right-handed neutrinos. It incorporates the *see-saw* mechanism which generates two neutrino masses, one of them to be very small by making the other arbitrarily large [137]. This could explain the lightness of the known left-handed neutrinos. Different versions of the model predict values of the heavy right handed neutrino from 1 TeV up to the GUT scale. As it has been shown, $SU(5)$ can be written in quite a simple way but unfortunately in this model the three running coupling constants do not meet in a single point. The proton lifetime predicted by this model is around $10^{32\pm1}$ y for non-supersymmetric models and $10^{34\pm1.5}$ y if Supersymmetry is included [138] (see 9.1.4).

9.1.4   Supersymmetry

Supersymmetry (SUSY) was originally proposed in 1973 by Julius Wess and Bruno Zumino [139]. However, the first realistic supersymmetric version of the Standard Model was proposed in 1981 by Savas Dimopoulos and Howard Georgi [26] and is called the Minimal Supersymmetric Standard Model (MSSM). The unification of the three forces, strong, weak, and electromagnetic is realized by introducing new particles in the region of ~ 1 TeV. Through the new particles introduced by SUSY models, the energy dependence of the running constants change and make them meet in a unification point at $\sim 10^{16}$ GeV.

Supersymmetry postulates a boson-fermion symmetry where for every standard-model particle there exist a corresponding supersymmetric particle (or *"sparticle"*) which has a spin that is different by 1/2 unit. Table 9.1 summarizes the particles in the standard model (SM) and the additionally introduced SUSY particles. Standard-model particles and its supersymmetric partners differ by the *R-parity*, where $R = 1$ for common particles and $R = -1$ for supersymmetric ones. Since R-parity is a conserved number, a SUSY particle can not decay into a common particle. This results in the existence of a SUSY particle, the lightest one (neutralino, gaugino or others, depending on the model) which is stable and could account for the dark matter in the Universe. In addition, SUSY has the possibility to unify with gravity [140][141]. Although great

	SM particles	spin		SUSY particles	spin
q_L	quark	$1/2$	$\tilde{q}_L$	squark	0
q_R	quark	$1/2$	$\tilde{q}_R$	squark	0
l_L	lepton	$1/2$	$\tilde{l}_L$	slepton	0
l_R	lepton	$1/2$	$\tilde{l}_R$	slepton	0
H_1, H_2	Higgs	0	$\tilde{H}_1, \tilde{H}_2$	higgsinos	$1/2$
g	gluon	1	$\tilde{g}$	gluino	$1/2$
γ	photon	1	$\tilde{\gamma}$	photino	$1/2$
Z^0	Z boson	1	$\tilde{Z}^0$	zino	$1/2$
$W^\pm$	W boson	1	$\tilde{W}^\pm$	wino	$1/2$

Table 9.1: The particles in the SM and in SUSY models.

experimental efforts have been made to find an evidence for supersymmetric particles, no observation has been made so far. Actually, one of the goals of the future LHC (Large Hadron Collider) at CERN is the search for SUSY particles [142] but also experiments which search for dark matter or for proton decay could point to its existence.

In the minimal supersymmetric $SU(5)$ model, the dominant decay modes of the proton involve pseudo-scalar bosons and anti-leptons [30]:

$$\overline{\nu}K^+, \ \overline{\nu}\pi^+, \ e^+K^0, \ \mu^+K^0, \ e^+\pi^0... \tag{9.9}$$

where the relative strengths depend on the specific exchange of the SUSY particles involved. However, in most of the models the proton-decay channel $p \rightarrow \overline{\nu}K^+$ is favored [30][141][143][144]. Figure 9.2 shows an example [141] of a Feynman diagram for a
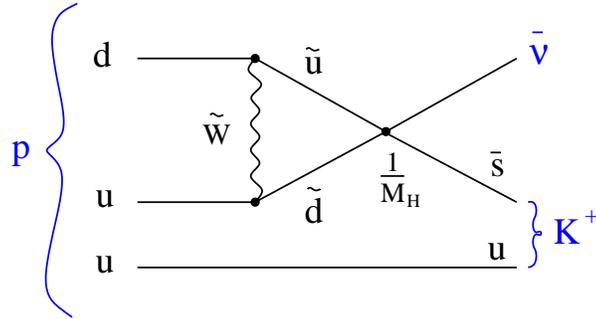
Figure 9.2: Example of a Feynman diagram of the decay $p \rightarrow \overline{\nu}K^+$ in Supersymmetry [141].

SUSY-favored proton decay reaction $p \rightarrow \overline{\nu}K^+$ where a higgsino ($\tilde{H}$, represented in the

105

figure by a vertex and labeled as $1/\mathrm{M}_H$) and a wino ($\tilde{W}$) are exchanged. The predictions concerning the lifetime of the proton are in the order of $10^{33} - 10^{34}$ y [143][144].

9.2   Experimental status

The search for proton decay addresses a fundamental question which has been investigated experimentally since at least 20 years. In 1954, the first proton-decay experiment was proposed by Maurice Goldhaber [145]. Later, many experiments have searched for these rare events: NUSEX [146], Fréjus [147], Soudan [148], IMB [149] and Kamiokande [150]. As no evidence has been reported so far, only lower limits on the proton lifetime have been obtained. The experiment with currently best sensitivity is the Superkamiokande detector. This experiment started in April 1996 and utilizes the Cherenkov effect in water having a fiducial volume of 22.5 kt. The best sensitivity is achieved for the decay channel $p \to \pi^0 e^+$ as it has a very clear signature and can be clearly distinguished from atmospheric neutrino reactions. The positron produces an electromagnetic shower and the neutral pion decays immediately (within 10^{-8} ns) into two gamma-rays which produce electromagnetic showers as well. Therefore, the signature consists of a double Cherenkov-ring structure (corresponding to the γs from π^0 decay) and a third ring in the opposite direction. The limit for the proton lifetime τ_p achieved for this decay channel is $\tau_p > 5 \cdot 10^{33}$ y. The investigation of the decay channel $p \to \overline{\nu} K^+$ in Super-Kamiokande has a much lower efficiency as the kaon is below the Cherenkov threshold in water. To search for this decay channel protons from oxygen are considered. The detection is performed by tagging a gamma ray which results from the nucleus deexcitation of the oxygen nucleus (due to the hole produced in the nuclear energy levels) and a delayed signal from the kaon decay particles. The sensitivity of Super-Kamiokande to this decay mode is $\tau_p > 2.3 \cdot 10^{33}$ y [29]. Table 9.2 summarizes some of the theoretically favored proton decay processes and the current best limits for the proton lifetime[1] arising from the experiments [28][29][151].

For the next future, already several proposals have been submitted to build new detectors which could be more sensitive than the existing ones. For example, the European proposal LAGUNA[2] [37] suggest among its main physics goals the search for proton decay (see chapter 1). The hope is to measure the lifetime of the proton or, if no positive signal is recorded, to constraint the parameter space for the existing theories beyond the SM.

---

[1]The lifetime actually refers to partial lifetime. An unknown branching ratio relates the proton lifetime to its partial lifetime in a certain decay channel.

[2]LAGUNA stands for Large Apparatus for Grand Unification and Neutrino Astrophysics.

Decay channel	Current lifetime best-limit	Experiment/Reference
$p \to \pi^0 e^+$	$500 \cdot 10^{31}$ y	Super-Kamiokande [28]
$p \to \pi^0 \mu^+$	$47 \cdot 10^{31}$ y	PDG [151]
$p \to K^+ \overline{\nu}$	$230 \cdot 10^{31}$ y	Super-Kamiokande [29]
$p \to \pi^+ \overline{\nu}$	$2.5 \cdot 10^{31}$ y	PDG [151]
$p \to \rho^+ \overline{\nu}$	$16 \cdot 10^{31}$ y	PDG [151]
$p \to K^0 e^+$	$100 \cdot 10^{31}$ y	Super-Kamiokande [29]
$p \to K^0 \mu^+$	$130 \cdot 10^{31}$ y	Super-Kamiokande [29]
$p \to e^+ \gamma$	$67 \cdot 10^{31}$ y	PDG [151]
$p \to \mu^+ \gamma$	$47.8 \cdot 10^{31}$ y	PDG [151]

Table 9.2: Summary of some of the theoretically favored proton-decay channels. The best current limits for the lifetime and the experiment/reference which set this limit are given in columns two and three, respectively. The complete list with the best proton decay limits can be found in [151].

9.3 Overview of the proton decay detection in LENA

A large-volume liquid-scintillator detector offers a complementary detection technique to the water-Cherenkov detectors for the search for proton decay. The main advantages of the scintillator technology are the excellent energy resolution ($\sim 10^2$ pe/MeV) and the low energy threshold due to the high light yield. In this section, general remarks about the proton decay detection mechanism are introduced. First, the target particles and some features concerning nuclear physics when nucleons are bound in nuclei are considered. Thereafter, an upper bound for the lifetime to all proton and nucleon decay reactions in LENA is given.

9.3.1 Number of target particles

The current design of the LENA detector has been introduced in section 3.2.2. It foresees a vertical cylindrical inner volume of $100\,\mathrm{m}$ height and $13\,\mathrm{m}$ radius which results in about $53\,000\,\mathrm{m}^3$ of liquid scintillator. The number of target particles in this volume can easily be calculated however, variations appear due to the specific scintillator solvent. In general, organic liquid scintillators have a composition of the form $\mathrm{C}_x \mathrm{H}_y$ (see chapter 5) providing y free protons and $12 \cdot x$ bounded protons. Table 9.3 summarizes the number of free and bound protons for different scintillator mixtures which are under discussion. The values are calculated for a fiducial volume of $44 \cdot 10^3\,\mathrm{m}^3$ and therefore, if a further fiducial volume cut is applied the number of target particles has to be reduced accordingly. For a scintillator based on pure PXE solvent, the total number of protons

Solvent	Free protons	Bound protons	Total Protons
Pure PXE	$2.3 \cdot 10^{33}$	$1.2 \cdot 10^{34}$	$1.45 \cdot 10^{34}$
PXE + 80% dodecan	$2.9 \cdot 10^{33}$	$9.4 \cdot 10^{33}$	$1.23 \cdot 10^{34}$
Pure LAB	$2.9 \cdot 10^{33}$	$1.0 \cdot 10^{34}$	$1.29 \cdot 10^{34}$

Table 9.3: Number of target nucleons for a fiducial volume of $44 \cdot 10^3 \, \text{m}^3$ in different liquid scintillator candidates.

is the largest of the three mixtures considered. However, for some applications (for example antineutrino detection) a high number of free protons is desired. Pure LAB or a mixture of 20% PXE and 80% dodecan have a lower total number of protons but a higher number of free protons than pure PXE.

9.3.2   Nuclear physics effects on bound nucleons

When protons from hydrogen are considered, the calculation of the proton-decay event topology is simplified. The kinetic energies of the decay particles can be calculated as a classical two-body problem at rest. In addition, the mass of the proton at rest can be used: $m_p = 938.27 \, \text{MeV}$. However, to increase the target mass or to consider the baryon number violating neutron decay, bound nucleons have to be included.

Nucleons bound in carbon have a Fermi momentum and a nuclear binding energy. The Fermi momentum has been measured in e^- scattering experiments on ^{12}C [152] leading to values up to $250 \, \text{MeV}/c^2$. In the analysis performed in this thesis, the Fermi motion of the nucleons has been considered. It affects the distribution of the nucleon mass and momentum between the daughter particles. In addition, the nucleon mass must be modified as well by the binding energy which is 37 or 16 MeV for nucleons in s- and p-state, respectively. The modified mass is calculated as $m'_N = m_N - E_b$ where m_N is the nucleon mass and E_b the corresponding binding energy [152].

When such a bound nucleon decay happens, the remaining nucleus can be in an excited state emitting prompt gamma-rays during its subsequent deexcitation process. For some nucleon-decay reactions, this prompt gamma can be used to tag the event. This method is used for example by Super-Kamiokande [29] to search for $p \rightarrow K^+ \overline{\nu}$ reactions as the kaon has an energy below the Cherenkov threshold in water (see section 9.2).

9.3.3   Calculation of the maximum detection potential

The sensitivity of LENA to search for different nucleon-decay processes is described in sections 9.6 and 9.7. However, it is useful to know how the sensitivity is calculated and

what is the maximum potential achievable.

The nucleon-decay activity a can be written as:

$$a = \epsilon N_p t_m / \tau \tag{9.10}$$

where ε is the total detection efficiency; N_p is the number of protons in the fiducial volume; t_m is the measuring time and τ is the lifetime of the proton. The parameter a represents the mean number of nucleon decays. As this is a rare process, a can be derived from the Poisson statistics. The Poisson distribution occurs when the probability p $\to$ 0 and the number of trials N $\to \infty$, such that the mean $a = $ N $\cdot$ p remains finite. The probability of observing r events is given by:

$$P(r) = \frac{a^r e^{-a}}{r!}. \tag{9.11}$$

To calculate the maximum sensitivity for the proton lifetime, the Poisson distribution is used. Assuming that no candidate event is measured, $r = 0$ and $P(0) = e^{-a}$, the activity at 90% confidence level can be easily calculated as $P(0) = 1 - 90\% = 0.1$ and therefore, $a = 2.3$. If now an efficiency of 100% is assumed, in 10 years measuring time the maximum achievable lifetime is $\tau_{p,max} = 6.3 \cdot 10^{34}$ y. This number has been calculated taking all (free and bound) protons for a PXE-based scintillator and assuming a background-free measurement. For a proton-decay reaction where only free protons can be considered, the achievable lifetime decreases to $\tau_{p,max} = 1 \cdot 10^{33}$ y in 10 years.

9.4 Monte Carlo simulations

To study the detector response to some of the proton decay events in LENA, a Monte Carlo simulation has been performed by using the C++-based Geant4 simulation toolkit [153]. In Geant4, there are three main classes which have to be defined by the user according to its specific physics problem: the detector geometry, the primary particle generator and the physics.

The detector geometry is defined as a cylinder of 100 m height and 24 m diameter. The sensitive volume (where physics processes can happen: fiducial volume) is the inner part of the cylinder. This corresponds to $44 \cdot 10^3$ m^3 target material which is defined as a mixture of carbon and hydrogen in the stoichiometry of the PXE molecules and with a density of 0.985 g/cm^3. The "standard" values for the scintillator optical parameters are set to 20 m absorption length, 20 m scattering length, 1.56 refractive index, 3.5 ns fast scintillation constant, 17 ns slow scintillation constant and 10 000 photons/MeV for the light yield. The volume around the scintillator is filled with water but it is not declared as sensitive volume. This simulation doesn't take into account the solute self-absorption effect (see chapter 8). For this reason, the fast scintillation constant is set to a quite

realistic value (3.5 ns) for a PXE-PPO mixture. The propagation parameters, absorption and scattering lengths are set to a constant value, i.e. are not wavelength-dependent.

In the primary-particle generator, the decay particles of the proton are produced. The position of the event is randomly distributed within the fiducial volume. For the decay reaction $p \to K^+ \overline{\nu}$, a positive kaon is generated with a random momentum direction. For the reaction $p \to \pi^0 e^+$, a neutral pion and a positron are generated with opposite momentum in a random direction. The kinetic energies of each particle are calculated from a two-body decay problem and given to the generator.

The physics class sets the interactions that generated particles and its secondaries should have. All particle interactions (electromagnetic, strong and weak) are used for the simulation. The charged particles deposit their energy in the medium or decay with the lifetime and branching ratios as given in the paper by the particle data group PDG [151]. The energy deposition leads to the emission of Cherenkov and scintillation light. The class which accounts for the scintillation mechanism is slightly modified to include particle quenching (see chapter 4). Birks formula [90] has been implemented in the code to take into account this effect where particles with high ionization density lead to additional energy losses.

9.5   Atmospheric neutrino background

In general, the signature of the proton-decay events consists of a high-energy prompt signal without having a signal in the outer detector. Depending on the decay reaction, the deposited energy of the events could vary from hundreds of MeV to a maximum energy of 938.37 MeV which corresponds to the proton mass. In this high-energy region, no background from natural radioactivity contributes. High-energy neutrons produced by spallation processes of cosmic muons in the surrounding rock can be neglected as well. On one hand, the 2 m thick water muon veto acts as a perfect moderator for neutrons and on the other hand by defining a fiducial volume inside the liquid-scintillator volume, the remaining neutrons can be identified as they produce recoil protons outside this volume. In addition, these signals can be tagged as the neutrons are captured by hydrogen in the scintillator after $\sim 180\,\mu$s, producing an observable 2.2 MeV gamma.

Finally, the only background which is relevant for the proton-decay detection is the contribution from atmospheric neutrinos. The expected atmospheric neutrino-rates in the energy region of the search for proton decay are calculated by scaling the measured rates of the Kamiokande [154] and Super-Kamiokande detectors [29] for the LENA detector. Thus, the total number of fully-contained events has been estimated [74] for LENA to be around 3 600 y for an energy range between 100 MeV and 10 GeV.

9.6 The decay reaction $p \rightarrow K^+ \overline{\nu}$

The proton-decay reaction $p \rightarrow K^+ \overline{\nu}$ is favored by most of the Supersymmetric models predicting a lifetime of about 10^{34} y [30]. The investigation of the sensitivity of LENA for proton decay in this mode has been studied in detail and published [66]. In this section, the main features of this decay channel are described. In addition, new simulations are presented where the values for the optical properties of the scintillator are taken from laboratory experiments. The aim is to investigate the impact of the scintillator's optical parameters on the efficiency and on the final proton-decay sensitivity. Special emphasis is given to the influence of the decay-time constants of the scintillator (see chapters 6 and 8) on the final sensitivity of LENA to proton decay.

9.6.1 Detection mechanism

From an experimental point of view, the proton decay via $p \rightarrow K^+ \overline{\nu}$ is of great interest, as a clear event signature can be identified in a liquid-scintillator detector. This signature consists of a double-peak structure which arises from the energy deposition by the kaon and later on, by its decay particles. Figure 9.3 shows an example of a proton-decay event in the LENA detector where the double-peak structure can be recognized.
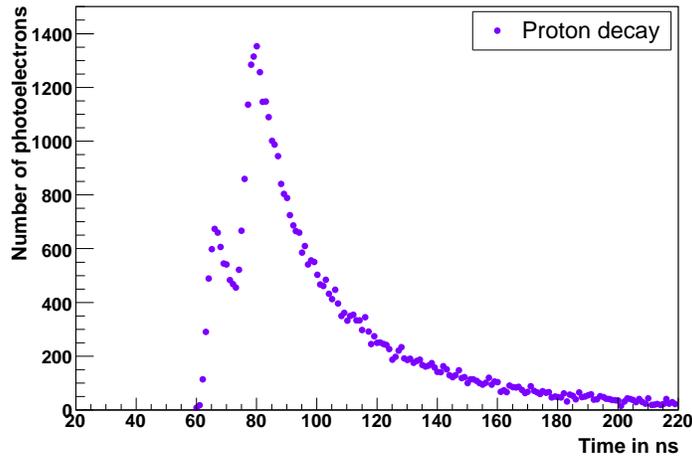
Figure 9.3: Example of a proton-decay pulse in the liquid-scintillator detector LENA. The first peak arises from the signal of the kaon while the second corresponds to the signal of the daughter particles.

If first the protons from H-nuclei (free protons) are considered, the kinematics is simplified as those protons decay at rest. Therefore, the proton decaying in the channel

111

$p \to K^+\bar{\nu}$ can be considered as a two-body decay problem. The energy corresponding to the mass of the proton, $m_p = 938.3\,\text{MeV}$, is thereby given to the decay products. Using relativistic kinematics, the energies of the kaon and of the neutrino can be calculated: 105 MeV and 339 MeV, respectively. In the LENA detector, the kaon causes a prompt mono-energetic signal and the neutrino escapes from the detector. After $\tau(K^+) = 12.8\,\text{ns}$, the kaon decays via $K^+ \to \mu^+\nu_\mu$ with a probability of 63.43 % [151]. From the kaon decay, a second mono-energetic signal arises, corresponding to the μ^+ with 152 MeV kinetic energy. Later, after $\tau(\mu^+) = 2.2\,\mu\text{s}$, also the muon decays: $\mu^+ \to e^+\nu_e\bar{\nu}_\mu$. With a smaller probability, 21.13 %, the kaon decays, alternatively, via $K^+ \to \pi^+\pi^0$. The π^+ deposits its kinetic energy (108 MeV) in the detector. The π^0 decays almost immediately, within $\tau(\pi^0) = 8.4 \cdot 10^{-8}\,\text{ns}$, into two gammas with a total energy being equal to the sum of the kinetic energy of the π^0 (111 MeV) and its rest mass ($m_{\pi^0} = 135\,\text{MeV}$). These gammas can be observed in the detector as they produce electromagnetic showers. Again there are two mono-energetic signals, first the kaon and then the one corresponding to the sum of the kinetic energy of the π^+ and the energy of the gammas. Figure 9.4 shows an energy spectrum in number of photoelectrons (pe) produced in the photomultipliers (110 pe = 1 MeV). The plot is the result of a simulation for free proton-decay events
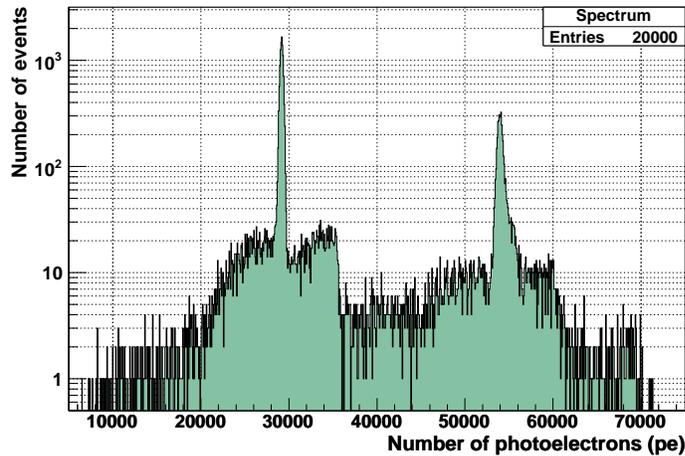
Figure 9.4: Simulation of the energy spectrum (in photoelectrons) for free proton-decay events in LENA. The two peaks represent the main decay channels of the kaon, namely $K^+ \to \mu^+\bar{\nu}$ (left peak) and $K^+ \to \pi^+\pi^0$ (right peak). The rest of the spectrum corresponds to other possible decay channels of the kaon with smaller branching ratios (in total $\sim 15\%$).

in the center of the detector. The two main peaks correspond to the kaon decay into $K^+ \to \mu^+\bar{\nu}$ and $K^+ \to \pi^+\pi^0$ which have branching ratios of 63% and 21%, respectively. The rest of the spectrum accounts for other decays of the kaon with smaller probabilities.

For the protons of the ^{12}C-nuclei (bound protons), further nuclear effects on the proton decay have to be considered (see section 9.3.2). The Fermi-motion affects slightly the event signature. The double-peak structure remains but the relative height of the kaon peak to that of its daugther particles changes as energy which the kaon deposits varies maximally by ± 37 MeV around the value of 105 MeV. The total energy of the event is also modified by the Fermi-motion. To take into account these variations, the energy region chosen for the proton decay analysis is quite wide, from 145 to 636 MeV (491 MeV energy window). With this energy cut, the detection efficiency is $\varepsilon_T = 0.995$.

9.6.2 Background rejection

The main background in the proton-decay search arises from charged current reactions of atmospheric neutrinos inside the detector being the produced lepton fully contained in the target volume. As the visible energies of the produced particles can be on the detection energy window of proton decay, a discrimination criterion is required. The expected rate of such events in LENA ($1190.4 \, \mathrm{y}^{-1}$) has been derived [155][156] from the Super-Kamiokande experimental data on atmospheric neutrinos [29].

To reduce this background a pulse-shape analysis has been applied to the simulated data. The method is rather simple: it calculates the time elapsed in the risetime for proton decay and for atmospheric neutrino events and compares them. In order to analyze the risetime of the resulting signal, the maximum number of photoelectrons is taken and the 15% and the 85% values of the maximum signal height are determined. The difference of the two corresponding time values is plotted in figure 9.5 for 10 000 proton decays and 20 000 background events.
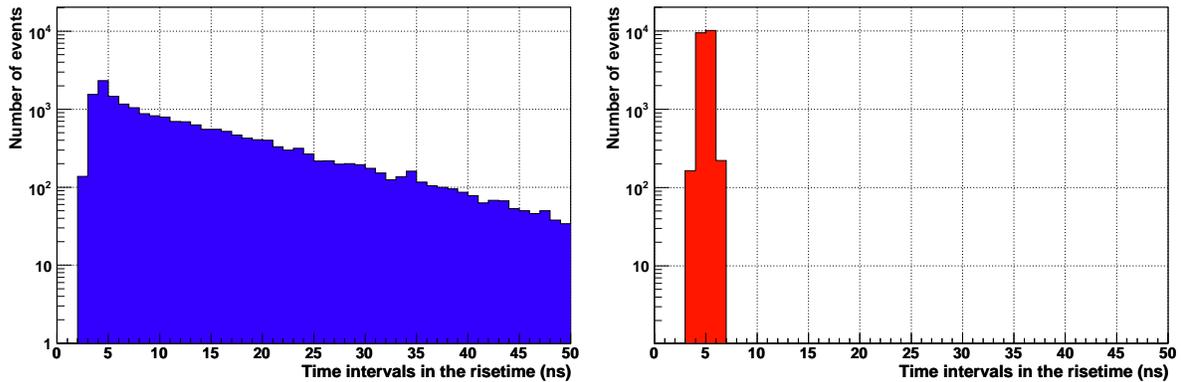
Figure 9.5: Distribution of time intervals in the risetimes for 20 000 proton-decay and 20 000 muon-background signals for a fast scintillator. A cut at 7 ns yields a reduction factor of $\sim 10^4$ for background events whereas the efficiency for observing a proton decay $p \to K^+ \overline{\nu}$ is 67.8%.

As an example, the effect of a cut at 7 ns is shown in this figure. The analysis performed for 20 000 background events shows that applying such a cut, a background reduction by a factor of $\sim 2 \cdot 10^4$ is achieved. This factor is already above the expected atmospheric neutrino rate in the detection energy window for 10 y measuring time. The background plot shown applies only to the channel $p \to K^+\bar{\nu}$ and $K^+ \to \pi^+\pi^0$. A similar simulation has been performed for the channel $p \to K^+\bar{\nu}$ and $K^+ \to \mu^+\nu_\mu$, resulting in an equivalent result where the same rejection factor is obtained. An efficiency of $\varepsilon_T = 0.65$ results after this time cut as only 35% of the signals are lost. As the analysis is performed within the signal risetime, the later part of the signal is lost. Further pulse-shape analysis where the complete signal is taken could be applied to increase the detection efficiency.

Hadron production

Atmospheric neutrinos can interact with the detector and produce also hadrons. The most probable of these reactions is the single-pion production [157][158]:

$$\nu_\mu + p \to \mu^- + \pi^+ + p'. \tag{9.12}$$

In such a reaction, a first prompt signal comes from the sum of the energies deposited by the μ^- and the π^+. Later, after $\tau_{\pi^+} = 26$ ns, the π^+ decays into μ^+ and a neutrino. Thus, a second short-delay signal originates from the μ^+. However, the π^+ and the μ^+ have such similar masses (139.6 and 105.7 MeV, respectively) that the decay muon receives only about 20 MeV kinetic energy. The signal produced by the μ^+ is small. Therefore, those events do not have the same signature as the proton decay signal. Moreover, since the muon signal is so small it is usually hidden behind the above-mentioned first signal.

Neutrinos of higher energies can interact producing particles with a strange quark, thus also kaon production has to be considered. According to the MINERvA proposal [53], the reactions of this type with notable probability are:

$$\nu_\mu + p \to \mu^- + K^+ + p, \tag{9.13}$$

$$\nu_\mu + n \to \mu^- + K^+ + \Lambda^0, \tag{9.14}$$

$$\text{and} \quad \nu_\mu + n \to \mu^- + K^+ + \Lambda^0 + \pi^0. \tag{9.15}$$

In equations 9.14 and 9.15, to conserve the strangeness number the kaon is produced together with a Λ^0 baryon. This Λ^0 particle decays after $\tau_{\Lambda^0} = 0.26$ ns mainly via two channels $\Lambda^0 \to p + \pi^-$ (63.9%) or $\Lambda^0 \to n + \pi^0$ (35.8%) [151]. Because of this short lifetime, the p, π^- or n, π^0 cause a prompt signal together with the μ^-, the K^+ and the π^0 in the case of equation 9.15. The prompt signal in these two reactions is bigger than the signal of the μ^+ from the kaon decay (or π^+, π^0 if the kaon decays within the

114

second-probable channel). For this reason, the signature of the background signal can be distinguished from proton decay events.

Reaction 9.13 can be responsible for a potential background for proton decay in the LENA detector. In this thesis it has been found that for this case, only neutrinos with energies between approximately 650 and 900 MeV can produce a signal with a signature similar to that of the proton decay [66]. This neutrino energy window has been determined considering the energy window of proton decay events relevant for the analysis $(150 - 650 \, \text{MeV})$ and the energies deposited by the particles in the possible background events. The atmospheric neutrino flux has a maximum around few hundreds of MeV and then decreases exponentially to higher energies. Assuming an energy dependence of $\phi_\nu \sim E_\nu^{-2.7}$ for the neutrino flux and a linear dependence for the cross-section, 10% of the total atmospheric neutrino flux occurs within the energy window considered in our analysis. Within this window a rate of 0.8 events per year (y^{-1}) caused by such neutrino reactions is predicted. To distinguish these background reactions from proton-decay events the number of delayed electrons produced have to be taken into account. For the proton decay in the channel considered, always one and only one electron is produced by the decay of the kaon. In the background reactions always two electrons are present, one from the μ^- decay and another from the K^+ decay chain. This fact considerably reduces the background contribution. Only in those cases where the energy of one of the background electrons is very small $(\text{E} < 0.5 \, \text{MeV})$ or when the signal of these electrons is hidden under that of the parent particle, the process exhibits only one electron. Events with electrons being hidden within the previous signal happen in 4% of the cases. From 200 muons simulated none of them had a decay electron with an energy smaller than 0.5 MeV. To estimate the number of background events of this type, the rate predicted has to be multiplied by this number 0.04 and then by two because electrons both from the μ^- and the K^+ decay chain can be hidden within the previous signal. Thus, the number of events of the type of reaction 9.13 expected in the LENA detector is $0.064 \, \text{y}^{-1}$.

Other reactions where hadrons are produced are possible but all of them have lower rates and can also be distinguished from a proton decay signal by applying the arguments used for reactions 9.14 and 9.15. A discussion on hadronic background in LENA can also be found in [155].

9.6.3 Sensitivity of the LENA detector to $p \rightarrow K^+\overline{\nu}$

The sensitivity of the proposed LENA detector to the proton-decay channel $p \rightarrow K^+\overline{\nu}$ can be calculated as described in section 9.3.3. The efficiency for the detection is determined by the cuts on the energy region and on the risetime:

$$\varepsilon = \varepsilon_E \cdot \varepsilon_T \tag{9.16}$$

where ε_E is the efficiency of the energy cut and ε_T the time cut for background discrimination. These efficiencies result from the Monte Carlo simulation described in section 9.4. The optical scintillator parameters taken for the simulation were the standard ones but the absorption and scattering lengths were set to 12 and 60 m, respectively. The influence of the scintillator parameters on the total efficiency is discussed in section 9.6.4.

In table 9.4 the efficiencies for events at different points within the detector are presented as well as the background rates for the same positions. As the detector

R (m)	ε_T	ε_E	ε (± 0.04)	B (y^{-1})
Center	0.649	0.995	0.65	0.11
3.0	0.675	0.994	0.67	0.11
6.0	0.650	0.994	0.65	0.11
9.0	0.679	0.995	0.68	0.11
11.5	0.666	0.995	0.66	0.11

Table 9.4: For 1000 events produced at each radial position R in the detector, the efficiency in the time-cut ε_T, the efficiency in the energy-cut ε_E, the total efficiency ε including the statistical error, and the background rate B are given.

is symmetrical along the cylinder axis the points considered are in the middle of the cylinder and at different radial distances. No dependency of the efficiency on the event position was found within the statistical error. This statistical error mainly comes from the time cut as that from the energy cut is negligible. The background rates presented have been obtained by multiplying the muon background rate in the LENA detector ($1190.4\,\mathrm{y}^{-1}$) derived from the Super-Kamiokande experiment [29] with the background suppression from the time cut ($5 \cdot 10^{-5}$, see section 9.6.2). The contribution of the kaon production background ($0.064\,\mathrm{y}^{-1}$) has been added to the previous value.

For the current proton lifetime limit for the channel considered ($\tau = 2.3 \cdot 10^{33}\,\mathrm{y}$) [29], about 40.7 proton-decay events would be observed in LENA after a measuring time of ten years with about 1.1 background events. If no signal is seen in the detector within this ten years, the lower limit for the lifetime of the proton will be placed at $\tau > 4 \cdot 10^{34}\,\mathrm{y}$ at 90% C.L. If one candidate is observed, the lower limit will be reduced to $\tau > 3 \cdot 10^{34}\,\mathrm{y}$ at 90% C.L. and the probability of this event being background would be 32%.

9.6.4 Impact of the detector's optical properties

The analysis presented above relies on the possibility to reject all atmospheric neutrino background events via pulse-shape analysis (risetime cut). However, to achieve this discrimination a liquid scintillator mixture with fast decay constants and large scattering

λ (m)	λ_a (m)	λ_s (m)	ε	Y (pe/MeV)	Cut (ns)
5	10	10	0.56	58	10
7	14	14	0.65	116	8
9	18	18	0.67	161	7
10	12	60	0.65	110	7
10	15	30	0.69	145	7
10	20	20	0.66	180	7
10	30	15	0.63	230	8
10	60	12	0.62	303	9

Table 9.5: Efficiencies ε for the detection of proton decay and photoelectron yield Y as function of attenuation, absorption and scattering lengths. The last column shows the time (see figure 9.5) at which the cut can be performed such that all background signals are rejected. Upper part: Different attenuation lengths for $\lambda_a = \lambda_s$. Bottom part: Attenuation length $\lambda = 10$ m for different combinations of λ_a and λ_s.

lengths is required. In this section, the results of further simulations are presented where the impact of optical properties of the detector on the sensitivity were studied.

First, the absorption and scattering-length parameters were investigated. Several simulations were performed where these two values were varied. In table 9.5 the efficiencies for proton-decay detection and the obtained photoelectron yield are given as function of different attenuation λ, absorption λ_a and scattering λ_s lengths. For the results presented, 1000 proton decay and 1000 background events were simulated for each combination of λ_a, λ_s and λ. All events were generated at the center of the detector. The last column of the table shows the time (see figure 9.5) at which the cut can be performed such that all background signals are rejected. In the upper part of the table, three attenuation lengths λ are presented keeping the contributions of absorption length and scattering length equal, $\lambda_a = \lambda_s$. As the attenuation length increases the photoelectron yield Y increases and the cut in the time intervals can be performed earlier. In the bottom part, the attenuation length has always the same value $\lambda = 10$ m for different values for the absorption and scattering lengths satisfying the equation: $\frac{1}{\lambda} = \frac{1}{\lambda_a} + \frac{1}{\lambda_s}$. The photoelectron yield increases as the absorption length increases because more optical photons reach the photomultipliers and therefore more photoelectrons are produced. As the scattering length increases, the cut in the time intervals can be performed earlier because the time information is better. Table 9.5 shows that in all cases investigated, for $\lambda > 7$ m the efficiencies $\varepsilon > 0.62$. This is also true for $\lambda_a = 12$ m and $\lambda_s = 60$ m, which we used for deriving the results presented in section 9.6.3. However, substantial differences can appear in the efficiency depending on these propagation parameters. For example, about 20% efficiency is lost if the total attenuation length decreases to 5 m.

In chapter 6, the results of the probability density function of several scintillator mixtures have been presented. It is shown there that the shortest fluorescence decay-constant, τ_1, accounts for the main part of the photons in the scintillation pulse. The constant τ_1 varies from 2 to 8 ns depending on the mixture. Further simulations have been performed to study the influence of the shortest decay constant on the pulse-shape discrimination. For this purpose, proton-decay and background events are produced for a liquid scintillator with a fast time constant τ_1 equal to 3 and 6 ns, respectively. These values have been taken as examples. As seen in chapter 8, differences in these values can be due to several processes: slow energy-transfer between solvent molecules, long lifetime of the singlet state in the solute, or absorption-reemission processes. In addition, new laboratory measurements [134] show that the absorption and scattering-length values (λ_a and λ_s) taken for the analysis in section 9.6.3 and in [66] were too conservative. Thus, now the measured values of $\lambda_a = 20$ m and $\lambda_s = 20$ m are implemented in the simulation and are taken as "standard". With these values, a photoelectron light yield of 180 pe/MeV is obtained. This value can be compared with that of the Borexino detector: 500 pe/MeV [23].

In figure 9.6, the photoelectron spectra of two proton-decay simulations are shown. Only one parameter has been changed: for the left plot the shortest fluorescence decay-
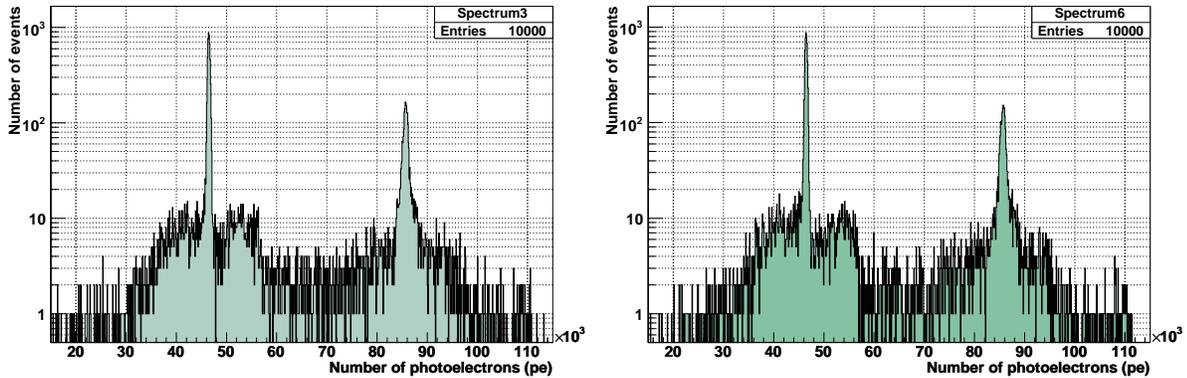
Figure 9.6: Simulated energy spectra (in photoelectrons) of the proton decay in LENA. The two peaks represent the main decay channels of the kaon, namely $K^+ \to \mu^+ \overline{\nu}$ and $K^+ \to \pi^+ \pi^0$. The rest of the spectrum corresponds to other possible decay channels of the kaon with smaller branching ratios (in total 10%). The left plot shows the spectrum for a fluorescence decay-time constant of $\tau_1 = 3$ ns and the right plot for $\tau_1 = 6$ ns.

time constant is taken as $\tau_1 = 3$ ns and for the second $\tau_1 = 6$ ns. For these values the same pulse-shape analysis as described in section 9.6.2 is applied. Figure 9.7 shows the results of the risetime distribution for proton-decay events (left) and for background events (right) (for explanations see section 9.6.2). The upper panels correspond to a simulation where the decay-time constant τ_1 had a relatively short values $\tau_1 = 3$ ns and
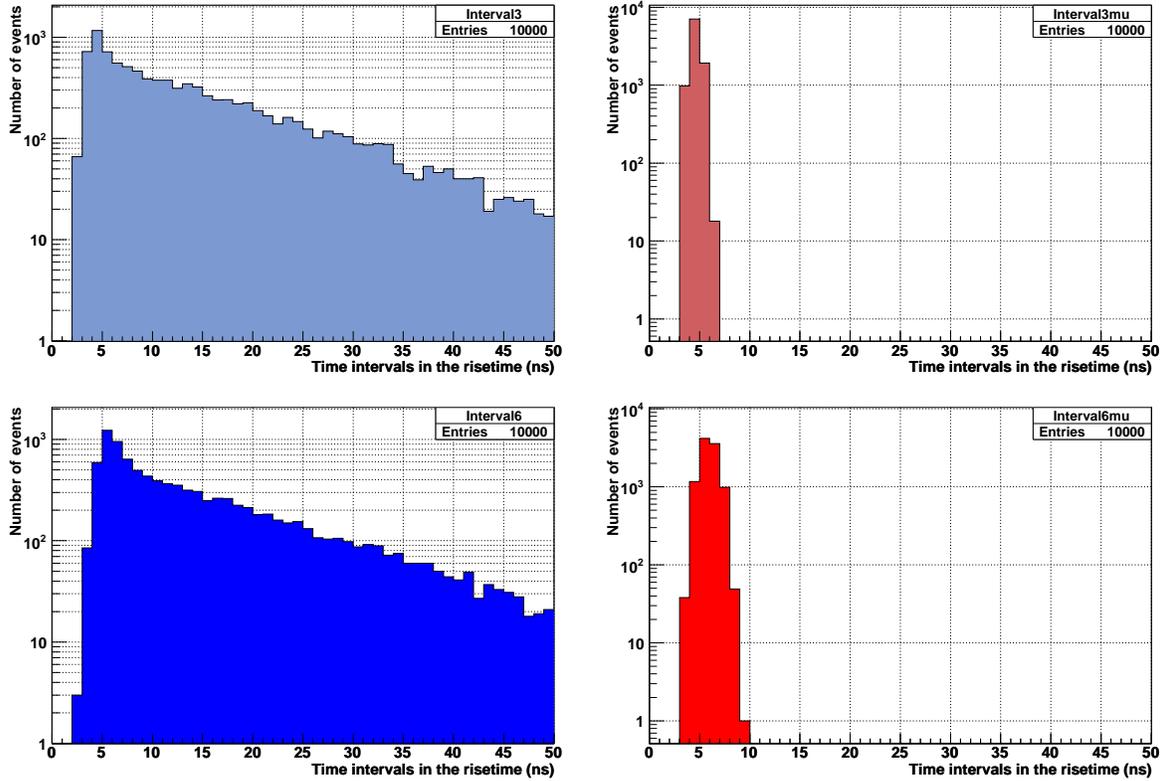
Figure 9.7: Distribution of time intervals in the risetimes for 10 000 proton-decay (left) and 10 000 muon-background signals (right) for scintillators with a shortest time constant of $\tau_1 = 3$ ns and $\tau_1 = 6$ ns. Top panels: A cut at 7 ns yields a reduction factor of $\sim 10^4$ for background events whereas the efficiency for observing a proton decay $p \to K^+ \overline{\nu}$ is 67.8%. Bottom pannels: A cut at 10 ns yields a reduction factor of $\sim 10^4$ for background events being the proton-decay efficiency is 56.6%.

in the lower panels $\tau_1 = 6$ ns. The main differences can be observed on the background events. For a slower scintillator, the risetime of a muon pulse is longer and the cut in the time difference to suppress this background has to be applied for a larger value (10 ns). For the simulation with $\tau_1 = 3$ ns, a cut on the risetime at 7 ns yields a reduction factor of $\sim 10^4$ for background events whereas the efficiency for observing a proton decay $p \to K^+ \overline{\nu}$ is 67.8%. For the simulation where $\tau_1 = 6$ ns is used, a cut at 10 ns yields also a reduction factor of $\sim 10^4$ for background events and the proton-decay efficiency is reduced to 56.6%. This differences on the detection efficiencies lead to a 20% effect on the sensitivity to proton decay.

119

9.7 The decay reaction $p \rightarrow e^+ \pi^0$

As explained in section 9.1.2, the original $SU(5)$ model and also some of its expansions predict as dominant proton-decay mode $p \rightarrow e^+ \pi^0$ [24][136]. The Super-Kamiokande detector has a high detection efficiency to search for this reaction (see section 9.2). As so far no positive signal has been observed, a limit on the proton lifetime has been set $\tau > 5 \cdot 10^{33}$ y [28]. However, it is of interest to test and improve this result with a different technology. For this reason, the topology of this decay has also been studied for the liquid-scintillator detector LENA. A first estimation of the efficiency, background rejection and sensitivity is given. At the end, some ideas to improve the background rejection are explained.

9.7.1 Detection mechanism

First, the decay of the proton via $p \rightarrow e^+ \pi^0$ is considered for free protons. In this case, the energies of the e^+ and the π^0 can be calculated according to a two-body decay problem, as 459 and 344 MeV, respectively. As the π^0 decays immediately ($\tau_{\pi^0} = 8.4 \cdot 10^{-8}$ ns) into two gamma-rays, an electromagnetic shower is produced. The e^+ as well produces an electromagnetic shower in the opposite direction. In principle, no directional information can be used in LENA due to the homogeneous emission of the scintillation light. Therefore, the signature of the event is just a peak in the energy spectrum at an energy corresponding to the proton mass. Due to the good energy resolution of the detector, this can be used to reject, at a certain level, the atmospheric neutrino-background.

To estimate the energy resolution of the LENA detector for such proton-decay events, the Geant4 simulation described in section 9.4 has been used. The event generator has been changed to produce a π^0 and an e^+ of 459 and 344 MeV, respectively which propagate in opposite directions. The optical parameters of the scintillation process are the standard values described in section 9.4. Figure 9.8 shows the energy spectrum (in photoelectrons) for 5 000 proton-decay events in the center of the detector. The spectrum has been fitted with a Gaussian function although it can be observed that the distribution is not perfectly symmetric. This can be due to differences in the electromagnetic shower development. The position of the peak at $\sim 181\,000$ pe shows a photoelectron yield of ~ 193 pe/MeV. This value is slightly above the yield calculated for the proton-decay channel $p \rightarrow K^+ \overline{\nu}$ (180 pe/MeV, see figure 9.6) although the optical properties of the medium were the same. This effect is actually due to the fact that the energy deposited by the kaon is quenched in the liquid scintillator (see equation 4.4 in chapter 4). The width of the distribution, $\sigma = 1097 \pm 15$ pe, shows an energy resolution of 0.6%. This signal corresponds to the light produced by the two electromagnetic showers. The results of the simulation show that each of the electromagnetic showers have a mean
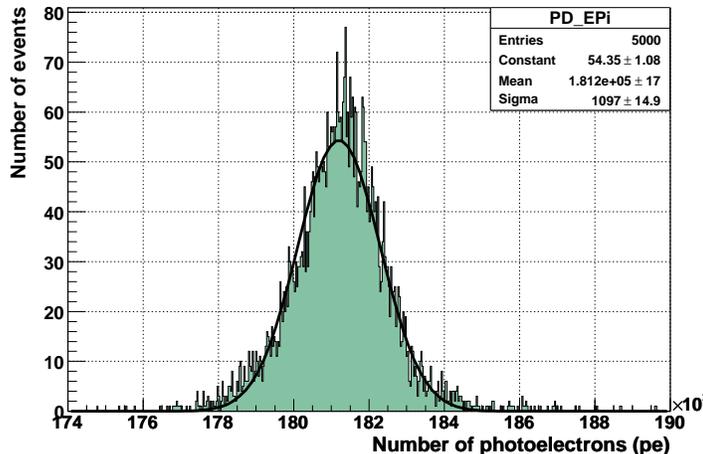
Figure 9.8: Simulated energy spectrum (in photoelectrons, $193\,\mathrm{pe} = 1\,\mathrm{MeV}$) of the proton decay $p \to e^+\pi^0$ in LENA. $5\,000$ simulated events are represented.

length of about $4\,\mathrm{m}$.

9.7.2 Background rejection and sensitivity

Due to the absence of a special signature for $p \to e^+\pi^0$ events, interactions of atmospheric neutrinos in the detector have to be considered. However, charged-current interactions where a muon is produced don't contribute to the background. This is due to the e^- signal from the muon decay as this delayed coincidence can be used to discriminate such events from proton decay. Reactions of $\overline{\nu}_e$ can, in principle, also be distinguished as its charged current interaction with a proton produces a neutron which can be detected. This neutron thermalizes and it can later be captured by a free proton leading to a $2.2\,\mathrm{MeV}$ gamma-ray. However, if the neutron is produced in a carbon nucleus, its secondary interactions can result in the production of a pion or a proton leading to the loss of the neutron. Therefore, to be conservative, all ν_e and $\overline{\nu}_e$ interactions in the detector are taken into account for this analysis.

To calculate the background rate, the data from the Kamiokande detector has been used [154]. Between 900 and $1\,000\,\mathrm{MeV}$ energy about 6 events from ν_e and $\overline{\nu}_e$ interactions were detected for a $2.8\,\mathrm{kt.y}$ exposure. Scaling this results to the fiducial volume of LENA ($44\,\mathrm{kt}$), about 94 events per year are expected in the energy window mentioned above.

In order to measure background free (expected rate below $1\,\mathrm{count/y}$), a narrow energy window can be chosen. For an energy window between 938 and $939\,\mathrm{MeV}$ (between 180929 and 181122 photoelectrons in figure 9.8), a background rate of $\sim$0.9 events per

year is expected. Consequently, for this narrow energy window the detection efficiency is reduced to ∼12%. The sensitivity to detect proton decay via $p \rightarrow e^+ \pi^0$ can be calculated as shown in section 9.3.3. If no candidate event is detected within one year of measuring time, a limit on the proton-decay lifetime of $1.2 \cdot 10^{32}$ y can be reached. For this calculation, only free protons have been considered. Events from bound protons are smeared out as the contribution of nuclear processes like Fermi motion and binding energy has to be considered (see section 9.3.2). For this case, scintillator mixtures with a large number of free protons are favored.

The calculated sensitivity is a factor of 20 worse than the current limit from the Super-Kamiokande experiment [28]. However, no background-discrimination criterion has been used so far. In section 9.7.3, some ideas to improve the background rejection and therefore increase the detection efficiency are discussed.

9.7.3 Possible improvements

To further increase the sensitivity, an additional criterion for background discrimination is required. A promising idea would be to use the information on the spatial distribution of the PMT hits combined with the photon arrival time. That means to try the tracking of the particles involve in the event. For atmospheric neutrino events where a charged lepton is produced, a lepton track is expected. For a proton-decay event, two tracks are produced (two electromagnetic showers) which propagate in opposite directions.

A possibility to separate neutrino signals from proton-decay events would be to use a position-reconstruction code like that used in [51]. This code gives the reconstructed position of a point-like event and estimates its error. Although more elaborate reconstruction programs can be developed, the existing one can be used for a first study. By using the arrival time and the distribution of the first (0 to ∼ 10 ns) hits on the PMTs, the starting position of the event could be determined with good precision. Next, the position reconstruction could be performed by taking the rest of the hits in the event (> 10 ns). Of course, the latter reconstructed position will be affected by a large error as a track length of few meters differs from a point-like event. However, the interesting result is the reconstructed position. If the event was a propagating particle from a neutrino interaction a shift in the position reconstruction would appear. For a proton-decay event, the position would be reconstructed in a similar place leading to a shorter shift. The shift between the reconstructed positions could be used as discrimination parameter between proton decay and background events.

Figure 9.9, shows an example of a muon event simulated [51] with a Geant4-based Monte Carlo. The muon propagates in along the cylinder axis of the LENA detector (horizontal direction in the figure). The picture represents a projection of the LENA detector surface onto a plane. The rectangle correspond to 100 m height $\times$ $2\pi r$ with $r = 12$ m being the radius of the LENA fiducial volume. The circles (left and right)
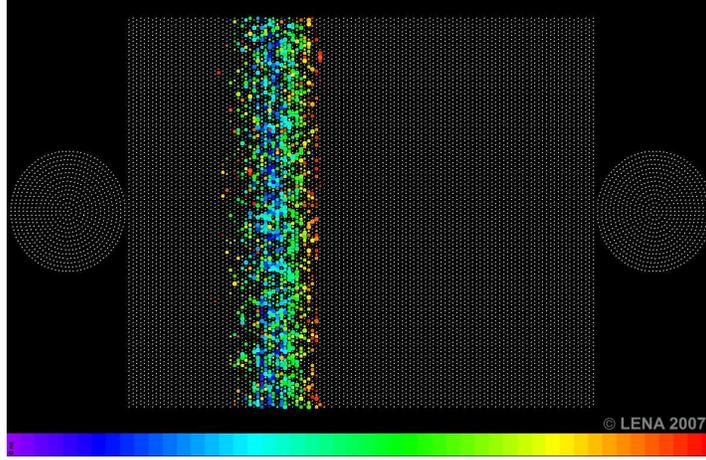
Figure 9.9: Simulated muon propagating along the cylinder axis in the LENA detector. In this projection of the LENA detector surface, the white points represent the positions of the PMT tubes. The colored points are hits in the PMT, the color code representing a time scale. This scale ranges from 0 ns (violet) to 25 ns (red). Further details are given in text. Picture from [159].

represent the end-caps of the detector. The white points show the position of the PMT tubes. The colored points are photon hits in the PMTs. The color code corresponds to a time scale. This scale ranges from 0 ns (violet, corresponding to the first PMT hit) to 25 ns (red). In this picture only hits within the 25 ns after the first hit are shown. A muon of about 938 MeV has been generated in the center of the detector and it propagates along the cylinder axis. This is one very simple example, but it shows easily the underlying idea. The distribution and time of the hits show that the muon propagates from left to right (more red points on the right part of figure 9.9). For a proton-decay event, a symmetric structure of the hits is expected. Although no analysis has been performed yet for this first simulation, the picture shows that there is a potential criterion for background discrimination.

9.8 Alternative baryon number violating processes

In the previous sections, the theoretically favored proton-decay channels $p \rightarrow K^+ \overline{\nu}$ and $p \rightarrow e^+ \pi^0$ have been discussed. However, a large number of processes which violate the baryon number have been discussed in the literature (see for example [30] and references therein). Some examples of these further baryon-number violating decay channels are: $p \rightarrow \pi^+ \overline{\nu}$, $p \rightarrow \rho^+ \overline{\nu}$, $p \rightarrow e^+ K^0$, $p \rightarrow \mu^+ K^0$, $p \rightarrow \mu^+ \pi^0$, $n \rightarrow \nu\nu\nu$.

The LENA detector could also search for some of these additional reactions. For the proton-decay reactions where a neutrino is produced ($\pi^+\overline{\nu}$, $\rho^+\overline{\nu}$), a peak at some hundreds of MeV is expected. This energy corresponds to the deposited energy by the particles and its decay products. The background rejection is performed by selecting a very narrow energy window around the expected peak (method as described in section 9.7). In these cases, only free protons can be considered as the Fermi motion smears out the energy deposition in the event.

Similarly to $p \rightarrow e^+\pi^0$, the proton decay channels where the mass of the proton is converted into visible energy could be investigated ($p \rightarrow \mu^+\pi^0$, $p \rightarrow \mu^+\gamma$, $p \rightarrow e^+\gamma$). For these cases, a detection method similar to that explained in section 9.7 could be used leading also to sensitivities of $\tau > 10^{32}$ y. If the tracking capabilities proposed in section 9.7.3 give a positive result, the sensitivity for theses decay channels could also be improved.

The neutron-decay (baryon-number violating) reaction $n \rightarrow \nu\nu\nu$ has been investigated by the CTF detector [160]. In this case, after the decay of the neutron, the remaining nucleus (^{11}C) is in an excited state. From its relaxation, a 2 MeV gamma-ray is produced which can be tagged in the detector. However, this signal is affected by muon-induced cosmogenic background. This background refers to high-energy muons which induce spallation processes in the ^{12}C nuclei leading to a ^{10}C nucleus and two neutrons. Depending on the capability of the detector to tag such events [45], the background for this neutron decay channel can be rejected. The limit set by the CTF detector for this partial lifetime is $\tau > 1.8 \cdot 10^{25}$ y at 90% C.L. [160]. Similar studies can already be performed in Borexino [20] and also in the LENA detector.

In summary, in this chapter it has been shown that the future LENA detector has a high efficiency and an excellent background rejection to search for proton decay via $p \rightarrow K^+\overline{\nu}$. Therefore, a sensitivity of $4 \cdot 10^{34}$ y has been obtained. The search for further baryon-number violating processes is also feasible and even very promising but further studies have to be performed to show the final sensitivity.

Chapter 10

Further simulations: beta beam detection in LENA

This chapter describes simulations performed to determine the potential of LENA as a detector for a beta-beam experiment. After a physics motivation and a description of the beta-beam concept, the simulations carried out are presented and first results concerning lepton identification are discussed. Finally, an overview concerning the main difficulties found and the required future work is given.

10.1   Physics motivation

In the neutrino mixing matrix (see chapter 1), there are still at least two unknown parameters: the mixing angle θ_{13} and and the CP-violating phase δ_{CP}. Several experiments have been set up to search for the value of θ_{13} or are currently under construction. The current best limit of $\sin^2 2\theta_{13} < 0.2$ is coming from the CHOOZ liquid-scintillator reactor experiment [17]. In this experiment, the $\overline{\nu}_e$ flux from a nearby reactor ($\sim 1\,\mathrm{km}$ distance) was analyzed without obtaining any evidence for neutrino oscillations.

In the next future, the reactor neutrino experiments Double-CHOOZ [161] and Daya Bay [19] can be expected to be in operation. Due to the planned second detector, the systematic uncertainties can be reduced and the design sensitivity of around $\sin^2 2\theta_{13} < 0.03$ and < 0.02 could be reached, respectively. Current accelerator experiments, as MINOS [162] or OPERA [163], will also contribute to a better knowledge of this parameter, however with a limited sensitivity. The limitation originates mainly from the imprecise knowledge of the electron-neutrino contamination of the muon-neutrino accelerator beam.

10.2   Introduction to beta beams

A new method for the production of intense and pure neutrino beams has been proposed a few years ago: the *beta beam* [70]. It exploits the beta decay of boosted radioactive ions. Such a novel concept has three main advantages: well-known neutrino fluxes, flavor purity and high collimation of the beam.

Although many candidate isotopes have been under discussion, particular interest is given to ^{18}Ne and ^{6}He [70]. These isotopes have β-decay endpoint energies of $E_{e,max} = 3.4$ MeV and $E_{e,max} = 3.5$ MeV, respectively. Neon undergoes a β^+ decay producing ν_e while Helium decays via β^- producing $\overline{\nu}_e$:

$$^{18}\text{Ne} \rightarrow^{18} \text{F} + e^+ + \nu_e \tag{10.1}$$

$$^6\text{He} \rightarrow^6 \text{Li} + e^- + \overline{\nu}_e. \tag{10.2}$$

The acceleration of these isotopes produces a boosted beta spectrum of pure $\overline{\nu}_e$ or ν_e. By measuring the ν_μ appearance rate, information on the Θ_{13} oscillation parameter could be obtained. Additionally, if both isotopes are used, δ_{CP} could be determined by comparing the appearance rates of ν_μ and $\overline{\nu}_\mu$. However in the oscillation formula, θ_{13} and δ_{CP} appear in the same term leading to degeneracies [164]. In order to disentangle these degeneracies, energy-dependent oscillations should be studied.

A possible realization of such an experiment has been studied in the project EU-RISOL [165] at CERN. This study explores the possibility of using existing CERN machines for the acceleration of radioactive isotopes. A picture of the possible facility can be seen in figure 10.1. The existing facilities at CERN, PS (proton synchrotron) and SPS (super proton synchrotron), are shown in black. The facilities which would have to be built are depicted in red: the ion source on the left and the decay ring on the right. Further details are given in [165].

A suitable detector for a beta-beam experiment should have a large target mass to gain high statistics and the capability of ν_e/ν_μ separation. In addition, to reach an energy-dependent oscillation measurement the neutrino energy should be reconstructed [164]. This can be either achieved by determining the direction of the outcoming lepton or by reconstructing the energy of all produced particles. As LENA fulfills the requirement for large mass, a brief evaluation of further capabilities of the detector have been investigated within this thesis.

10.3   Electron/muon separation in LENA

For neutrinos at energies between 100 MeV and about 2 GeV, the dominant reaction is the quasi-elastic scattering on nuclei, i.e. the charge-current interaction producing the
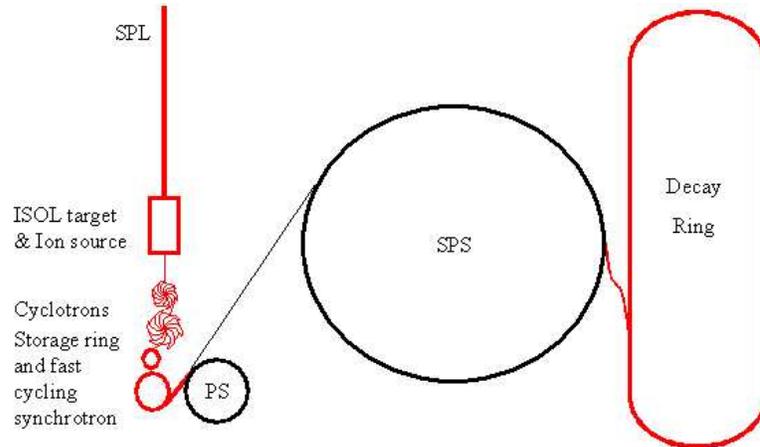
Figure 10.1: Planned EURISOL [165] facility at CERN. The existing facilities, PS (proton synchrotron) and SPS (super proton synchrotron), are shown in black. In red, the facilities which would have to be built are indicated.

corresponding lepton. As a first step to evaluate the potential of the LENA detector for a beta-beam experiment, the discrimination between muons and electrons produced in quasi-elastic reactions has been studied. To this end, mono-energetic muons and electrons have been simulated and several discrimination criteria have been searched for to separate these events. The response of the detector to these two types of particles has been investigated by using the Geant4 [153] simulation toolkit. The details of the simulation structure and the used parameters for LENA are given in chapter 9.

For low energies, a criterion has been found to recognize muons as the electrons of their succeeding decay after $2.2\,\mu$s can be clearly registered in LENA. As long as the energy threshold for the pion production reactions is not reached, there is no significant background for this method. However, the efficiency of the electron detection has to be considered. In 4% of the muon decays, the e^- signal comes within 200 ns after the muon pulse and therefore overlaps with its tail leading to an unidentified electron signal. For energies above the pion production threshold, the criterion can still be used but an electron background has to be included.

For high energies, a pulse shape discrimination criterion can be applied. In general, muons travel longer distances than electrons as electrons undergo scattering and bremsstrahlung while muons are close to minimal ionizing particles. This results in different distributions of the number of photons and the timing pattern of the arriving photons. Figure 10.2 shows an example of an electron and a muon pulse of 1.0 GeV energy where the different pulse shapes can be distinguished.

In general, electron pulses have a steeper risetime and a shorter width while muon

127
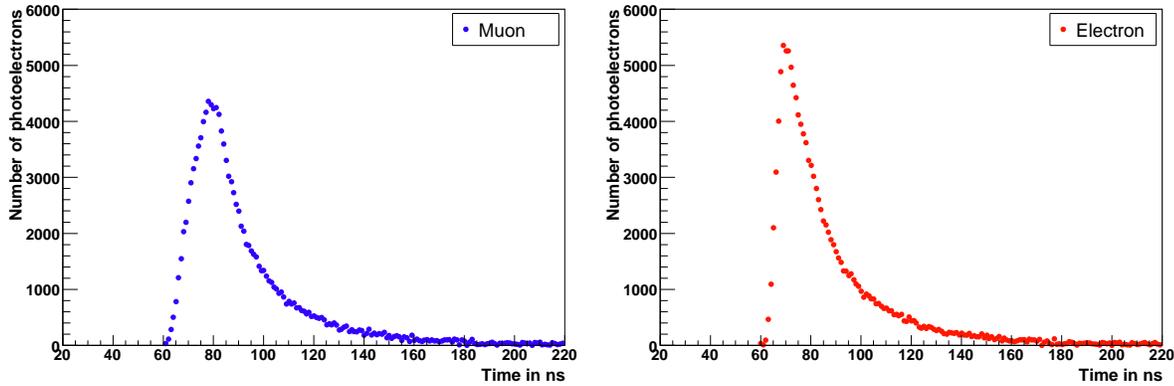
Figure 10.2: Examples of a muon (left) and an electron (right) pulse for 1.0 GeV particle energy.

pulses have a flatter risetime and a larger width for the same particle energy. Therefore, the risetime of the pulse and the half width at half maximum (HWHM) are characteristic parameters to discriminate muon and electron signals. For several electron and muon energies, the risetimes and HWHM are calculated. In figure 10.3, scatter plots are shown where risetime and HWHM of the electron and muon pulses are plotted relative to each other. In these scatter plots, electron (in red) and muon (in blue) parameters are represented for the energies 1.2 GeV, 1.0 GeV, 0.6 GeV, and 0.4 GeV. In general, it can be seen that muons have a more confined values of risetime and HWHM. If a cut is performed to the risetime and HWHM around the parameter values of the muon signals, the muon appearance efficiency and the electron contamination rate can be determined. As an example, at 1.2 GeV (upper plot on the right in figure 10.3) the cuts can be set for the range between 8 and 12 ns for the risetime and for the range between 10 and 15 ns for HWHM, leading to a muon appearance efficiency of 96.3% with 0.2% electron contamination. The position of the cuts was chosen to optimize muon efficiency minimizing at the same time electron acceptance (below 1%).

From $0.2 - 1.2$ GeV, the performed simulations show that muon events are separable from electron events due to their different track lengths in the detector and due to the secondary electron emitted in the muon decay. Both criteria are complementary and can be combined to analyze the potential of LENA for particle separation. For the whole energy range, an efficiency of $\sim 90\,\%$ for muon recognition has been calculated with an acceptance of $1\,\%$ electron background.
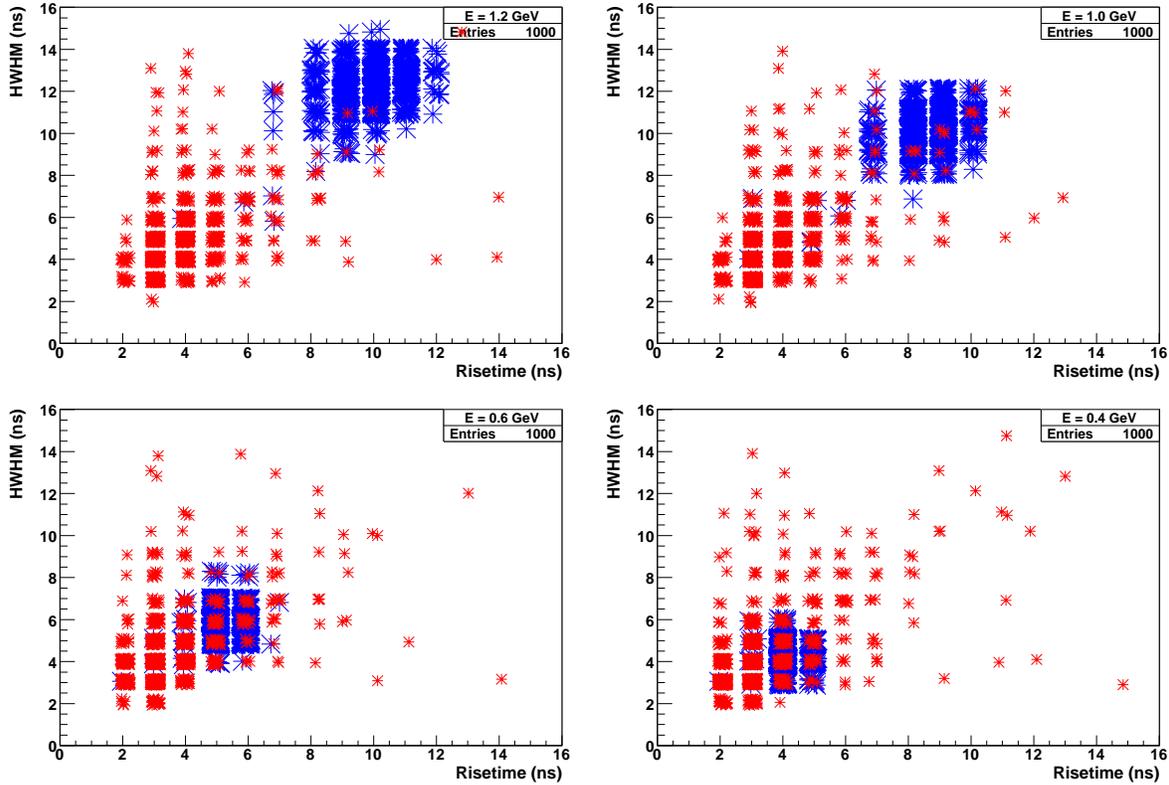
Figure 10.3: Scatter plots for electrons (red) and muons (blue) with energies of $1.2\,\text{GeV}$, $1.0\,\text{GeV}$, $0.6\,\text{GeV}$ and $0.4\,\text{GeV}$, respectively. On the x axis the risetime of the pulses is plotted and on the y the half width at half maximum (HWHM). At higher energies ($> 1\,\text{GeV}$), a pulse shape analysis gives good muon-electron separation.

10.4 Neutrino interactions and energy quenching

The results given in the previous section refer to the discrimination power between mono-energetic muons and electrons. However, for a neutrino oscillation experiment the neutrino interactions have to be considered. The cross sections, the kinematics of the reactions and the nuclear physics processes have to be taken into account in order to estimate the neutrino energy resolution. As mentioned before, the energy information of the incoming neutrino is necessary to disentangle θ_{13} and δ_{CP}.

As the scintillator technology has, in principle, no tracking capabilities, the information on the incoming neutrino can only be obtained by reconstructing the energy of all produced particles. A first look into the effects of neutrino interactions has been obtained by simulating neutrino interactions in a liquid scintillator. For this purpose,

129

the software tool Nuance [166] has been used[1]. Nuance is a FORTRAN-based software where all kinds of neutrino interactions are taken into account, e.g. charge and neutral current reactions in quasi-elastic and deep-inelastic regimes, resonant and diffractive pion production or scattering on electrons. In the simulation, LENA was defined as a cylinder filled with liquid scintillator. The target was assumed to be of pure PXE scintillator with a density of $0.985\,\mathrm{g/cm^3}$ and chemical composition $C_{16}H_{18}$.

From the simulations performed, two main difficulties have been identified. First, the kinematics of the interactions are modified by the Fermi motion of the nucleon in ^{12}C with which the neutrino reacts. This affects the energy reconstruction by lowering the visible energy. The available energy corresponds to the proton mass minus the maximum nucleon binding energy in ^{12}C which goes up to $37\,\mathrm{MeV}$. The contribution of this effect ranges from 18% to 3% for 0.2 to $1.2\,\mathrm{GeV}$ energy, respectively. More information about the Fermi motion can be found in chapter 9. Even more important are secondary strong interactions of nucleons or pions produced in the first neutrino interaction vertex. These secondary interactions can produce further pions and also a knock-out of nucleons. The production of charged pions results in a loss of visible energy as neutrinos appear as decay products ($\pi^+ \to \mu^+\nu_\mu$) taking some of the energy away. In case of proton knock out [167] again part of the visible energy can be lost due to particle quenching effects: for particles heavier than electrons, the ionization density in the energy deposition increases leading to a loss of produced photons (further details are given in chapter 5).

10.5   Conclusion

From the performed simulations, no clear conclusion of the potential of LENA as a beta beam detector can be extracted. It has been shown that the detector has a good muon/electron separation capability but the achievable neutrino energy resolution remains unclear. However, the experience with the Borexino detector will give an indication for the tracking potential of a liquid-scintillator detector. To evaluate LENA as a beta beam detector, a dedicated analysis of nuclear physics, neutrino-energy reconstruction and tracking features has to be performed.

---

[1]In collaboration with Joachim Kopp.

Chapter 11

Summary and Outlook

LENA [35][36] is a proposed large-volume ($\sim 50\,\text{kt}$) liquid-scintillator detector aiming to cover a rich physics program including particle, astroparticle and geophysics. In the last years, feasibility studies concerning the physics potential and measurements of liquid-scintillator optical properties have been performed. Recently, LENA has joint the LAGUNA [37] initiative which intends to design an underground observatory for proton decay and neutrino physics in Europe. Over the next three years, LAGUNA will investigate site and engineering related topics for six possible locations (Canfránc [84] (Spain), Boulby [85] (England), Fréjus [73] (France), Polkowice-Sieroszowize [37] (Poland), Slanic [37] (Romania) and Pyhäsalmi [86] (Finland)) and three different types of detectors (water-Cherenkov (MEMPHYS [33]), liquid-argon (GLACIER [34]) and LENA). Due to the laboratory depth, the locations in Pyhäsalmi and Fréjus are relevant candidates for LENA. It will be of great interest to learn about the feasibility of the detector underground construction for these two sites. In addition to this technical design study, the physics potential and the detector performance (for example concerning the liquid scintillator or the light read-out) have to be further evaluated.

In the course of this thesis, the light-emission mechanisms in organic liquid-scintillators have been investigated. To this end, two kinds of experiments have been performed: the measurement of fluorescence decay-time constants and spectroscopy of the emitted light. For the measurement of the decay-time constants, several scintillators have been tested. A suitable organic liquid scintillator is a mixture of a liquid solvent and one or more powder solutes, i.e. wavelength-shifters. Systematic studies have been carried out by varying both the solvent and the solute types and the solute concentration. Usually, there is a short decay-time constant which accounts for the main part of the emitted light (60 to 95%). For this decay constant, large differences from 2 to 8 ns have been obtained for various scintillator mixtures. In order to get complementary information on the scintillation processes, spectroscopical measurements have been performed. The medium has been excited in two different ways, namely by UV-light and by electron

radiation. The results of both methods show similar spectra, exhibiting the vibrational structure of the organic molecules. In addition, the light propagation in the medium in connection with the solute self-absorption length has been studied. Fluorescence decay-times and spectroscopical measurements have been interpreted by a microscopic scintillation model. This model includes the energy transfer between the molecules, quenching processes (loss of energy) and solute self-absorption.

The scintillator components which have been investigated are the solvents PXE, LAB and dodecan and the solutes PPO, pTP, PMP and bisMSB. Concerning the fluorescence decay-time constants and the solute self-absorption, a mixture containing PXE, about $2\,\mathrm{g}/\ell$ PPO and $\sim 20\,\mathrm{mg}/\ell$ bisMSB shows the best performance for LENA. Even without adding the secondary shifter bisMSB, the scintillator has an acceptable short decay-time constant of about $3.3\,\mathrm{ns}$ in a large detector. This allows for a good position reconstruction and permits to resolve timely close pulses. LAB is quite a new solvent candidate which shows a good transparency [133]. However, the results of this thesis demonstrate that the energy transfer between LAB molecules is slow, leading to broad pulses. If the solute concentration is increased, this effect is suppressed but the solute self-absorption increases. Further measurements are required to find a solute type and the concentration which optimizes the energy transfer and thus the signal's pulse shape in LAB-based scintillators. In general, wavelength-dependent absorption and scattering lengths are essential to properly describe the light propagation. Previous works have investigated the relative light yield emitted by different mixtures of PXE and dodecan with PPO solute [168] and PXE and LAB with PPO and PMP [51] always with a concentration of $2\,\mathrm{g}/\ell$. In addition, it would be very interesting to study the efficiency of the energy transfer between different solvent and solute molecules. For this purpose, relative light-yield measurements have to be performed where the solute concentration varies over two or more orders of magnitude. To precisely carry out these measurements, a fixed energy deposition would be desired. This can be achieved by setting up a coincidence experiment which selects the Compton edge of a gamma interaction ($180°$ scattering angle). In the end, the scintillator studies should provide all necessary parameters for a complete optical model which could then be included in the LENA detector simulation. The results presented in this thesis mark an important step towards this direction.

The performance of the liquid scintillator in LENA has direct implications on the physics potential. One major point of interest will be the search for proton decay because of its dramatic implications for particle physics. In this thesis, a Geant4-based Monte Carlo simulation has been performed for the SUSY-favored [30] decay channel $p \to K^+\overline{\nu}$ in LENA. For the detector implementation, special attention has been paid to the scintillator optical processes, the quenching effects and the properties of the photomultipliers. However, only a simplified optical model without wavelength-dependent processes has been implemented so far. From this simulation an efficiency of $\varepsilon = 65\%$ has

been obtained for the detection of the proton decay in the LENA detector. The underlying analysis is based on a pulse-shape analysis to separate proton-decay events from background due to atmospheric neutrino interactions. The mentioned proton-decay reaction has a very distinctive signature in a liquid-scintillator detector. A double-peak structure arises from the energy deposited by the kaon and its decay particles ($\tau(K^+) \simeq 12$ ns). Taking into account the current limit for the proton lifetime for this channel ($\tau > 2.3 \cdot 10^{33}$ y [29]), about 40 proton-decay events and an upper limit of 1 background event are expected to be observed in LENA after 10 years of measuring time. If no event is detected a lower limit of $\tau > 4 \cdot 10^{34}$ y could be reached. By varying the scintillation parameters in the simulation, their influence on the proton-decay sensitivity has been investigated. If the values of the attenuation and the scattering lengths are reduced from 10 m to 5 m each, a 20% decrease in the efficiency appears. Similarly, if the shortest fluorescence decay-time constant is increased from 3 to 6 ns, also the detection efficiency and therefore the sensitivity is reduced by 20%. However, the laboratory results show that the mentioned 65% efficiency in the proton-decay detection efficiency is achievable.

With the LENA detector simulation, further physics cases have briefly been studied, namely the proton-decay reaction $p \rightarrow e^+\pi^0$ and neutrino-oscillation measurements using LENA as a beta-beam [70] detector. For both cases, the obtained first results look promising. However, to be competitive to other proposed detectors, the capability of LENA to reconstruct particle tracks has to be shown. This would, on the one side, be used to discriminate atmospheric neutrino background from the proton-decay reaction $p \rightarrow e^+\pi^0$ and increase the detection efficiency. Furthermore, the reconstruction of the lepton produced by a beta-beam neutrino would help to reconstruct the incoming neutrino energy. In addition, it would be very interesting to determine the directional resolution and tracking capabilities of LENA, since this could also be used to look for low-energy atmospheric neutrino oscillations.

Appendix A

Supplement spectroscopy spectra

In this appendix, the full set of emission spectra for different PPO concentrations in PXE is presented. The data have been recorded with the UV-light excitation setup described in section 7.2 and complete the results shown there in figure 7.6. Blue circles correspond to the light guide position A (direct emission, see figure 7.4) and red circles to position B (~ 1.4 cm in-medium propagation). In the former cases, the scale of the y-axis has been changed compared to figure 7.6 (left) to include the full spectral shape. Six different mixtures are presented with PPO concentrations as indicated.
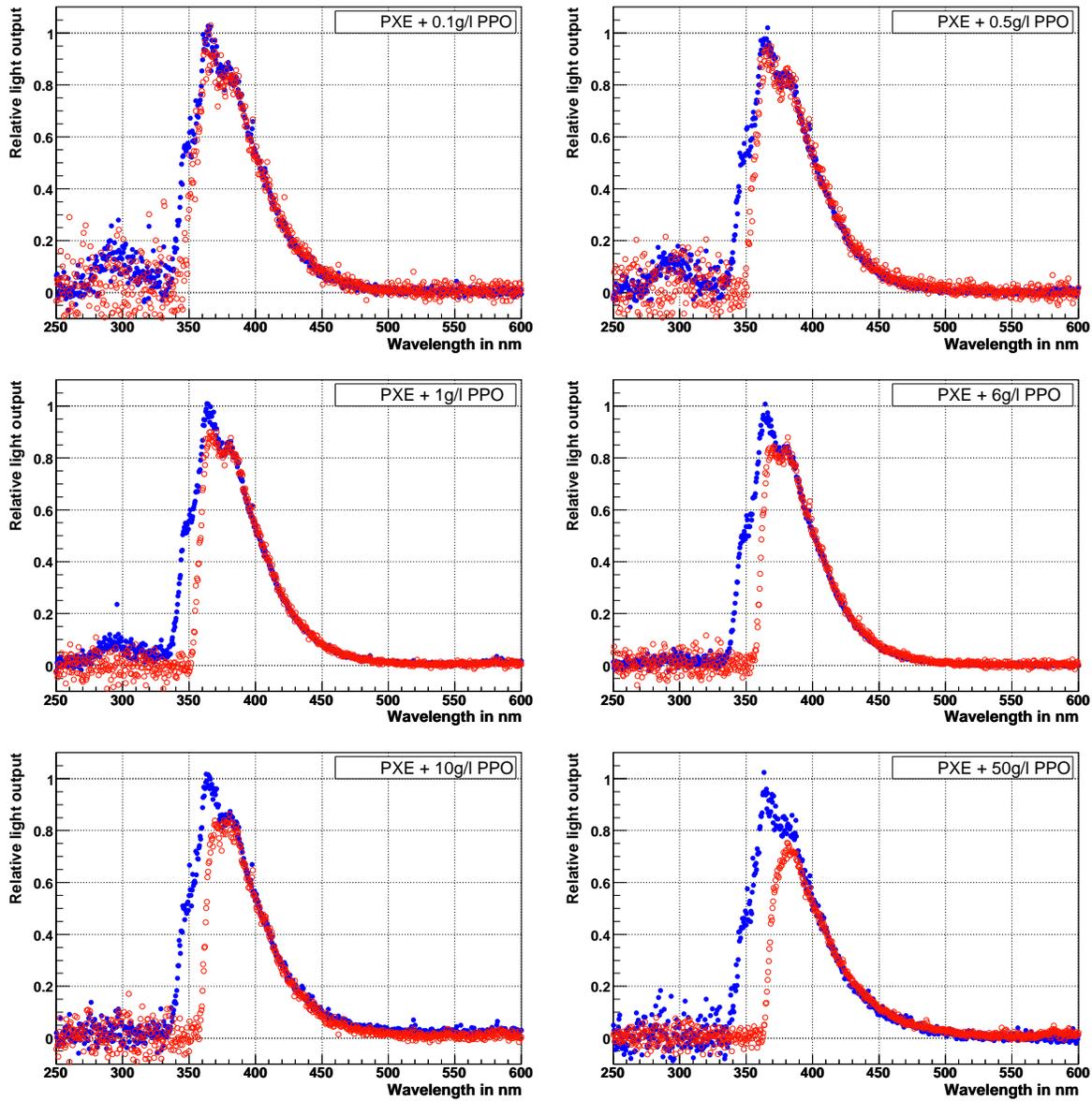
Figure A.1: Emission spectra of scintillator mixtures based on PXE (solvent) and PPO (wavelength-shifter). The PPO concentration varies from $1.0\,\mathrm{g}/\ell$ (top left) to $50\,\mathrm{g}/\ell$ (down right) as indicated in the figures.

Bibliography

[1] R. J. Davis, D. S. Harmer, and K. C. Hoffman, Phys. Rev. Lett. **20**, 1205 (1968).

[2] H. Klapdor-Kleingrothaus and K. Zuber, *Particle Astrophysics* (Institute of Physics Publishing, Bristol and Philadelphia, 1997).

[3] GALLEX, P. Anselmann *et al.*, Phys. Lett. **B357**, 237 (1995).

[4] GNO, M. Altmann *et al.*, Phys. Lett. **B616**, 174 (2005), hep-ex/0504037.

[5] SAGE, J. N. Abdurashitov *et al.*, J. Exp. Theor. Phys. **95**, 181 (2002), astro-ph/0204245.

[6] Kamiokande, M. Koshiba *et al.*, In *Minneapolis 1985, Proceedings, Grand Unification* 65-88.

[7] Kamiokande-II, Y. Totsuka, Nucl. Phys. Proc. Suppl. **19**, 69 (1991).

[8] Kamiokande-II, K. Hirata *et al.*, Phys. Rev. Lett. **58**, 1490 (1987).

[9] Super-Kamiokande, J. Hosaka *et al.*, Phys. Rev. **D73**, 112001 (2006), hep-ex/0508053.

[10] Super-Kamiokande, Y. Fukuda *et al.*, Phys. Rev. Lett. **81**, 1562 (1998), hep-ex/9807003.

[11] SNO, B. Aharmim *et al.*, Phys. Rev. **C72**, 055502 (2005), nucl-ex/0502021.

[12] Particle Data Group, S. Eidelman *et al.*, Phys. Lett. B **592**, 1 (2004).

[13] KamLAND, S. Abe *et al.*, (2008), 0801.4589.

[14] Super-Kamiokande, Y. Ashie *et al.*, Phys. Rev. Lett. **93**, 101801 (2004), hep-ex/0404034.

[15] K2K, S. Yamamoto *et al.*, Phys. Rev. Lett. **96**, 181801 (2006), hep-ex/0603004.

[16] F. Reines and C. L. Cowan, Nature **178**, 446 (1956).

[17] CHOOZ, M. Apollonio *et al.*, Phys. Lett. **B466**, 415 (1999), hep-ex/9907037.

[18] Double-CHOOZ, F. Ardellier *et al.*, (2004), hep-ex/0405032.

[19] Daya Bay, X. Guo *et al.*, (2007), hep-ex/0701029.

[20] Borexino, G. Alimonti *et al.*, Astropart. Phys. **16**, 205 (2002), hep-ex/0012030.

[21] T. Araki *et al.*, Nature **436**, 499 (2005).

[22] Borexino, C. Arpesella *et al.*, Phys. Lett. **B658**, 101 (2008), 0708.2251.

[23] Borexino, C. Arpesella *et al.*, (2008), 0805.3843.

[24] H. Georgi and S. L. Glashow, Phys. Rev. Lett **32**, 438 (1974).

[25] D.-G. Lee and R. N. Mohapatra, Phys. Rev. **D51**, 1353 (1995), hep-ph/9406328.

[26] S. Dimopoulos and H. Georgi, Nucl. Phys. **B193**, 150 (1981).

[27] F. Halzen and A. D. Martin, *Quarks and Leptons: An Introductory Course in Modern Particle Physics* (Springer-Verlag, Wiley, New York, 1984).

[28] Super-Kamiokande, M. Shiozawa *et al.*, Phys. Rev. Lett. **81**, 3319 (1998), hep-ex/9806014.

[29] Super-Kamiokande, K. Kobayashi *et al.*, Phys. Rev. D **72**, 052007 (2005), hep-ex/0502026.

[30] P. Nath and P. Fileviez Pérez, Phys. Rept. **441**, 191 (2007), hep-ph/0601023.

[31] K. Nakamura, Int. J. Mod. Phys. **A18**, 4053 (2003).

[32] C. K. Jung, AIP Conf. Proc. **533**, 29 (2000), hep-ex/0005046.

[33] A. de Bellefon *et al.*, (2006), hep-ex/0607026.

[34] A. Bueno *et al.*, JHEP **04**, 041 (2007), hep-ph/0701101.

[35] L. Oberauer, F. von Feilitzsch, and W. Potzel, Nucl. Phys. Proc. Suppl. **138**, 108 (2005).

[36] T. Marrodán Undagoitia *et al.*, Prog. Part. Nucl. Phys. **57**, 283 (2006), hep-ph/0605229.

[37] D. Autiero *et al.*, JCAP **0711**, 011 (2007), 0705.0116.

[38] J. N. Bahcall, A. M. Serenelli, and S. Basu, Astrophys. J. Suppl. **165**, 400 (2006), astro-ph/0511337.

[39] B. T. Cleveland *et al.*, Astrophys. J. **496**, 505 (1998).

[40] L. Wolfenstein, Phys. Rev. **D17**, 2369 (1978).

[41] S. P. Mikheev and A. Y. Smirnov, Sov. J. Nucl. Phys. **42**, 913 (1985).

[42] T. Enqvist *et al.*, Nucl. Instrum. Meth. **A554**, 286 (2005), hep-ex/0506032.

[43] V. A. Kudryavtsev, N. J. C. Spooner, and J. E. McMillan, Nucl. Instrum. Meth. **A505**, 688 (2003), hep-ex/0303007.

[44] T. Hagner *et al.*, Astropart. Phys. **14**, 33 (2000).

[45] H. Back *et al.*, Phys. Rev. **C74**, 045805 (2006).

[46] A. Ianni, D. Montanino, and F. L. Villante, Phys. Lett. **B627**, 38 (2005), physics/0506171.

[47] R. M. Bionta *et al.*, Phys. Rev. Lett. **58**, 1494 (1987).

[48] T. Totani, K. Sato, H. E. Dalhed, and J. R. Wilson, Astrophys. J. **496**, 216 (1998), astro-ph/9710203.

[49] M. T. Keil, G. G. Raffelt, and H.-T. Janka, Astrophys. J. **590**, 971 (2003), astro-ph/0208035.

[50] T. A. Thompson, A. Burrows, and P. A. Pinto, Astrophys. J. **592**, 434 (2003), astro-ph/0211194.

[51] J. Winter, Diploma Thesis, Technische Universität München, Garching, Germany, September 2007.

[52] L. Cadonati, F. P. Calaprice, and M. C. Chen, Astropart. Phys. **16**, 361 (2002), hep-ph/0012082.

[53] MINERvA Collaboration, 2004, hep-ex/0405002.

[54] R. Buras, M. Rampp, H. T. Janka, and K. Kifonidis, Phys. Rev. Lett. **90**, 241101 (2003), astro-ph/0303171.

[55] A. S. Dighe, M. T. Keil, and G. G. Raffelt, JCAP **0306**, 006 (2003), hep-ph/0304150.

[56] Super-Kamiokande, M. Malek *et al.*, Phys. Rev. Lett. **90**, 061101 (2003), hep-ex/0209028.

[57] S. Ando and K. Sato, New J. Phys. **6**, 170 (2004), astro-ph/0410061.

[58] M. Wurm *et al.*, Phys. Rev. **D75**, 023007 (2007), astro-ph/0701305.

[59] C. Volpe and J. Welzel, (2007), 0711.3237.

[60] K. A. Hochmuth, PhD thesis, Technische Universität München, Garching, Germany, 2008.

[61] C. Lunardini, Astropart. Phys. **26**, 190 (2006), astro-ph/0509233.

[62] S. J. Lilly, O. Le Fevre, F. Hammer, and D. Crampton, Astrophys J. **460**, L1 (1996), astro-ph/9601050.

[63] D. H. Hughes *et al.*, Nature **394**, 241 (1998).

[64] G. G. Raffelt, M. T. Keil, R. Buras, H.-T. Janka, and M. Rampp, (2003), astro-ph/0303226.

[65] K. A. Hochmuth *et al.*, Astropart. Phys. **27**, 21 (2007), hep-ph/0509136.

[66] T. Marrodán Undagoitia *et al.*, Phys. Rev. D **72**, 075014 (2005).

[67] P. Huber, M. Lindner, and W. Winter, Nucl. Phys. **B645**, 3 (2002), hep-ph/0204352.

[68] P. Huber and W. Winter, Phys. Rev. **D68**, 037301 (2003), hep-ph/0301257.

[69] J. Bouchez, M. Lindroos, and M. Mezzetto, AIP Conf. Proc. **721**, 37 (2004), hep-ex/0310059.

[70] P. Zucchelli, Phys. Lett. **B532**, 166 (2002).

[71] S. T. Petcov and T. Schwetz, Phys. Lett. **B642**, 487 (2006), hep-ph/0607155.

[72] J. Kopp, M. Lindner, A. Merle, and M. Rolinec, JHEP **01**, 053 (2007), hep-ph/0606151.

[73] G. Gerbier, Prepared for IDM 2004: 5th International Workshop on the Identification of Dark Matter, Edinburgh, Scotland, United Kingdom, 6-10 Sep 2004.

[74] C. Traunsteiner, private communication, 2008.

[75] WMAP, G. Hinshaw *et al.*, (2008), 0803.0732.

[76] D. Clowe *et al.*, Astrophys. J. **648**, L109 (2006), astro-ph/0608407.

[77] C. Boehm, P. Fayet, and J. Silk, Phys. Rev. **D69**, 101302 (2004), hep-ph/0311143.

[78] S. Palomares-Ruiz and S. Pascoli, Phys. Rev. **D77**, 025025 (2008), 0710.5420.

[79] L. Oberauer, F. von Feilitzsch, and W. Potzel, Nucl. Phys. B (Proc. Suppl.) **138**, 108 (2005).

[80] Kalliossuunnittelu Oy Rockplan LTD, www.rockplan.fi/.

[81] Borexino, C. Arpesella *et al.*, Astropart. Phys. **18**, 1 (2002), hep-ex/0109031.

[82] L. Oberauer, C. Grieb, F. von Feilitzsch, and I. Manno, Nucl. Instrum. Meth. **A530**, 453 (2004), physics/0310076.

[83] Hamamatsu Corporation, http://sales.hamamatsu.com/.

[84] J. Amare *et al.*, J. Phys. Conf. Ser. **39**, 151 (2006).

[85] E. Tziaferi *et al.*, Astropart. Phys. **27**, 326 (2007), hep-ex/0612014.

[86] J. N. Abdurashitov *et al.*, (2006), nucl-ex/0607024.

[87] NESTOR, G. Aggouras *et al.*, Nucl. Phys. Proc. Suppl. **151**, 279 (2006).

[88] J. G. Learned, S. T. Dye, and S. Pakvasa, Prepared for 12th International Workshop on Neutrinos Telescopes: Twenty Years after the Supernova 1987A Neutrino Bursts Discovery, Venice, Italy, 6-9 Mar 2007.

[89] Borexino, G. Alimonti *et al.*, Nucl. Instrum. Meth. **A440**, 360 (2000).

[90] J. B. Birks, *The Theory and Practice of Scintillation Counting* (Pergamon Press, London, 1964).

[91] A. Jabloski, Z. Phys. **94**, 38 (1935).

[92] J. Franck and E. G. Dymond, Trans. Faraday Soc. **21**, 536 (1926).

[93] E. Condon, Phys. Rev. **28**, 1182 (1926).

[94] I. B. Berlman, *Handbook of fluorescence spectra of aromatic molecules* (Academic press, New York and London, 1971).

[95] F. X. Hartmann, 2008, private communication.

[96] C. Buck, F. X. Hartmann, D. Motta, and S. Schoenert, Chem. Phys. Lett. **435**, 452 (2007).

141

[97] T. Forster, Discuss. Faraday Soc. **27**, 7 (1959).

[98] W. Leo, *Techniques for Nuclear and Particle Physics Experiments* (Springer-Verlag, Berlin, Heidelberg, 1987).

[99] I. B. Berlman, J. Chem. Phys. **33**, 1124 (1960).

[100] I. B. Berlman, J. Chem. Phys. **34**, 598 (1961).

[101] M. Born, *Optik* (Springer - Verlag, Berlin, 1965).

[102] Dixie chemical company, INC, P.O. Box 130410, Houston, TX 77219-0410.

[103] Petresa Canada Inc. (PCI), 5250 Bécancour Boulebard, Québec, G9H 3X3 Canada.

[104] Borexino, G. Ranucci *et al.*, Nucl. Phys. Proc. Suppl. **70**, 377 (1999).

[105] H. O. Back *et al.*, Nucl. Instrum. Meth. **A585**, 48 (2008).

[106] SNO+, C. Kraus, Prog. Part. Nucl. Phys. **57**, 150 (2006).

[107] Y. Ding *et al.*, Nucl. Instrum. Meth. (2007).

[108] C. Buck, private communication, 2007.

[109] Sigma Aldrich Chemie GmbH, Riedstr. 2, Steinheim, 89555 Germany.

[110] H. Guesten, P. Schuster, and W. Seitz, AIP Conf. Proc. **82**, 459 (1978).

[111] Merck, Darmstadt, Germany.

[112] H. Murayama and A. Pierce, Phys. Rev. **D65**, 013012 (2002), hep-ph/0012075.

[113] CHOOZ, M. Apollonio *et al.*, Eur. Phys. J. **C27**, 331 (2003), hep-ex/0301017.

[114] KARMEN, K. Eitel, Prog. Part. Nucl. Phys. **48**, 89 (2002).

[115] G. Ranucci *et al.*, Nucl. Instrum. Meth. **350**, 338 (1994).

[116] Electron Tubes, www.electrontubes.com/.

[117] Agilent Technologies. Acqiris, www.acqiris.com/.

[118] Labview, www.ni.com/labview/.

[119] J. Kirkbride, E. C. Yates, and D. G. Crandall, Nucl. Instrum Meth. **52**, 293 (1967).

[120] F. Rademakers and R. Brun, Linux Journal **51** (1998).

[121] W. Verkerke and D. Kirkby, The roofit toolkit for data modeling, http://roofit.sourceforge.net/.

[122] BABAR, B. Aubert *et al.*, Nucl. Instrum. Meth. **A479**, 1 (2002), hep-ex/0105044.

[123] F. James and M. Roos, Comput. Phys. Commun. **10**, 343 (1975).

[124] D. Motta, PhD thesis, Ruperto-Carola University of Heidelberg, Heidelberg, Germany, 2004.

[125] C. Kraus and M. Chen, private communication, 2007.

[126] Ocean Optics, 2007, http://www.oceanoptics.com/.

[127] A. Ulrich, 2007, private communication.

[128] LOT-Oriel, www.lot-oriel.com/.

[129] E. Hecht, *Optics* (Addison Wesley, 1987).

[130] J. Wieser *et al.*, Rev. Sci. Instr. **68**, 3 (1997).

[131] A. Morozov *et al.*, Eur. Phys. D **33**, 207 (2005).

[132] L. Niedermeier, PhD thesis, Technische Universität of München, Garching, Germany, 2004.

[133] C. Buck and M. Wurm, private communication, 2005.

[134] M. Wurm, *in preparation*, PhD thesis, Technische Universität München, Garching, Germany.

[135] P. Langacker, Phys. Rept. **72**, 185 (1981).

[136] P. Fileviez Pérez, H. Iminniyaz, and G. Rodrigo, (2008), 0803.4156.

[137] R. N. Mohapatra and G. Senjanovic, Phys. Rev. Lett. **44**, 912 (1980).

[138] N. T. Shaban and W. J. Stirling, Phys. Lett. **B291**, 281 (1992).

[139] J. Wess and B. Zumino, Phys. Lett. **B49**, 52 (1974).

[140] P. Nath, A. H. Chamseddine, and R. Arnowitt, Phys. Rev. **D32**, 2348 (1985).

[141] R. Arnowitt, A. H. Chamseddine, and P. Nath, Phys. Lett. **B156**, 215 (1985).

Bibliography

[142] I. Hinchliffe, F. E. Paige, M. D. Shapiro, J. Soderqvist, and W. Yao, Phys. Rev. **D55**, 5520 (1997), hep-ph/9610544.

[143] J. C. Pati, Int. J. Mod. Phys. **A18**, 4135 (2003), hep-ph/0305221.

[144] V. Lucas and S. Raby, Phys. Rev. **D55**, 6986 (1997), hep-ph/9610293.

[145] M. Goldhaber, P. Langacker, and R. Slansky, Science **210**, 851 (1980).

[146] O. Saavedra *et al.*, In *Nordkirchen 1984, Proceedings, Neutrino Physics and Astrophysics*, 350-361.

[147] Fréjus, C. Berger *et al.*, Nucl. Phys. **B313**, 509 (1989).

[148] Soudan-2, W. W. M. Allison *et al.*, Phys. Lett. **B427**, 217 (1998), hep-ex/9803030.

[149] G. Blewitt *et al.*, Phys. Rev. Lett. **54**, 22 (1985).

[150] Kamiokande-II, K. S. Hirata *et al.*, Phys. Lett. **B220**, 308 (1989).

[151] Particle Data Group, W. M. Yao *et al.*, J. Phys. **G33**, 1 (2006).

[152] K. Nakamura *et al.*, Nucl. Phys. A **268**, 381 (1976).

[153] Geant4, S. Agostinelli *et al.*, Nucl. Instr. Meth. A **506**, 250 (2003).

[154] Kamiokande-II, K. S. Hirata *et al.*, Phys. Lett. **B205**, 416 (1988).

[155] T. Marrodán Undagoitia *et al.*, J. Phys. Conf. Ser. **39**, 269 (2006).

[156] T. Marrodán Undagoitia *et al.*, Prog. Part. Nucl. Phys. **57**, 290 (2006).

[157] D. Rein and L. M. Sehgal, Ann.of Phys. **133**, 79 (1981).

[158] D. Rein, Z. Phys. C **35**, 43 (1987).

[159] J. Winter, private communication, 2007.

[160] Borexino, H. O. Back *et al.*, Phys. Lett. **B563**, 23 (2003), hep-ex/0302002.

[161] Double-CHOOZ, F. Ardellier *et al.*, (2006), hep-ex/0606025.

[162] MINOS, P. Adamson *et al.*, Phys. Rev. **D76**, 052003 (2007), 0705.3815.

[163] R. Adinolfi Falcone *et al.*, Nucl. Phys. Proc. Suppl. **172**, 165 (2007).

[164] P. Huber, M. Lindner, M. Rolinec, and W. Winter, Phys. Rev. **D73**, 053002 (2006), hep-ph/0506237.

[165] EURISOL DS, M. Benedikt and M. Lindroos, EURISOL-DS-TASK12-TN-06-01.

[166] D. Casper, Nucl. Phys. Proc. Suppl. **112**, 161 (2002), hep-ph/0208030.

[167] O. Buss, T. Leitner, U. Mosel, and L. Alvarez-Ruso, Phys. Rev. **C76**, 035502 (2007), 0707.0232.

[168] M. Wurm, Diploma Thesis, Technische Universität München, Garching, Germany, November 2005.

Acknowledgments

Als erstes will ich Herrn von Feilitzsch und Lothar Oberauer danken, dass ich in diese Gruppe rein kommen durfte. Mit Herrn von Feilitzsch habe ich ganz interessante Konversationen über Physik aber auch Politik in der Wisschenschaft gehabt. Lothar Oberauer hat meine Arbeit sehr nett betreut und von ihm habe ich sehr viel gelernt. Die wichtigen Aspekte meine Arbeit habe ich immer sehr gerne mit ihm diskutiert, und von seinen Erfahrungen von Borexino habe ich viel profitiert.

In Walter Potzel habe ich immer ein Ansprechpartner gehabt. Danke für die lange Physik Gespräche und insbesondere für die gründliche Korrektur dieser Doktorarbeit. Andreas Ulrich von E12 will ich auch danken für das schöne halbe Jahr wo wir zusammen experimentiert haben. Es war sehr gut für meine Arbeit die Spektroskopie Messungen die ich bei Euch machen durfte. Ohne den Herrn Hagn hätte ich es nie geschafft alle Arten von Rauschen von mein Aufbau weg zu kriegen, danke.

Von meine Arbeitskollegen will ich insbesondere Michael Wurm und Jürgen Winter für eine interessante aber auch sehr nette Zusammenarbeit sowie für die Kommentare zu meiner Arbeit danken. Wolfgang Westphal will ich bedanken für die Hilfe mit dem Computer in zahlreiche Situationen. Für interessante Diskussionen will ich auch Wolfgang Rau und Tobias Lachenmaier danken. Meine ehemaligen Werk- und Projektstudenten, Martin Hofmann, Sebastian Todor und Christoph Traunsteiner, will ich für deren Beiträge bedanken.

Alle anderen Mitglieder von E15, Cryos, Szintillators, Sekretariat, Werkstatt, will ich für die tolle Atmosphäre danken. Ich fande sehr angenehm mit Euch diese Jahren gearbeitet zu haben, auch wenn ich jede Cryomeeting über Eure Lecks hören musste. Unsere Sekretärin Beatrice van Bellen könnte ich eine lange Dankeschöns Liste schreiben.

Vielen Dank an Christian Buck und Franck Hartmann für alle die Informationen über Flüssigszintillatoren, Elisa Resconi für Ihre letzte Probe PMP, Klaus Eitel für Informationen dazu und Joachim Kopp für die Zusammenarbeit zu Beta beams.

A mi familia quiero agradecer que comprendan mi fascinación por la investigación aunque la quiera llevar a cabo en el extranjero. Ganz am Ende aber dafür das Wichtigste war der Unterstützung von Quirin Weitzel. In Tausenden von Fällen, am Computer, um über Physik zu diskutieren, um Vorträge zu üben, um mich zu motivieren, warst Du eine große Hilfe. Vielen Dank!